A Search for Double Beta Decay in ^{76}Ge

Thesis by Peter H. Fisher

In Partial Fulfillment of the Requirements

for the Degree of

Doctor of Philosophy

California Institute of Technology

Pasadena, California

1988

(submitted February 1, 1988)

Acknowledgements

I owe a great debt to my advisor, Prof. Felix Boehm, not only for guiding me through this project and my studies at Caltech, but also for giving me the opportunity to experience life in Switzerland while doing so. Invaluable guidance was also provided by Jean-Luc Vuilleumier, Kurt Gabathuler, Petr Vogel and Herb Henrikson, all of whom played irreplacable roles in completing this project. Else Garcia deserves special credit for always being there to handle the last minute difficulties and as well as the everyday ones. The other collaborators on this experiment played invaluable parts and they were Eric Bovet, Jean-Pierre Egger and Daniel Reusser. Thanks go to the institutions involved, Caltech, the Swiss Institute for Nuclear Research and the Institute of Physics at the University of Neuchatel, for providing excellent support. Special thanks to my parents for patience and understanding and to friends on both sides of the Atlantic for making both work time and free time enjoyable. Also special thanks to Howard Stone and Louis Fluri for many interesting discussions and David Mellon and Frank Booth for providing many interesting diversions.

Finally, sentiments I cannot express to Jane Ann Kincade who has been with me throughout and without whose patience and understanding I could not have completed this project. This thesis is dedicated to her.[1]

[1] Sue Ellen too.

Abstract

This thesis describes a search for the double beta ($\beta\beta$) decay of ^{76}Ge using an array of eight high purity, high resolution germanium detectors containing a total of 3.9×10^{24} ^{76}Ge nuclei. There are three modes of $\beta\beta$ decay: neutrinoless $(0\nu)\beta\beta$ decay, $\beta\beta$ decay with Majoron emission ($\chi^0\beta\beta$ decay) and two neutrino $(2\nu)\beta\beta$ decay. The first two modes violate lepton number conservation, while the third is allowed by the Standard Model. $0\nu\beta\beta$ decay may take place to the ground state of the daughter nucleus ($0^+ \rightarrow 0^+$ transition) or to an excited state of the daughter nucleus ($0^+ \rightarrow 2^+$ transition). The detector was operated for a total time of 2033 h (0.23 y) which translates to 1.30 kg-y. The background at the $\beta\beta$ decay transition energy was 0.53 counts keV^{-1} y^{-1} (10^{23} ^{76}Ge nuclei)$^{-1}$. No evidence for double beta decay of any sort was found and the half life limits are $T^{0\nu}_{1/2}(0^+ \rightarrow 0^+) > 1.2 \times 10^{23}$ y, $T^{0\nu}_{1/2}(0^+ \rightarrow 2^+) > 2 \times 10^{22}$ y, $T^{\chi^0}_{1/2} > 8 \times 10^{20}$ y, and $T^{2\nu}_{1/2} > 2 \times 10^{20}$ y, all at 90 % c.l. The limit for the neutrinoless mode translates to an upper limit of between 16 and 1.6 eV on the Majorana mass of the neutrino, depending on the nuclear matrix element used.

"This is, after all, Switzerland, where everything works; where the trains run like clocks, the clocks run like watches and the watches are synchronized with the pulse of the universe."
John McPhee,*La Concorde de Place Suisse*

"...here he found the conversation interesting and he stood waiting for a chance to air his views, as young men are fond of doing."
L. Tolstoy,*War and Peace*

Contents

Chapter 1

The Neutrino

Wolfgang Pauli first postulated the existence of the neutrino in 1930 to explain the energy distribution of electrons emitted in beta decay [1]. At the time, most physicists believed that beta decay involved the emission of an electron only. Since the nucleus is so much heavier than the electron, and energy and momentum must be conserved, the electron should be emitted with a discrete energy. This was found not to be the case; the electron was found to have energies ranging from zero to the maximum energy allowed by energy conservation. This led Pauli to his famous "desperate measure": the introduction of a chargeless lepton with very small mass.

Unlike other particles, the neutrino has "aged" rather slowly. Twenty-seven years elapsed before Reines and Cowan [2] made the first direct detection of a neutrino by absorbing an antineutrino with a proton producing a neutron and a positron ("inverse beta decay"). The fundamental interaction responsible for the production of neutrinos, the V-A (vector minus axial vector) law, had been worked out only a year earlier by Lee and Yang, [3] as a product of the surprising notion that parity was not conserved in weak interactions.

In 1963, thirty-three years after Pauli's hypothesis, the Standard Model of electroweak interactions began to emerge from the V-A law of Lee and Yang [4], Now, twenty-four years later, the Standard Model has survived a vast number of rigorous tests without showing any sign of failure and yet [5], despite numerous attempts to

measure them, the mass and charge conjugation symmetry of the neutrino remain unknown.

The mass and charge conjugation symmetry of the neutrino are not just parameters of the Standard Model, which need to be measured to complete the model; they are signposts for new physics. Charge conjugation is a crucial example since it is intimately connected to lepton number conservation, a feature of the Standard Model. The charge conjugate of a neutrino may be a distinct particle (Dirac case) or it may the neutrino itself (Majorana case). Since the neutrino carries lepton number of one, the charge conjugate of a neutrino carries lepton number of negative one. In the Majorana case, lepton number is not conserved and the Standard Model is incomplete.

Neutrino mass and charge conjugation symmetry impact fields outside fundamental particle physics. Big Bang Cosmology leaves the universe in an undetermined state: open, closed or flat. The open universe expands forever, leaving the occupants to slowly freeze to death as the energy density becomes lower and lower. The closed universe will eventually stop expanding and collapse back in itself, heating back up for another big bang. The flat universe lies just between the two cases, ever expanding, but just barely so. The energy density of the universe determines which of these destinies the universe will follow and, if neutrinos are sufficiently massive, they could account for enough density to close the universe [6]

Since neutrinos interact only weakly, they are invisible as far as astronomical observations are concerned and are classed as dark matter. Dark matter permeates current astrophysical theories on every distance scale from the mega parsecs of galactic clusters to the scant millions of kilometers of solar systems [7]. As a result, the mass and conjugation symmetry of neutrinos are needed to explain galactic clustering and rotation, stellar and solar dynamics and the composition of the interstellar medium. With so many questions depending on its properties, the neutrino must

be one of nature's truly "fundamental" particles.

Neutrinoless double beta decay depends on the charge conjugation symmetry and Majorana mass of the neutrino and the presence of right-handed coupling. For double beta decay to occur, the neutrino *must* be a massive Majorana particle; right-handed currents are not necessary for the decay to take place. One can visualize double beta decay as a sequence of processes. As a first step, a neutron in a nucleus beta decays, emitting an electron and antineutrino. If lepton number is not conserved (Majorana case) and if the neutrino is massive (so that it is not completely polarized the wrong way), it may be absorbed by another neutron in the same nucleus, turning it into a proton and another electron. A small admixture of right-handed currents will increase the decay rate by making the absorption by the second neutron more probable. By searching for the two electrons emitted in this process, the neutrinoless double beta decay rate may be determined, giving the mass of a neutrino, which remains the same under charge conjugation (called a *Majorana* neutrino.) If the process remains undetected, an upper limit is placed on the mass of a Majorana neutrino.

This thesis describes an attempt to measure the Majorana mass of the neutrino by searching for the neutrinoless double beta decay of ^{76}Ge in a low background environment. Chapter 2 contains a brief sketch of the theoretical basis for the extensions of the Standard Model that lead to massive neutrinos, with particular emphasis on double beta decay. A description of the principles and practicalities of the experimental apparatus is given in Chapter 3. Chapter 4 describes the data collected by the experiment and the extraction of the limits for the three modes of double beta decay, and Chapter 5 provides the theoretical interpretation of the half-life limits in terms of limits on neutrino masses, right-handed currents and Majoron masses. In Chapter 6, the outlook for future double beta decay experiments is given. Finally, an appendix describes the Monte Carlo program used in the background

calculations.

Chapter 2

Theoretical Background

In this chapter we explore the theoretical aspects of neutrino mass and charge conjugation symmetry leading to a relation between these properties and the neutrinoless double beta decay rate. The impact of right-handed currents and mass eigenstate mixing is also considered along with some of the nuclear physics problems associated with the calculations of the relevant nuclear matrix elements. Finally, other phenomonological results are mentioned.

Fundamental to any discussion of $\beta\beta$ decay is the distinction between Majorana and Dirac neutrinos. We will work in the Pauli-Dirac representation of the γ matrices. Since all neutrinos are emitted in weak interactions, only the $\frac{1}{2}(1-\gamma_5)$ projection of the neutrino will couple to the W boson field, and if the neutrino is massless (as it is assumed to be in the Standard Model), the solutions to the Dirac equation for a free particle will be eigenstates of the chirality operators $\frac{1}{2}(1-\gamma_5)$. For the most general spinor

$$u = \begin{pmatrix} \alpha \\ \beta \end{pmatrix}$$

where α and β are two component spinors, the eigenstates will be

$$u_R = \begin{pmatrix} \alpha+\beta \\ \alpha+\beta \end{pmatrix} \text{ for } \frac{1}{2}(1+\gamma_5)$$

and

$$u_L = \begin{pmatrix} \alpha-\beta \\ -(\alpha-\beta) \end{pmatrix} \text{ for } \frac{1}{2}(1-\gamma_5).$$

Applying the charge conjugation operator $C = i\gamma_0\gamma_2$ to any of these states has the effect of flipping the spin :

$$\psi_L = \frac{1}{2}(1-\gamma_5)u = \begin{pmatrix} \alpha^2 \\ -\alpha^2 \end{pmatrix} \qquad (\psi_L)^c = C(\overline{\psi_L})^T = \begin{pmatrix} \alpha^1 \\ \alpha^1 \end{pmatrix}$$

$$\psi_R = \frac{1}{2}(1+\gamma_5)u = \begin{pmatrix} \alpha^2 \\ \alpha^2 \end{pmatrix} \qquad (\psi_R)^c = C(\overline{\psi_R})^T = -\begin{pmatrix} \alpha^1 \\ -\alpha^1 \end{pmatrix}$$

where

$$\alpha^1 = \begin{pmatrix} 1 \\ 0 \end{pmatrix} \qquad \alpha^2 = \begin{pmatrix} 0 \\ 1 \end{pmatrix}.$$

The convention is to call the projection which has its spin oriented in the direction of the momentum the right handed projection. We now leave the realm of the Standard Model and give the neutrino a mass. The most general solution for the free particle Dirac equation is :

$$u = \begin{pmatrix} \alpha \\ -(\frac{\sigma\cdot p}{E+m})\alpha \end{pmatrix} \text{ for a particle}$$

and

$$v = \begin{pmatrix} (\frac{\sigma\cdot p}{E+m})\alpha \\ \alpha \end{pmatrix} \text{ for an antiparticle.}$$

These states are no longer eigenstates of the chirality operators, but the weak interaction still only couples to the left-handed projection of the particle state and right-handed projection of the antiparticle state. These are *Dirac neutrinos.*

Next, we form

$$\Psi_M = \frac{1}{\sqrt{2}}(\psi_L + \eta(\psi_L)^c)$$

from the massive Dirac neutrino states. The η is just a complex phase and is not of physical significance. Ψ_M has the important property that

$$C\Psi_M = \eta'\Psi_M.$$

This is a Majorana neutrino. Like a photon, the Majorana neutrino is its own antiparticle, and for this reason there are only two Majorana neutrino states as

opposed to four Dirac neutrino states. In the massless limit, the upper and lower components decouple in the Pauli-Dirac representation and Majorana and Dirac neutrinos are the same.

The distinction between Majorana and Dirac neutrinos is made clear in the following way [8]: in the lab frame, neutrinos emitted in ordinary beta decay will have polarization $\frac{-|v|}{c}$ along their direction of travel as a result of the V-A law. This neutrino is called a left-handed neutrino, ν_L. An observer moving at velocity $v_{observer} > v$ will see the same neutrino being polarized in the *positive* direction of travel and label it a right-handed neutrino, ν_R. Now, if the suspect neutrino is a Majorana neutrino and the moving observer studies the effect of a CPT transformation on the neutrino, he will find $CPT\nu_R = \overline{\nu}_L$, which is just ν_L. However, if the neutrinos are massless, they must travel at the speed of light, so there will be no frame in which a left handed neutrino will appear to be right-handed, thus a CPT transformation will not connect it with a left-handed antineutrino.

2.1 Neutrinos in the Standard Model Lagrangian

The neutrino mass may enter into the Standard model Lagrangian in two different ways [9]. The first is just the same as for the charged leptons :

$$L = \mathrm{m_{Dirac}}\overline{\psi}\psi + \mathrm{h.c.}$$

This is the Dirac case and m_{Dirac} is called the Dirac mass. It conserves lepton number. As shown above, a second way is possible because the neutrino is chargeless:

$$L = \mathrm{m_{Majorana}}(\overline{\psi^{\mathrm{c}}}\psi + \overline{\psi}\psi^{\mathrm{c}}) = \mathrm{m_{Majorana}}\overline{\psi}_{\mathrm{M}}\psi_{\mathrm{M}},$$

where

$$\psi^{\mathrm{c}} = C\psi$$

$$\psi_M = \tfrac{1}{\sqrt{2}}(\psi^{\mathrm{c}} + \psi)$$

This term does not conserve lepton number. It also has the property that

$$\psi_M = C\psi_M = \psi_M^c.$$

This is the Majorana mass term. The most general Standard Model Lagrangian will have both Majorana and Dirac terms. The Majorana term introduces processes that change lepton number by two (Figure 1).

Neutrinos interact only weakly. The interaction term in the Standard Model Lagrangian is

$$L_i^{cc} = \bar{l}\gamma^\mu \frac{1}{2}(1-\gamma^5) W_\mu^+ \nu_{weak} + \text{h.c.}$$

for the charged current interaction and

$$L_i^{nc} = \bar{\nu}_{weak}\gamma^\mu \frac{1}{2}(1-\gamma^5) Z_\mu^0 \nu_{weak} + \text{h.c.}$$

for the neutral current interaction. The subscript "weak" indicates that ν_{weak} is the weak interaction eigenstate of the neutrino field. In the most general case, these will be related to the mass eigenstates by a unitary transformation U:

$$\nu_{weak}^i = \sum_j U_{ij}\nu_{mass}^j$$

where ν_{mass} are the mass eigenstates. If at least one of the neutrinos have different non-zero masses, neutrino oscillations are possible.

Present experimental evidence from electron helicity measurements in nuclear beta decay rules out right-handed couplings down to 10^{-3} of the left-handed weak coupling strength. right-handed coupling relevant to low energy semi-leptonic processes may be introduced by the following parameterization of the Hamiltonian:

$$H_W = \frac{G}{\sqrt{2}}(J_L^\alpha(M_{L\alpha}^+ + \kappa M_{R\alpha}^+) + J_R^\alpha(\eta M_{L\alpha}^+ + \lambda M_{R\alpha}^+)),$$

where κ, η and λ (all less than one) describe the various right-handed coupling strengths and $J_L(J_R)$ and $M_L(M_R)$ are the left (right) handed lepton and quark currents.

If neutrinos are massive, several new processes will occur and other familiar processes will be altered [10], [11]. In beta decay, the energy distribution of the outgoing electron will be changed if the neutrino is massive and sharp kinks will appear if the electron neutrino mixes with other massive neutrinos. The energy distributions of the final products of other types of decay in which neutrinos are emitted will be altered in a similar way. Likewise, mixing between massive neutrinos will cause a neutrino emitted in one weak interaction eigenstate to change into another weak interaction eigenstate in flight. These are called neutrino oscillations. More massive neutrinos will be able to decay to lighter neutrinos by emitting a photon or Dalitz pair. Finally, massive Majorana neutrinos will allow certain nuclei to decay by emitting two electrons. This is double beta decay.

Each of these processes provides a way of probing the properties of the neutrino, and many experiments have been performed (and continue to be performed) searching for the effects of massive, mixed neutrinos.

2.2 Double Beta Decay

Nuclear double beta decay is the process in which two neutrons in a nucleus decay into two protons, two electrons and either zero or two antineutrinos. If two antineutrinos are emitted, the process is called *two neutrino double beta decay* ($2\nu\beta\beta$ decay). This process does not require that the neutrino be a Majorana particle or be massive and therefore is allowed by the Standard Model. The case in which no neutrinos are emitted is called *neutrinoless double beta decay* ($0\nu\beta\beta$ decay) and requires that the neutrino be a massive Majorana neutrino.

To see how the $0\nu\beta\beta$ decay rate depends on the Majorana mass of the neutrino,

consider the following decay - absorption Racah Sequence :

$$n_1 \rightarrow p_1 + e_1 + \text{“}\nu\text{”}$$

$$\text{“}\nu\text{”} + n_2 \rightarrow p_2 + e_2,$$

where the n's are neutrons, the p's are protons, the e's are electrons and “ν” is a neutrino of some sort (Figure 2). Two things are immediately apparent : the neutrino emitted by the first decay must be the antiparticle for the neutrino absorbed by the second neutron (crossing symmetry) and (assuming there are no right-handed weak currents) the particle emitted by n_1 will be right-handed while the particle absorbed by n_2 must be left handed. The Majorana neutrino fills both conditions: it is its own antiparticle (by definition) and it is not in a state of definite handedness (since it is massive).

In order for double beta decay of either kind to occur, the initial state must be more energetic than the final state. Therefore, the atomic mass of the parent nucleus (N, Z) must be greater than the atomic mass of the final nucleus $(N \mp 2, Z \pm 2)$ for double beta decay emitting two electrons (positrons). However, if the mass of the nucleus (N-1,Z+1) or (N+1,Z-1) is less than the mass of the parent nucleus (N,Z), then a cascade of two ordinary beta decays may take place, masking the much rarer double beta beta decay. Thus, the experimentally interesting case is that in which the intermediate nucleus is more massive than both the parent and the daughter nuclei, making single beta decay energetically impossible (Figure 3).

Nucleons inside the nucleus tend to bind into pairs of opposite spin, so for nuclei in which all the nucleons are paired (i.e., nuclei with even N and Z) tend to be less massive than those with unpaired nucleons, that is, those with odd Z and/or N. Double beta decay candidates then have even N and Z; hence, they typically have 0^+ ground states (zero angular momentum and even parity). If the two electrons

Figure 2.1 Majorona neutrino propagator.

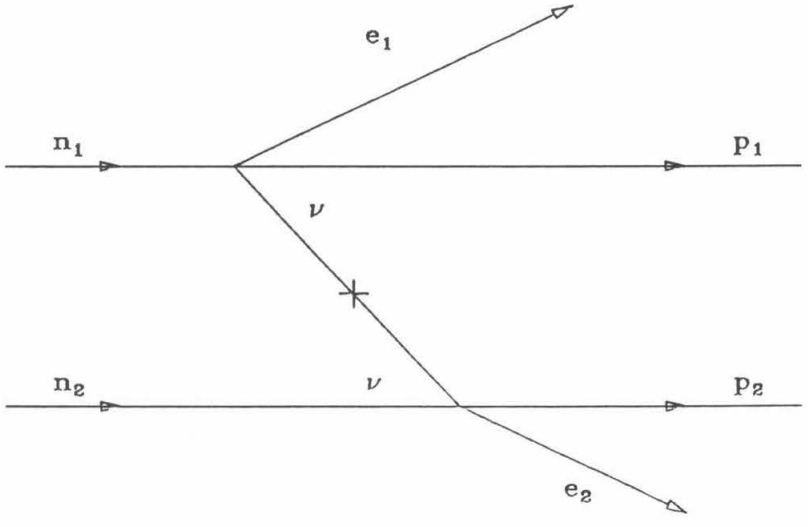

Figure 2.2 The Racah Sequence.

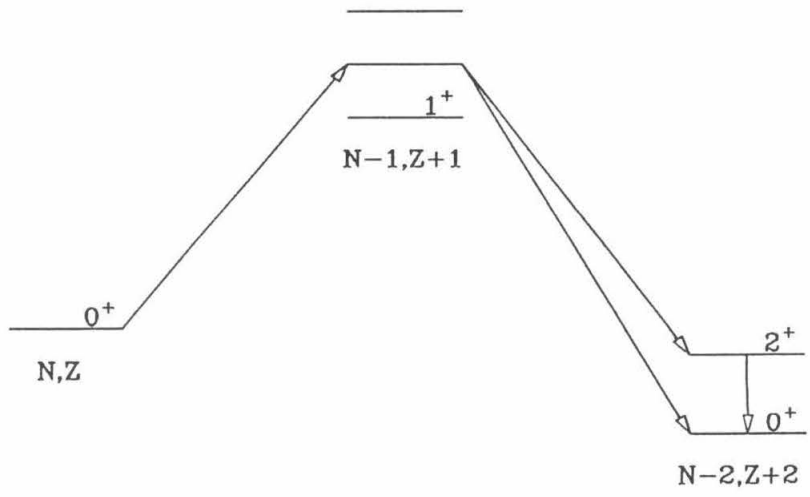

Figure 2.3 Mass schemes for double beta decay

are emitted in a zero angular momentum state, the final nucleus must be left in a 0^+ ground state or 2^+ excited state. Decay to the 2^+ state is possible if the mass of the 2^+ nucleus is less than the mass of the parent nucleus and, in the $0\nu\beta\beta$ case, if there is some form of right-handed coupling. If there is V-A coupling at both vertices, the virtual neutrino cannot carry any angular momentum from one vertex to the other, since its helicity must be the same at both vertices. If one of the vertices has some component of V+A coupling, then the neutrino may carry one unit of angular momentum, making the 2^+ final state accessable.

2.2.1 Calculation of the Double Beta Decay Rates

The details of the calculation of the decay rates for the two neutrino and zero neutrino processes are similar and will only be outlined here. Two points are essential: *first*, the matrix element for the process breaks into two parts, hadronic (or nuclear)

and leptonic. Calculation of the leptonic part is straightforward, while the calculation of the hadronic part is not. Second, since the leptonic part of the 0ν matrix element introduces a neutrino potential in between the two nucleons undergoing the decay and the 2ν process does not (since there is no virtual neutrino), the nuclear matrix elements will be different for the 2ν and 0ν processes.

Two Neutrino Double Beta Decay

We begin by calculating the rate for the 2ν process shown in Figure 4a. Since this is a low energy process, the Fermi theory is a sufficient approximation to the Electroweak model. Fermi's Golden Rule and second-order perturbation theory gives

$$d\omega = 2\pi\delta(E_i - \sum_f E_f) \mid \sum_{m,\beta} \frac{< f \mid H \mid m >< m \mid H \mid i >}{E_i - E_m - p_\nu - E_e} \mid^2$$

for the partial decay rate. Here H is the Fermi current-current interaction Hamiltonian, E_i,E_f and E_m are the energies of the initial, final and intermediate states and p_ν and E_e are the momentum and energy of the neutrino and electron emitted in the first decay. The first-order matrix elements are

$$< m \mid H \mid i >=< N_m, e, \nu \mid G_F/4\sqrt{2}(\overline{\psi}_p(g_v - g_A\gamma_5)\gamma^\alpha\overline{\psi}_n)(\overline{e}(1-\gamma_5)\gamma_\alpha\nu) \mid N_i >$$
$$= j^\alpha M_{\alpha,m,i},$$

where j and M are the hadronic and leptonic currents. The matrix element must be summed over all possible final states and a minus sign must be introduced between all amplitudes that differ by the exchange of indistinguishable leptons in the final states. This gives

$$d\omega = 8\pi G_F^4 cos^4\theta_c \delta(E_i - \sum_f E_f) \mid \sum_{m,\alpha,\beta} M^\alpha_{f,m} M^\beta_{m,i} \sum_{n_e,n_\nu} \frac{(-)^{n_e+n_\nu} J^{n'_e n'_\nu}_\alpha J_\beta}{E_i - E_m - p_{n_\nu} - E_{n_e}} \mid^2 .$$

Nucleons bound in nuclei typically have binding energies of the order of 8 MeV and may be treated nonrelativistically by neglecting the small components in the

4-component spinors. Since we are interested only in the total decay rate, all terms linear in the lepton momenta may be neglected, since they will disappear in the phase space integration. Similarly, the leptonic part of the energy denominator $E_e + p_\nu$ may be averaged to $(E_i - E_f)/2$ since, on average, each lepton pair will carry half the available energy. Contracting the leptonic currents and summing over spins gives

$$\omega_{2\nu} = \frac{G_F^4 cos^4\theta_c}{8\pi^7} \int_{m_e}^{E_0 - m_e} F(Z, E_{e1}) p_{e1} E_{e1} dE_{e1} \int_{m_e}^{E_0 - E_{e1}} F(Z, E_{e2}) p_{e2} E_{e2} dE_{e2}$$
$$\times \int_0^{E_0 - E_{e1} - E_{\nu 2}} \mid M \mid^2 p_{\nu 1}^2 (E_0 - E_{e1} - E_{e2} - p_{\nu 1})^2 dp_{\nu 1}.$$

M is the nuclear matrix element,

$$M = \sum_m \frac{< f \mid \sigma\tau^+ \mid m >< m \mid \sigma\tau^+ \mid i >}{E_m - (M_i + M_f)/2} + \frac{g_V^2}{g_A^2} \sum_m \frac{< f \mid \tau^+ \mid m >< m \mid \tau^+ \mid i >}{E_m - (M_i + M_f)/2}$$
$$= M_{GT}^{2\nu} + \frac{g_V^2}{g_A^2} M_F^{2\nu}.$$

$F(Z, E)$ is the Coulomb correction for the outgoing electrons, and is given by

$$F(Z, E) = \frac{E}{P} \frac{2\pi Z\alpha}{1 - e^{2\pi Z\alpha}}$$

in the nonrelativistic approximation. The nonrelativistic approximation is not so good for calculating the total decay rate, but is adequate for determining the shape of the total electron kinetic energy spectrum. Haxton & Stephenson [12] give a corrected value for the total decay rate based on a numerical evaluation of the Coulomb corrections. Performing the phase space integration gives

$$[T_{1/2}^{2\nu}(0^+ \rightarrow 0^+)]^{-1} = G^{2\nu}(E_0, Z) \mid M_{GT}^{2\nu} - (\frac{g_V}{g_A})^2 M_F^{2\nu} \mid^2,$$

where

$$G^{2\nu} \propto T_0^7 [1 + \frac{T_0}{2} + \frac{T_0^2}{9} + \frac{T_0^3}{90} + \frac{T_0^4}{1980}.]$$

Also of interest to experimentalists is the distribution of total kinetic energy K, which is obtained by integration over the total electron energies instead of the elec-

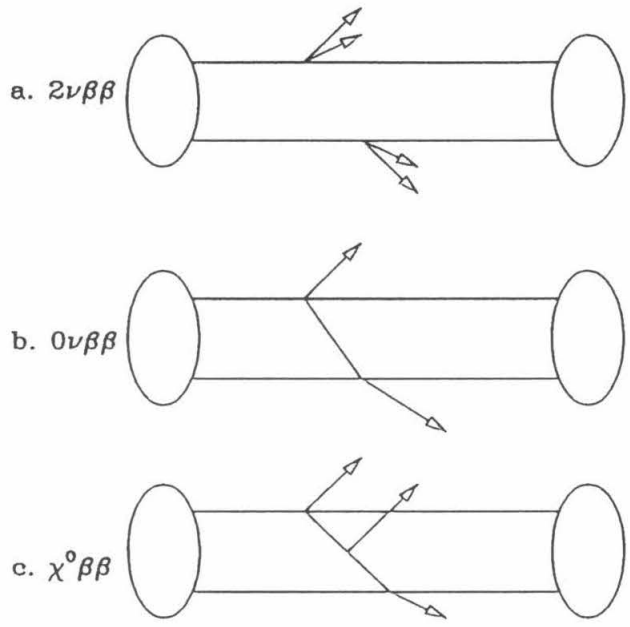

Figure 2.4 The modes of $\beta\beta$ decay: a. $2\nu\beta\beta$ decay, b. $0\nu\beta\beta$ decay and c. $\chi^0\beta\beta$ decay.

tron energies individually,

$$dN/dK \sim K(T_0 - K)^5(1 + 2K + 4\frac{K^2}{3} + \frac{K^3}{3} + \frac{K^4}{30}),$$

Figure 5.

Neutrinoless Double Beta Decay

The calculation of the 0ν decay rate proceeds similarly to the 2ν rate calculation, Figure 4b. right-handed currents can make the rate go faster but, as mentioned before, non-zero Majorana neutrino mass is the fundamental requirement for the decay to take place. right-handed currents are not considered in the following; details may be found in [10], [11] or [13]. We start by writing the partial decay rate

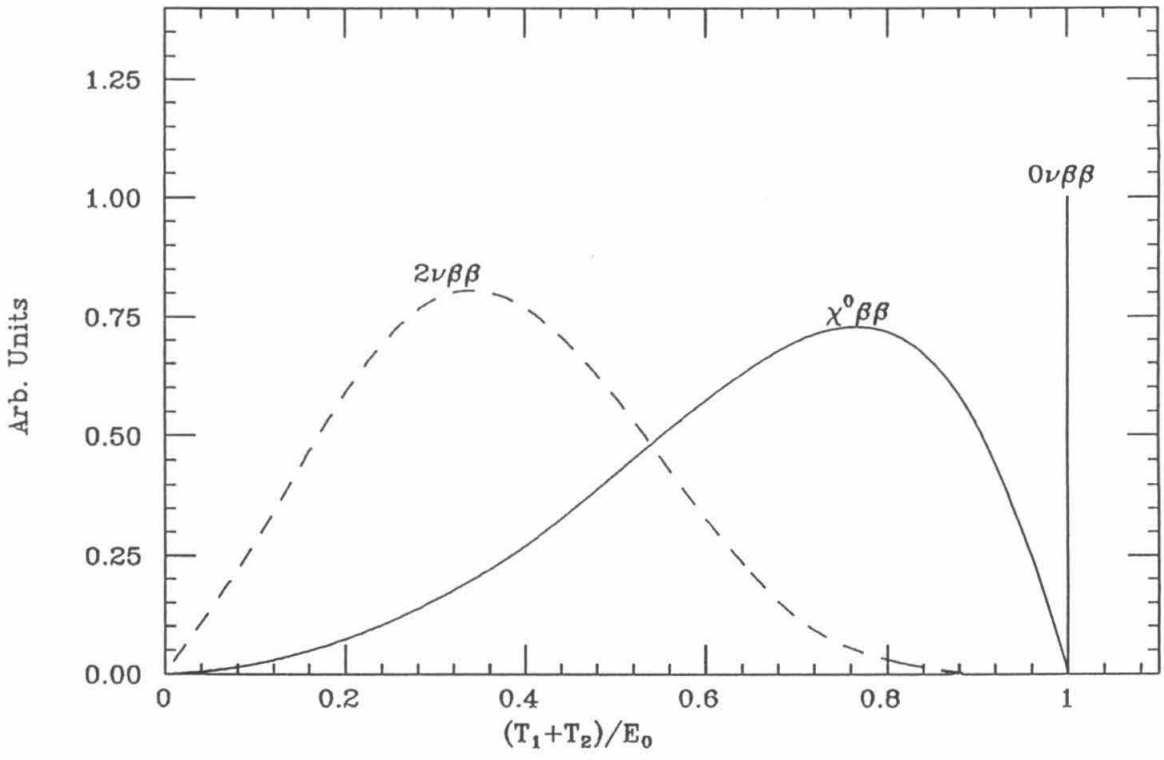

Figure 2.5 Total electron kinetic energy distributions for each mode.

as before,

$$\omega_{0\nu} = 2\pi \sum_{spins} \mid R_{0\nu} \mid^2 \delta(E_{e1} + E_{e2} + E_f - M_i) d^3p_{e1} d^3p_{e2},$$

where $R_{0\nu}$ is the transition element. Although $R_{0\nu}$ is similar to the $R_{2\nu}$ transition element, a fundamental difference arises from the neutrino propagator S_{Maj}, which appears in the leptonic part,

$$S_{Maj} = -i \int \frac{d^4q}{(2\pi)^4} \frac{e^{-iq(x-y)}}{q^2 - m^2} \overline{e}(x) \gamma_\rho \frac{1}{2}(1 - \gamma_5)(q^\mu \gamma_\mu + m_\nu) \frac{1}{2}(1 - \gamma_5) \gamma_\sigma e^C(y)$$

where q is the four momentum carried by the virtual neutrino. At low virtual energies, the neutrino propagator acts like a potential. Integrating the leptonic part, contracting the spinors and assuming that the energy difference between initial and intermediate nuclear states is much smaller than the energy carried by the virtual neutrino energy give a Yukawa potential,

$$H(r) = \frac{R}{r} e^{-r m_\nu},$$

where $R = 1.2A^{1/3}$. The total rate is then

$$[T^{0\nu}_{1/2}(0^+ \rightarrow 0^+)]^{-1} = G^{0\nu}(E_0, Z) \mid M^{0\nu}_{GT} - \frac{g_V^2}{g_A^2} M^{0\nu}_F \mid^2 < m_\nu >^2,$$

but the nuclear matrix elements are modified by the neutrino potential,

$$\begin{aligned} M^{0\nu}_{GT} &= < F \mid \sum_{lk} \sigma_l \sigma_k \tau_l^+ \tau_k^+ H(r_{lk}) \mid i > \\ &\sim < f \mid R \sum_{lk} \sigma_l \sigma_k \tau_l^+ \tau_k^+ / r_{lk} \mid i >, \end{aligned}$$

and similarly for the Fermi matrix element. The phase space coefficient is

$$\begin{aligned} G^{0\nu} \sim \int F(Z, E_{e1}) F(Z, E_{e2}) p_{e1} p_{e2} E_{e1} E_{e2} \delta(E_0 - E_{e1} - E_{e2}) dE_{e1} dEe2 \\ \sim (\frac{E_0^5}{30} - \frac{2E_0^2}{3} + E_0 - \frac{2}{5}). \end{aligned}$$

Since the nucleus is assumed to be recoilless, the total electron kinetic energy is E_0. Putting in additional terms for right-handed couplings gives

$$\begin{aligned}(T^{0\nu}_{1/2}(0^+ \rightarrow 0^+))^{-1} &= C_1 \frac{< m_\nu >^2}{m_e^2} + C_2 < \lambda > \frac{< m_\nu >}{m_e} + \\ & C_3 < \eta > \frac{< m_\nu >}{m_e} + C_4 < \lambda >^2 + \\ & C_5 < \eta >^2 + C_6 < \lambda >< \eta > .\end{aligned}$$

The C_1 coefficient is just

$$C_1 = \mid M^{0\nu}_{GT} - \frac{g_V^2}{g_A^2} M^{0\nu}_F \mid^2 G^{0\nu}(E_0, Z) m_e^2$$

and the definitions of the rest of the coefficients are given in Table 2.2.2.

The rate of the transition to the 2^+ final state does not depend explicitly on the neutrino's Majorana mass but, as mentioned before, a non-zero Majorana neutrino mass is required. The nuclear matrix elements are much more complex and there are more of them in this case; these are summarized in [13]. The total decay rate in terms of the right-handed couplings $< \lambda >$ and $< \eta >$ is

$$[T^{0\nu}_{1/2}(0^+ \rightarrow 2^+)]^{-1} = D_1 < \lambda >^2 + D_2 < \lambda >< \eta > + D_3 < \eta >^2 .$$

where

$$D_1 = 1.3 \times 10^{-17} \text{ y}^{-1}$$

$$D_2 = 2.2 \times 10^{-17} \text{ y}^{-1}$$

$$D_3 = 4.0 \times 10^{-17} \text{ y}^{-1}$$

for ^{76}Ge [13].

Double Beta Decay with Majoron Emission

A third possible mechanism for double beta decay is double beta decay with Majoron emission, $\chi^0\beta\beta$ decay [14], Figure 4c. Here, the Majoron is a massless Higgs boson

that generates the Majorana mass for the neutrino. The decay rate is given by

$$[T^{\chi^0}_{1/2}]^{-1} = R(E_0) \mid M^{0\nu} \mid^2 g^2_{ee},$$

where R is a phase space factor and g_{ee} is the coupling at the neutrino-majoron vertex. The nuclear matrix element is the same as in the $2\nu\beta\beta$ case; however, in this case, since the Majoron leaves the detector undetected, the total electron kinetic energy will be distributed over the spectrum as shown in Figure 5.

2.2.2 Nuclear Matrix Elements for Double Beta Decay

As previously mentioned, the calculation of the nuclear matrix elements for both modes of double beta decay is a difficult and, as yet unsolved problem. An adequate review of these calculations would constitute a thesis in itself; here we give a rough outline of the methods used in the context of work done in Ref. [15].

For medium to heavy nuclei, several effects must be considered : nuclear deformation, pairing and interactions between the nucleons. These calculations are carried out in several approximation schemes. The most straightforward of these schemes is the direct calculation of the matrix elements using existing shell model code [12]. Because most of the double beta decay candidates are medium or heavy nuclei, the number of states used in the shell model calculation must be truncated to make computation feasible. Also, to save computing time, a closure approximation is used in which the energy denominator is set to some average value. The shell model calculations consistently overestimate the rate for the 2ν mode, especially in the case of ^{130}Te, where geochemical experiments give a matrix element $M^{exp}_{GT} = 8.6 \times 10^{-3}$ [16] and calculation gives $M^{calc}_{GT} = 0.11$ [12]. This discrepancy has led several authors [15], [17], [18] to attempt to calculate the nuclear matrix elements using the Random Phase Approximation (RPA). Here we outline briefly the calculation of the nuclear matrix elements using RPA for the 2ν and 0ν modes. The matrix elements are separated into two parts, Fermi (τ^+) and Gamow-Teller

($\sigma\tau^+$). The Gamow-Teller transition dominates over the Fermi transition because the Fermi connects states of different isospins. For this reason, we consider only the Gamow-Teller matrix element in the following.

To begin with, we must choose some representation for the nucleon wave functions to work with. Since we wish to incorporate nuclear deformation effects, the simplest approach is to view the nucleus as an inner closed core surrounded by several partially filled outer shells and to represent the nucleons in these shells with anisotropic harmonic oscillator wave functions [19]. The advantage of this representation is that the Gamow-Teller matrix element may be calculated analytically (rather than numerically) and that the deformation enters as a single parameter, ϵ, which is just the compression or expansion of the z component of the oscillator.

Interactions between the nucleons must now be incorporated. The first step incorporates pairing between nucleons via the BCS theory and the Bogolyubov-Valatin quasi-particle transformation, [20]. The essential point is that in large nuclei, nucleons pair in states of opposite spin and momentum, similar to Cooper pairs in superconductors. The characteristic feature of this effect is a gap in the energy spectrum of states, which corresponds to the energy required to break one of the pairs in the system. As a result, the nucleon pairs with kinetic energy ϵ_k are no longer confined to the lowest energy states allowed by the Pauli Exclusion Principle, but are distributed over the states close to the Fermi surface with probability v_k^2 given by

$$v_k^2 = \frac{1}{2}[1 + \frac{\epsilon_k}{\sqrt{(\epsilon_k^2 + \Delta^2)}}],$$

where Δ is the gap energy (Figure 6).

While pairing explains the energy gap in the nuclear states, it does not explain the features of the β^- strength distribution. Calculation of the β^- strength using pairing alone gives consistently smaller ft values than are observed experimentally, indicating that a considerable portion of the β^- strength for $0^+ \rightarrow 1^+$ transitions

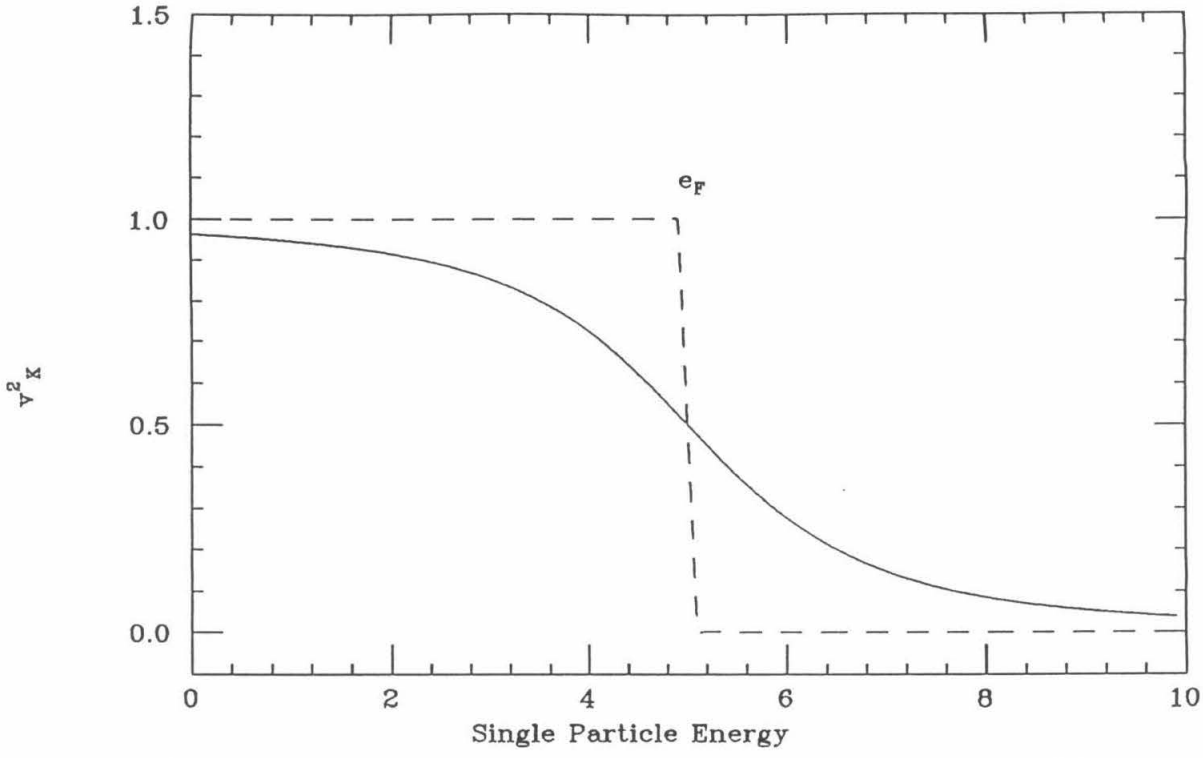

Figure 2.6 Plot of momentum vs. average occupation number. Solid line is with quasi-particle pairing; dotted is for without pairing.

lies at higher energies than those accessed in beta decay. Guidance is given by the observation of the Giant Gamow-Teller resonance [21] in (p,n) reactions on even-even nuclear targets. This implies that roughly 60 % of the β^- strength lies in states around 15 MeV above the Fermi level in the target nucleus. This effect is modelled by the "Gamow-Teller" spin-isospin polarization force, which describes the interaction between quasi-particle particle pairs and holes

$$V_{GT} = 2\chi\beta^- \cdot \beta^+,$$

where the β^- and β^+ strengths are given in terms of particle operators by

$$\beta^-_\mu = < p \mid \sigma_\mu \mid n > a^\dagger_p a_n,$$

and χ is a coupling strength given phenomenologically by

$$\chi = \frac{23}{A} MeV.$$

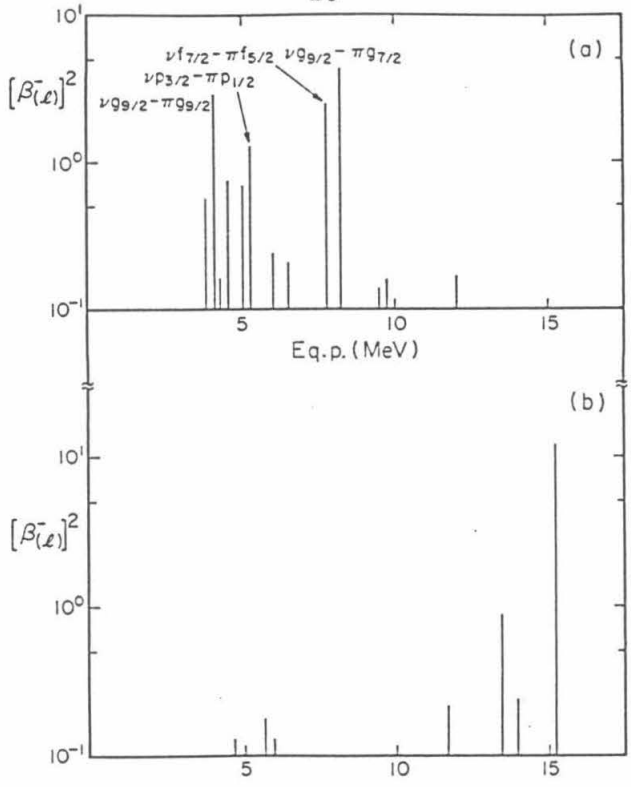

Figure 2.7 (a) β^- strength for ^{82}Se without interaction; (b) with interaction and χ =(23/A) MeV. Pairing gap Δ=1.5 MeV was used.

The inclusion of the spin-isospin polarization force has the effect of moving the β^- strength to higher lying states Figure 7.

The spin-isospin polarization force must next be written in term of the quasi-particle neutron-proton pair operators,

$$A^\dagger_{JM}(j_p, j_n) = \sum_{m_p, m_n} < j_p m_p j_n m_n \mid JM > \alpha^\dagger_{j_p m_p} \alpha^\dagger_{j_n m_n}.$$

and the Random Phase Approximation (RPA) is invoked. Essentially, the RPA requires that all interaction terms that cannot be expressed as combinations of $A^\dagger A$ are neglected. All that remains is to determine the quasi-particle energies and compute the energy weighted sum

$$M^{2\nu}_{GT} = \sum_l \frac{\beta^-_{(l)}\beta^+_{(l)}}{\omega^{(l)} + \Delta E},$$

where

$$\Delta E = M^{atomic}_{odd-odd} - M^{atomic}_{initial} + \frac{T_{max}}{2} - (E^{neut}_{qp} + E^{prot}_{qp})_{min}.$$

Author	$M^{0\nu}$	$t^{0\nu}_{1/2} \times < m_\nu >^2$	$M^{2\nu}$	$t^{2\nu}_{1/2}$
Vogel et. al. [22]	-1.97	2.7×10^{25}	0.12	1.3×10^{21}
Haxton et. al. [12]	5.51	3.4×10^{24}	0.14	1.0×10^{21}
Klapdor et. al. [23]	19.93	2.6×10^{23}	0.30	2.2×10^{20}
Faessler et. al. [24]	17.0	3.6×10^{23}	< 0.14	$> 10^{21}$

Table 2.1 Calculated matrix elements and half-lives.

The sum is carried out over the intermediate nuclear states l which, because of the $\sigma \cdot \sigma$ operator will all be 1^+. Carrying out this procedure for several nuclei, for the 2ν transition, we find the rate is suppressed when compared to the shell model calculations [12], although not enough to explain the ^{130}Te problem. To this end, Vogel et. al. [22] have incorporated the a particle-particle interaction that leads to additional suppression. The particle-particle coupling g_{pp}, which must be determined from the positron decay of neutron rich nuclei and is very uncertain, makes the degree of suppression difficult to assess. The current results of both modes is shown in Table 3.

Calculating the 0ν matrix element is considerably more difficult. Because of the neutrino propagator mentioned above, the transition operator will now be

$$M^{0\nu}_{GT} \sim < f \mid R \sum_{lk} \sigma_l \cdot \sigma_k \tau_l^+ \tau_k^+ / r_{lk} \mid i >,$$

so the sum over intermediate nuclear states will include all angular momentum-parity configurations instead of just the 1^+ as for the 2ν case. Additionally, the isospin selection rule does not apply in this case, requiring the calculation of $M^{0\nu}_F$. $M^{0\nu}$ has been calculated by several authors using both the RPA and shell model. Suppression from the particle-particle interaction is indicated, [22]; the RPA calculations are not yet complete. The calculations of Haxton & Stephenson combined with those of Doi et al. [13] gives a complete set of the ratios of coefficients C_i given in Table 8.

Physical Quantity	Coefficient	^{76}Ge
$< m_\nu >^2$	C_1	9.2×10^{-15}
$< m_\nu >< \lambda >$	C_2/C_1	-0.35
$< m_\nu >< \eta >$	C_3/C_1	-10.6
$< \lambda >^2$	C_4/C_1	1.0
$< \eta >^2$	C_5/C_1	118.
$< \eta >< \lambda >$	C_6/C_1	-0.8

Table 2.2 Coefficients for $0\nu\beta\beta$ decay in ^{76}Ge. From [10]

2.3 Other Measurements of the Neutrino Mass

As we have seen, 0ν double beta decay may be used to measure the neutrino's Majorana mass. The neutrino may, however, have a Dirac mass independently of the Majorana mass, which will not drive 0ν double beta decay and must be measured using a different technique. In this section, we provide a brief review of other processes that will be sensitive to the neutrino mass.

2.3.1 Kinematic Measurements

The mass of a neutrino may be measured kinematically in the decay of a particle. The essential problem with this method is that since the neutrino's energy cannot be measured directly, the energy of all the other particles must be measured.

For electron neutrinos, the most popular decay is

$$^3\mathrm{H} \rightarrow ^3\mathrm{He} + \mathrm{e}^- + \overline{\nu}_\mathrm{e},$$

with endpoint energy 18.6 keV. The electron energy spectrum is given by

$$d\mathrm{N} = \frac{\mathrm{G_F^2}\cos^2\theta}{2\pi^3}\xi \mathrm{F(Z,E_e)E_e p_e(\Delta - E_e)((\Delta - E_e)^2 - m_\nu^2)^{1/2}dE},$$

where

$$\xi = |\ \mathrm{C_V}\ |^2 |< 1 >|^2 + |\ \mathrm{C_A}\ |^2 |< \sigma >|^2$$

Δ = endpoint energy

$F(Z, E_e)$ = Coulomb correction factor

E_e = Energy of outgoing electron.

A Kurie plot of

$$\left(\frac{\mathrm{N(E_e)}}{\mathrm{F(Z,E_e)p_eE_e}}\right)^{\frac{1}{2}} \text{ vs. } E_e$$

will show deviation form a straight line if one or more of the neutrino flavors are massive. The most sensitive portion of the spectrum is near the endpoint where the spectrum should bend sharply away from the axis if the lightest neutrino is massive.

Although this method is appealing, it is fraught with experimental difficulties, particularly in the case of the spectrometer calibration and resolution. Currently, one group [25] reports a positive result of $14eV \leq \nu_e \leq 23$ eV, but all other groups report results consistent with zero mass, the best upper limit being 18 eV [26].

The muon neutrino mass may be measured kinematically in the decay

$$\pi^+ \rightarrow \mu^+ + \nu_\mu.$$

Here, the pions are stopped and allowed to decay. The muon's energy is then measured, giving a value for the square of the neutrino mass. The result is

$$\mathrm{m}^2_{\nu_\mu} = (-0.163 \pm 0.080)\mathrm{MeV}^2,$$

which leads to [27]

$$m_{\nu_\mu} < 0.25 MeV (90\% c.l.).$$

Another method is to measure muons from pions decaying in flight. This method gives a worse limit of $\mathrm{m}_{\nu_\mu} < 0.50$ MeV.

Since τs can be produced only at high energies, the limits on m_{ν_τ} come from accelerator experiments. The best results come from the decay

$$e^+e^- \rightarrow \tau^+\tau^- \rightarrow 3\pi\nu_\tau,$$

which gives a limit [28]

$$m_{\nu_\tau} < 50MeV(90\%c.l.).$$

2.3.2 Neutrino Oscillations

So far, only the mass of the neutrino has been considered. If for neutrino species i $(i = e, \mu, \tau)$, the mass eigenstate ν_i^m is different from the weak interaction eigenstate ν_j^w, then mixing is possible and

$$\nu_j^w = \sum_{i=1,3}^{3} U_{ij}\nu_i^m,$$

where U is the mixing matrix. Momenta for different mass eigenstates will be different if their masses are different and the neutrino will oscillate between weak interaction eigenstates. Then, for example. the probability fo a neutrino to oscillate from ν_e to ν_μ over a distance x from the source is given by

$$\mathrm{P}(\nu_e \rightarrow \nu_\mu) = |< \nu_\mu \mid \nu_e(\mathrm{t}) >|^2 = \frac{1}{2}\sin^2\theta(1 - \cos\frac{2\pi \mathrm{x}}{\mathrm{l}}),$$

where $l = \frac{4\pi \mathrm{hp}}{(\mathrm{m}_1^2 - \mathrm{m}_2^2)\mathrm{c}^2} = \frac{2.48E_\nu(MeV)}{\Delta m^2(eV)^2}$.

If the neutrino has a purely Dirac mass, neutrino oscillation conserves total lepton number L=L_e+L_μ+L_τ, but not the individual lepton number for each flavor.

A large number of oscillation experiments have been carried out at both accelerators and reactors with $\overline{\nu}_e$, ν_μ and $\overline{\nu}_\mu$ beams. So far, no confirmed evidence has been found for neutrino oscillations, and the best limit is $\Delta m^2 < 0.02\mathrm{eV}^2$ for maximum mixing, which translates into a neutrino mass limit of $m_i < 0.14\mathrm{eV}$.

2.3.3 Decay of Heavy Neutrinos

Heavier neutrinos may decay into lighter neutrinos via the two processes:

$$\nu_1 \rightarrow \nu_2 + \gamma$$

$$\nu_1 \rightarrow \nu_2 + e^+ + e^-.$$

The radiative decay rate is suppressed by the factor $(\frac{m_l}{m_W})^4$, and for $m_l = m_\tau$, the lifetime is given by

$$\Gamma_\gamma = (10^{29} years)^{-1} \frac{m_{\nu_2}{}^5}{30\text{eV}} \mid U_{\tau 1} U^*_{\tau 2} \mid^2 .$$

For the decay into the electron-positron pair, the rate is given by

$$\Gamma_{ee} = (6 \times 10^5)^{-1} (\frac{m_{\nu_2}}{1\text{MeV}})^5.$$

Neither of these decays has been observed, so only limits on masses and mixing parameters exist; see Boehm & Vogel [10] or [11] for a review of the current limits.

Chapter 3

Experimental Apparatus

3.1 Choice of Candidate Isotope

How may the double beta decay rate be measured? The best predictions indicate 0ν lifetimes will exceed 10^{21} years per eV of neutrino mass, and the best lifetime limits are even greater, $T^{0\nu}_{1/2} > 8 \times 10^{23}$ years for ^{76}Ge [29]. To be sensitive to lifetimes of such magnitude, a large number of the candidate nuclei must be assembled in an apparatus capable of measuring the kinetic energy of the two electrons emitted in double beta decay. The detection apparatus must be able to discriminate between electrons produced by double beta decay and energetic electrons produced by other means such as cosmic ray interactions, interactions between atomic electrons and gamma ray photons and electrons emitted in radioactive decays. These considerations constrain the selection of candidate nuclei and detection systems.

Most obviously, reducing the number of interactions from outside sources is the primary consideration. A candidate isotope with a high degree of purity must be chosen and the detection apparatus must be constructed out of materials containing the least possible radioactive contaminants, [1] necessitating the careful selection of all materials used in the construction of the experiment. A location low in both cosmic ray flux and terrestrial radioactivity must be chosen. Finally, the candidate

[1] This statement may sound trivial. The point is that most everyday substances contain very small amounts of radioactive substances. Paint, for example, contains ^{40}K in trace quantities.

isotope and detector must be shielded with low radioactivity material to further reduce the effect from radioactivity in nearby sources.

Obviously, the detection apparatus must be optimized to discriminate between electrons emitted from double beta decay and energetic electrons from other sources. Since the two electrons emitted in $0\nu\beta\beta$ decay will always have the same total kinetic energy (equal to the Q [2] value of the decay), a detector with very good energy resolution will help to distinguish $0\nu\beta\beta$ decay electrons. Detector systems that can distinguish between one and two (or more) primary energetic electrons have an enormous advantage in discriminating against background from beta decay or gamma ray - electron interactions. Also, a detector sensitive to the sign of the charge of energetic electrons or positrons will be able to distinguish between the two electrons from double beta decay and the electron positron pair created by pair production by a gamma ray in a nuclear Coulomb field.

Finally, choosing a candidate isotope, a balance must be struck between the cost, availability and radio-purity of the candidate and the sensitivity of the candidate, that is, the expected half-life per eV of neutrino mass. Since the latter depends on (currently) uncertain calculations of the nuclear matrix elements, the half-life per eV as a rough estimate is dominated by the phase space coefficient $G(E_0, Z)$. The phase space increase rapidly with the Q value, so candidates with higher Q values are more promising. Additionally, most of the gamma lines from the natural decay chain are below 2.0 MeV, and only the 2.614 MeV line from ^{208}Tl lies above 2.5 MeV; consequently, double beta decay candidates with Q values above 2.0 MeV will have fewer gamma lines that can cause background.

^{76}Ge was chosen as the candidate for this experiment. ^{76}Ge has a reasonably high natural abundance of 7.76 %, and its Q value of 2040.71 keV is larger than all but a

[2] The Q value is just the total energy released in the decay. For the $\beta^-\beta^-$ decay, the Q value is equal to the difference in the atomic masses of the parent and daughter nuclei.

few of the high energy gamma rays emitted by the natural decay chains. Germanium is readily available in quantities of several kilograms at very high purities and has the remarkable advantage that a high resolution detector of energetic electrons may be made out it [30]. This gives the detector almost 100 % efficiency for detecting double beta decay electrons. Such detectors can be built in fairly large sizes, about a kilogram per single crystal. An array of 8 such crystals will contain about 6 moles of ^{76}Ge nuclei. Such a system will be sensitive to 0ν half-lives of up to 10^{24} years per year of operation. Finally, such detectors are fairly compact, so they may be easily shielded from external sources.

The use of ^{76}Ge, however, has some disadvantages. First of all, germanium detectors are quite sensitive to gamma rays that penetrate the crystal and interact with an electron or nucleus in the body of the detector, resulting in energetic electrons that can mimic electrons emitted in double beta decay. Secondly, cosmic ray neutrons generate ^{68}Ga through the reaction ^{68}Ge(n,γ)^{68}Ga. ^{68}Ga then β^+ decays with a Q value of 2.92 MeV. Germanium detectors are incapable of distinguishing positrons and electrons struck by the 511 keV gamma rays (from the positron annihilation with an atomic electron) from double beta decay electrons, so ^{86}Ga decays will also mimic double beta decays. High energy cosmic ray muons may pass through the crystal , leaving an ionization trail that may be confused with $\beta\beta$ decay electrons. Finally, germanium detectors must be operated at a temperature of 100 k, necessitating the construction of a cryostat of low activity copper, a difficult engineering task.

These problems must all be faced and a thorough understanding of the physics and operation of a high purity germanium detector is a prerequisite.

3.2 Physics of a High Purity Germanium Detector

In this section, we address the basic issues of how the germanium detector detects charged particles and photons. In the following section, we consider how these processes constrain the design and construction of the detector.

3.2.1 Energy Loss of Charged Particles in Bulk Matter

High purity germanium detectors have long been used for charged particle and gamma ray spectroscopy [30]. Charged particles entering the crystal through a thin window will atoms in the crystal lattice which lie close to their trajectory , forming electron-hole pairs in the crystal. A large bias voltage applied to the opposite ends of the crystal creates an electric field that drifts the electrons to the anode and the holes to the cathode where they are collected, creating a current pulse proportional to the energy deposited by the incident particle. If the particle stops in the crystal, all the current pulse will be proportional to the total kinetic energy of the particle.

Energetic charged particles (electrons) will also be created when a gamma ray interacts inside the crystal. The energetic electron will carry some or all of the incident gamma ray energy. If, as in the case of Compton scattering, the gamma ray does not transfer all of its energy to an electron, a secondary gamma ray will emerge. When a ^{76}Ge nucleus undergoes either 2ν or 0ν $\beta\beta$ decay, two electrons will be emitted inside the germanium crystal and will lose energy as they move through the crystal. In the case of $0\nu\beta\beta$ decay, the electrons will always have a total kinetic energy of 2041 keV. In $2\nu\beta\beta$ decay, the total energy of the two electrons will be distributed over a wide range up to 2041 keV.

The electrons lose energy as they move through the germanium crystal by undergoing ionizing collisions with the atoms in the lattice. In each collision, the electron transfers some of its energy to atomic electrons, knocking them out of their atomic

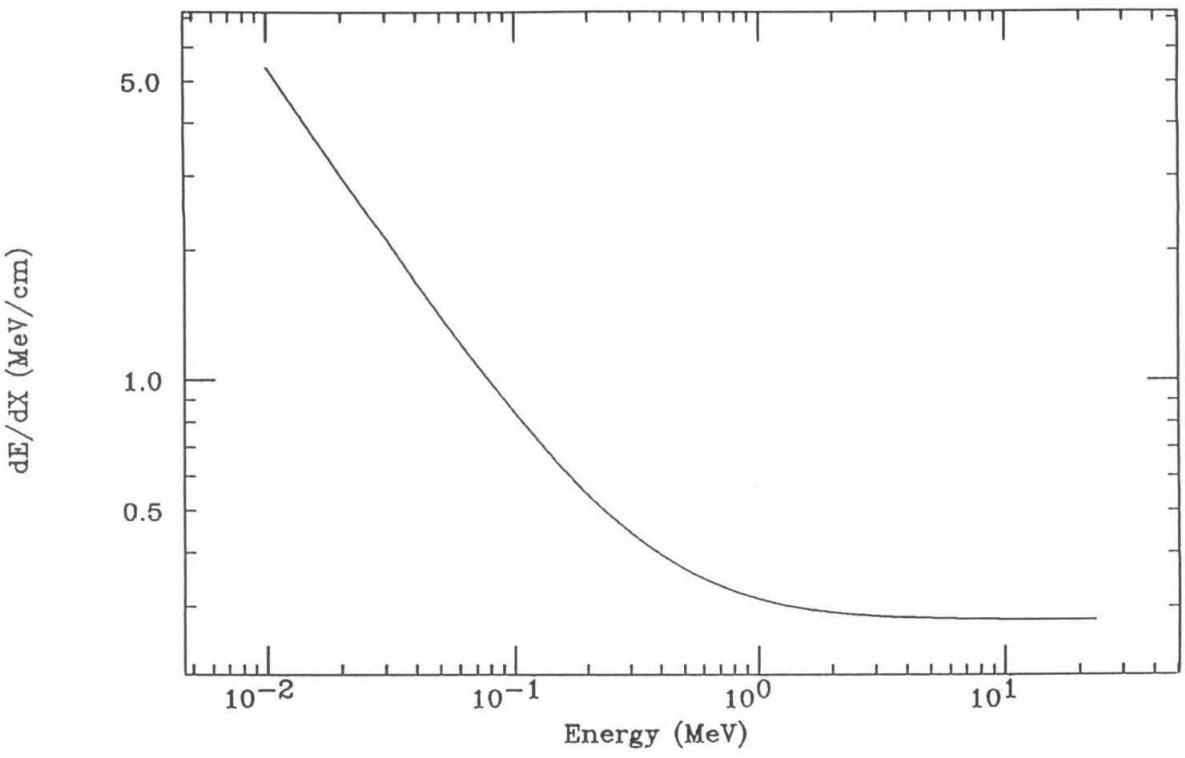

Figure 3.1 Energy loss per distance for electrons in germanium.

orbit and leaving the atom in the lattice site ionized. The crystal is kept at very low temperature, so the energy required to remove a valence electron by ionization is quite small: 2.96 keV per electron-hole pair. The expression for the energy loss of an electron moving in a medium with ionization I is

$$-\frac{dE}{dx} = \frac{4\pi e^4 N}{m_e v^2}(ln\frac{m_e v^2}{I} - \frac{1}{2}ln2 + \frac{1}{2}),$$

where N = number density of scatterers in medium

v = velocity of electron

I = ionization energy of medium.

This law goes roughly as 1/E for energies below 2 MeV (Figure 1). Primary electrons may also lose energy by bremsstrahlung. For energies below 2 MeV in germanium, this process contributes only 9 percent of the total energy loss [30]

Integrating this expression reveals that electrons with 2 MeV kinetic energy have ranges of a few millimeters. For a crystal of 150 cm^3 volume, the chance of losing an electron emitted by a $\beta\beta$ decay of a nucleus inside the crystals is less than 0.1 %.

As mentioned before, to discriminate $0\nu\beta\beta$ decay electrons from energetic electrons from other sources, the detector must have as high a resolution as possible. For a primary electron of kinetic energy 2 MeV coming to a complete stop in germanium, a total of 666,000 electron-hole pairs will be produced. Energy loss is a statistical process with constant probability per unit time, so the number of electron- hole pairs produced will be governed by Poisson statistics. For large numbers of particles, the standard deviation will be equal to the square root of the total number of particles produced. For 2 MeV, this will be 820 pairs or 5.9 keV full width half maximum. [3] Since the electron energy is related to the number of pairs collected, it appears that the ultimate resolution of the detector is given by the quoted number. However, the electrons are not free particles, as assumed in the foregoing argument. Collective effects between the pairs lead to an improvement of the resolution. The Fano factor

$$\epsilon = \frac{observed\,variance}{\frac{E_{e^-}}{E_{pair}}}$$

is a measure of this improvement. For germanium, the Fano factor is of the order of 0.1, so at 2 MeV, a germanium detector will have a resolution of 2.0 MeV FWHM [30]. Electronic noise and incomplete charge collection will increase this to about 2.5 MeV FWHM.

3.2.2 Gamma Ray Interactions in Bulk Matter

As gamma rays interacting in the crystal will be the principal source of background events, so a detailed knowledge of how gamma rays interact in the germanium detector is necessary. Gamma ray photons that enter the germanium crystal create

[3] *Full width half-maximum (FWHM)* refers to the width of a peak from the point at half-maximum below the peak to half-maximum above the peak

energetic electrons either by Compton scattering off atomic electrons, being photo-absorbed by an atom and ejecting a valence electron or by pair producing in the nuclear field, resulting in an electron-positron pair. The energetic electrons and positrons then lose energy through ionizing collisions with atomic electrons in the Ge lattice, as described in 3.1.

Photo Absorption

In the photoelectric absorption process, the incident gamma ray undergoes an interaction with the absorbing atom in which the incident photon completely disappears. An energetic photoelectron is ejected from the atom with energy

$$E_{e^-} = E_\gamma - E_{binding}.$$

For gamma rays above 20 keV, inner shell electrons are the most likely struck, leaving a vacancy. Valence electrons will decay into the inner shell, generating a 10-15 keV X-ray. This X-ray will be immediately photo-absorbed, creating a second energetic electron, which will also lose energy through the now familiar ionization process. Since all of the gamma ray's energy is converted into electron kinetic energy, the height of the current pulse generated by the ionization from the photo-ionized electron will be directly proportional to the energy of the gamma ray, E_γ (neglecting charge carrier statistics as discussed above). Typically, data from a germanium detector are plotted as number of counts versus pulse height (Figure 2). Gammas that are photo-absorbed will contribute to the full energy peak. The photo absorption cross section depends on both the Z of the absorbing nucleus and the energy of the incident gamma ray :

$$\sigma_{photo} = const. \times \frac{Z^n}{E_\gamma^3},$$

where n = 4-5.

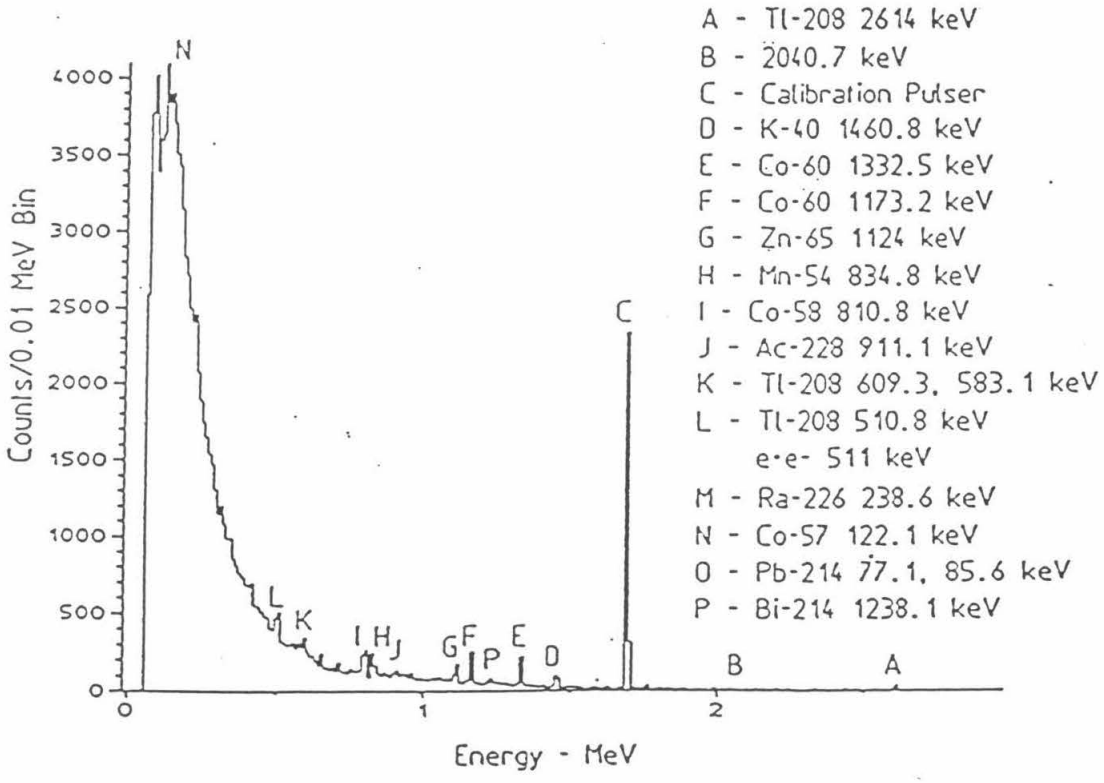

Figure 3.2 Pulseheight Spectrum from a 90 cm^3germanium detector in a low background environment. The labels refer to the photopeaks from naturally occurring gamma sources [31].

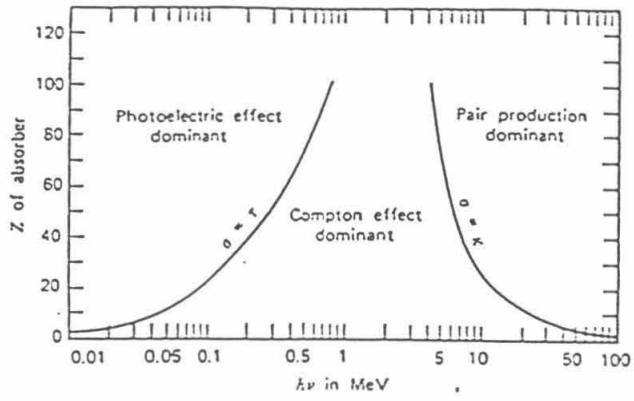

Figure 3.3 Relative cross sections of gamma ray interactions in bulk material as a function Z [30].

Because of the E_γ^3 dependence, photo absorption in Ge dominates for energies below 100 keV and is insignificant for energies above 1 MeV (Figure 3).

Compton Scattering off Atomic Electrons

Compton scattering occurs when a gamma ray scatters off a bound atomic electron, resulting in both a secondary gamma ray and an energetic Compton electron. The energy of the final products is given by

$$E_\gamma^{'} = \frac{E_\gamma}{1 + \frac{E_\gamma}{m_e}(1 - cos\theta)}$$

$$E_{e^-} = E_\gamma - E_\gamma^{'},$$

where $E_\gamma^{'}$ = energy of scattered gamma ray

E_γ = energy of incident gamma ray

E_{e^-} = energy of struck electron

θ = scattering angle.

The struck electron then loses energy via ionization, while the secondary gamma ray continues through the crystal. The maximum energy transferred to the struck

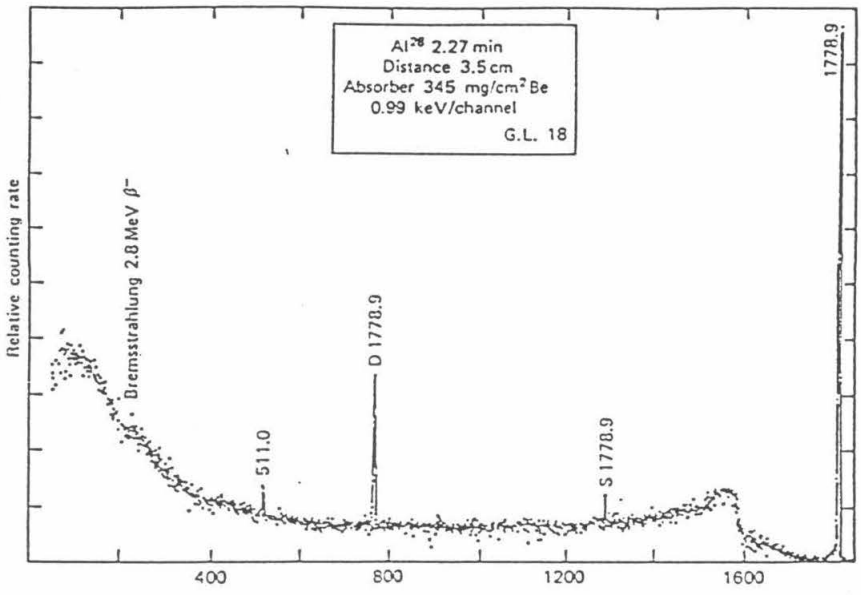

Figure 3.4 Typical pulse height spectrum from a germanium detector with a 1779 keV ^{28}Al gamma ray source. The Compton edge lies just below 1600 keV. The peaks labelled S1778.9 and D1778.9 are the single and double escape peaks from loss of 511 keV annihilation gamma rays. From [30].

electron occurs for θ=180 degrees and is given by

$$E'_{e^-,max} = E_\gamma - \frac{E_\gamma}{1+\frac{2E_\gamma}{m_e}},$$

which gives rise to the characteristic Compton edge in the pulseheight spectrum (Figure 4). The separation between the full energy peak and Compton edge is

$$E_{peak} - E_{ce} = \frac{E_\gamma}{1+\frac{2E_\gamma}{m_e}}.$$

For high energy gammas, the separation is half an electron mass (Figure 4).

The spectrum below the Compton edge is composed primarily of events in which the gamma ray Compton scatters at a smaller angle and the secondary gamma ray leaves the crystal. This is called the Compton continuum. It is possible that the secondary gamma ray will also Compton scatter or be photo-absorbed. If the latter occurs, the event will contribute to the full energy peak. If the former occurs, there

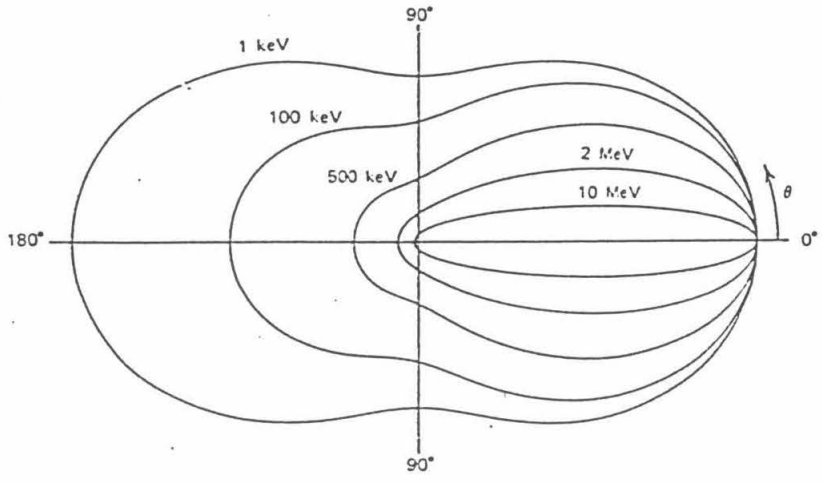

Figure 3.5 Compton scattering of gamma rays as a function of angle for energies from 1 keV to 10 MeV. From [30].

will be a third gamma ray that may interact and so on. The principal mechanism contributing to counts in the full energy peak in large (100 cm^3) germanium crystal is multiple Compton scattering followed by photoabsorption. Since the photo absorption cross section rises as E^{γ} decreases and Compton scattering always results in a lower energy gamma ray, a typical count in the full energy peak will be the result of several Compton scatterings, followed by photo absorption. Thus, the gamma ray is "cooled" by Compton scattering in the crystal.

The Compton cross section for a free electron is given by the Klein-Nishina formula

$$\frac{d\sigma}{d\Omega}_{free\ electron} = \frac{\alpha^2}{2m_e}(\frac{p^{'}}{p})^2(\frac{p^{'}}{p} + \frac{p}{p^{'}} - sin^2\theta),$$

where p = incident gamma ray momentum

$p^{'}$ = scattered gamma ray momentum,

and is sharply peaked in the backwards direction, which enhances the Compton edge (Figure 5). . For bound electrons, a correction must be applied

$$\frac{d\sigma}{d\Omega}_{atomic} = I(Z,v)\frac{d\sigma}{d\Omega}_{free}$$

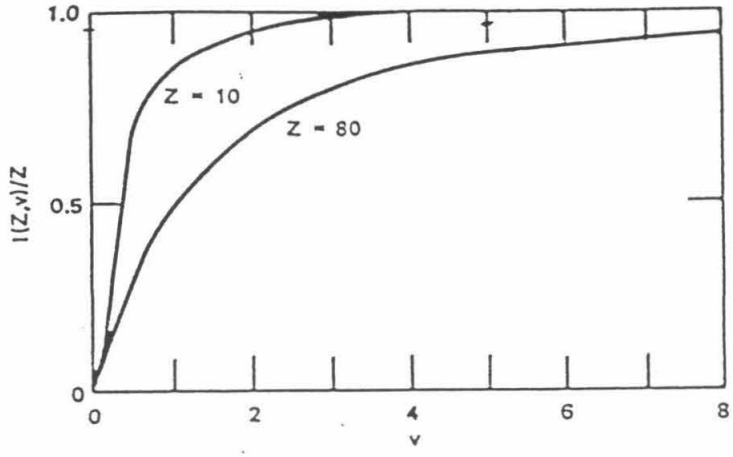

Figure 3.6 Atomic correction for Compton scattering. From [32].

where $I(Z,v)$ = correction for atomic electrons

$v = \kappa \sin\theta$

$\kappa = 29.1433\ \text{cm}^{-1}$,

which reduces the cross section for scattering in the forward direction (Figure 6). In germanium, Compton scattering is the dominant process between 100 keV and 10 MeV and is still significant above 10 MeV.

Pair Production in the Nuclear Coulomb Field

A gamma ray that has an energy above 1.04 MeV is energetically capable of interacting with the nuclear Coulomb field to produce an electron-positron pair. Both leptons lose energy through ionization and stop. The positron will then annihilate with an atomic electron into two 511 keV secondary gamma rays, which will continue through the crystal. Absorption of both 511 keV gammas will contribute to the full energy peak. Loss of one or both 511 keV gammas will contribute to the single or double escape peak, respectively, which are separated from the full energy peak by 511 and 1022 keV (Figure 4).

Pair production in the nuclear field dominates above 10 MeV, but contributes

significantly down to 2 MeV in germanium.

The pulseheight spectrum in Figure 7 is typical for a large germanium detector such as the ones used in this experiment. In general, however, the continuum part of the spectrum for a monoenergetic source will be modified depending on the geometry of the crystal and the surrounding material. The backscatter peak in Figure 4 is an example; this feature is caused by a primary gamma ray passing through the crystal without interacting, Compton scattering in some material behind the crystal to produce a backscattered secondary gamma ray travelling in the opposite direction. The secondary gamma ray is then absorbed in the crystal. For known detector and gamma ray geometries, the calculation of the expected pulseheight spectrum is a straightforward but tedious exercise in the Monte Carlo method and is described in Appendix 2.

3.3 Detector Requirements

As we have seen in Chapter 2, searches for massive neutrinos have placed upper limits on the Dirac neutrino mass of about 20 eV. To measure in double beta decay to Majorana masses of this order, a germanium experiment must be sensitive to lifetimes of more than 10^{23} years. To achieve this, the sample should be at least several moles and the background must be reduced to a minimum. Since $0\nu\beta\beta$ decay results in a peak in the pulse height spectrum at 2040.71 ± 0.39 keV, the resolution must be as high as possible. This is shown approximately for a system with resolution ΔE and N ^{76}Ge nuclei by:

$$T_{1/2}^{0\nu} > ln2 \cdot 10^{23} N \sqrt{\frac{t}{B \Delta E N}},$$

where t is the running time in years and B is the background in units of counts y^{-1} keV^{-1} $(10^{23}$ ^{76}Ge nuclei$)^{-1}$. $B\Delta E$ will be the number of background counts per 10^{23}

atoms per year. [4] The largest systems now operating [29] have $N = 4 \cdot 10^{24}$ ^{76}Ge nuclei and ΔE is fixed at 2.5 keV by the physics of the detector, so the background rate B limits the lifetime sensitivity. For such a system, Poisson statistics [33] gives

$$T_{1/2}^{0\nu}(B = 0) > 1.2 \times 10^{24} \text{years}$$

for one year of operation, assuming no background. As we shall see in Chapter 4, the background for our system is B=19 $y^{-1}keV^{-1}$, which gives

$$T_{1/2}^{0\nu}(B = 19) > 3 \times 10^{23} \text{years}$$

for one year of operation. Clearly, the sensitivity of the detector depends strongly on the level of background, and every effort was made to reduce this level as much as possible, as described below.

3.3.1 The 90 cm^3 Germanium Crystal Detector

The construction of a large germanium detector system of sufficient size to probe the the neutrino mass in the region of a few eV presses the limits of both detector technology as well as background suppression. As an intermediate step, a 90 cm^3 detector was built by a commercial firm (Princeton Gamma Tech) and installed in a low background cryostat. The setup is shown in Figure 8. The detector system was surrounded by 11 cm of oxygen-free high conductivity copper, followed by 15 cm of lead. The cooper-lead shielding was enclosed in an aluminum enclosure, which was continuously purged with nitrogen to expel any ^{226}Ra gas produced in the decay of ^{238}U. As an initial test, the 90 cm^3 detector was set up in the subbasement at Caltech with a veto to reduce the background from cosmic muons [34]. The detector was operated for over 2000 hours in early 1983, and it became apparent that the cosmic muon background made further operation pointless. The decision

[4] The above relation is reasonable when $B\Delta E > 20$, that is, when the fluctuation of the number of counts in the window where the signal is expected is Gaussian. When $B\Delta E < 20$, Poisson statistics must be used and the above relation must be modified accordingly.

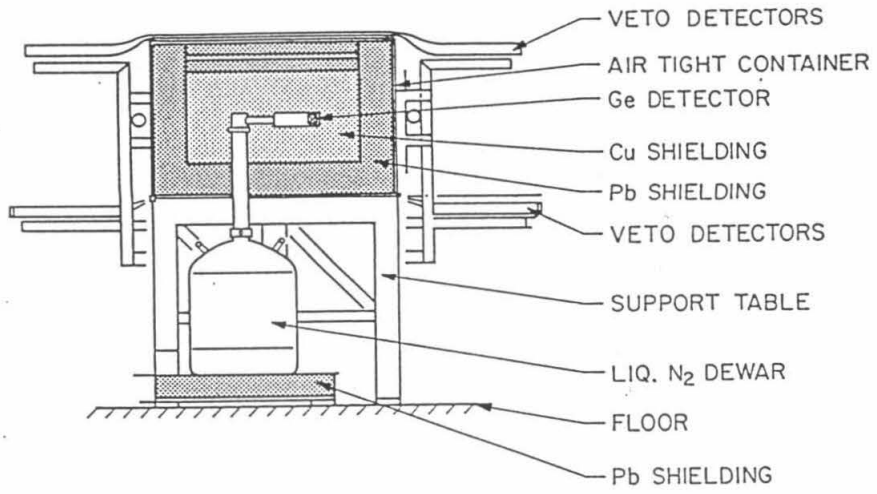

Figure 3.7 The 90 cm^3 detector setup. The muon vetos were not used in the St. Gotthard Tunnel.

was made to install the detector in an underground site, the St. Gotthard tunnel in Switzerland. Negotiations in collaboration with the Swiss Institute for Nuclear Research and the University of Neuchatel in fall 1984 led to a long term agreement completed in January 1984 to set up the detector in an emergency cross tunnel. The detector was shipped to Switzerland in spring 1985 and was setup and operating by summer of that year. After installation in the tunnel, 20 cm of borated polyethylene were added to reduce possible background from thermal neutrons. The pulse height spectrum was recorded using an 8192 channel analyzer covering the range from 10 keV to 2.8 MeV.

This small detector served three purposes. First, it served as a double beta decay experiment itself ([34] [35] [31].) Second, it allowed testing of materials used in the construction of the large 8-crystal system described below. Finally, it allowed the identification of gamma rays from background sources in the underground laboratory

and the measurement of their intensities.

Various components used in the construction of the large detector system were tested for radioactive contaminants by placing them inside the shielding next to the 90 cm^3crystal. The substances being tested were left in the shielding for one or two weeks. From the data it was determined which materials were acceptable for use in the eight-crystal system. There were two primary critia: the background rate around 2 MeV (the double beta decay energy of ^{76}Ge) and the rate of the 2614 keV gamma ray from the decay of ^{208}Tl (^{232}Th decay series). The rate of the 2614 keV gamma lines is important because it is the only known strong gamma line above the double beta decay transition energy. Only materials used in the actual construction were tested. The results of the materials tests are shown in Table 1.

3.3.2 The Eight Germanium Crystal System

After operating the 90 cm^3detector in the tunnel for one year, the detector was dismounted in Spring 1986 and a prototype 8 crystal cryostat containing one 140 cm^3crystal was installed. This detector was manufactured by Detector System GmbH, Mainz to our specifications. At this time, the local shielding was increased from 11 cm to 25 cm of copper and 15 cm to 25 cm of lead. The prototype was found to have excellent resolution and stability, but contained an unacceptably high level of ^{232}Th and was taken apart after two months of operation. The 90 cm^3detector was then remounted in the thicker shielding and each component of the 8 crystal cryostat, including the germanium crystals, was tested in the remounted 90 cm^3detector. A substantial amount of ^{232}Th contamination was found inside the "shoe box" cryostat cover. All the copper parts were washed in Radiac wash and then ultrasonically cleaned. After cleaning, the cryostat cover was retested and the ^{208}Tl contamination was not detectable. Finally, in April 1987, the 8 crystal cryostat was reassembled with its eight 140 cm^3crystals and was remounted in the tunnel.

Material	Test Time (days)	^{208}Tl 2614 keV (counts)	Counts above 1500 keV
Background	7	2	25
Lead	7	0	34
Gold, Cap.	14	100+	100+
Siemans Mkt Cap. (6.3 kV, 2.5 μF)	13	15	144
Capacitor	14	3	44
Copper Foil, Epoxy	12	1	39
Silver Solder	7	0	28
HV Capacitor	10	0	39
Green HV Wire, Indium	14	3	43
Red Signal Wire	24	6	77
Black Epoxy	7	207	200+
Delrin FET Mount (White teflon)	7	4	36
Gallium-Indium Wire	14	2	58
Black Delrin, Colorless Wire	7	4	31
Black Delrin	10	2	35
Resistors	8	0	33
FET (16) SS-PN-4393-011	14	3	27

Table 3.1 Results of Materials tests. The substances tested were placed next to the 90 cm^3 germanium detector inside the local shielding. The efficiency for 2.5 MeV gamma rays was about 5%.

A plan of the detector is shown in Figures 9 and 10. Eight-high purity germanium crystals, each with an active volume of 140 to 145 cm^3, form the detector array. The minimum total fiducial volume is 1100 cm^3, giving a total of 3.9×10^{24} ^{76}Ge nuclei. Each crystal is mounted in its own copper box, which is bolted to the base plate with copper screws and bolts. The copper base plate is connected to the cold finger, which maintains the 100 K operating temperature of the crystals. The entire assembly is surrounded by copper heat shields followed by a thick copper cover. The long cold finger allows the "shoe box" containing the crystals to be completely surrounded by passive shielding.

The electrical connections made inside the crystal are shown in Figure 11. The resistor, FET and capacitor C1 are mounted on a teflon holder mounted on the end of the copper cup. To reduce activity from tin and lead, no solder connections were made; copper crimps were used to make all electrical connections inside the shoe box. The high voltage filter capacitor C2 was homemade from epoxy, copper and gold and mounted behind the large copper block as shown in Figure 11. The preamp and high voltage wires were run down the cold finger to the preamps, which were mounted on the caroussel just above the dewar. The signals were read out by computer through an 8192 channel ADC and stored on a disk along with the time and a pattern showing which crystals fired. Only the total energy from all crystals was stored; the pulses from all the crystals were summed in the router (Figure 12). Once a week, the disk was read off onto tape.

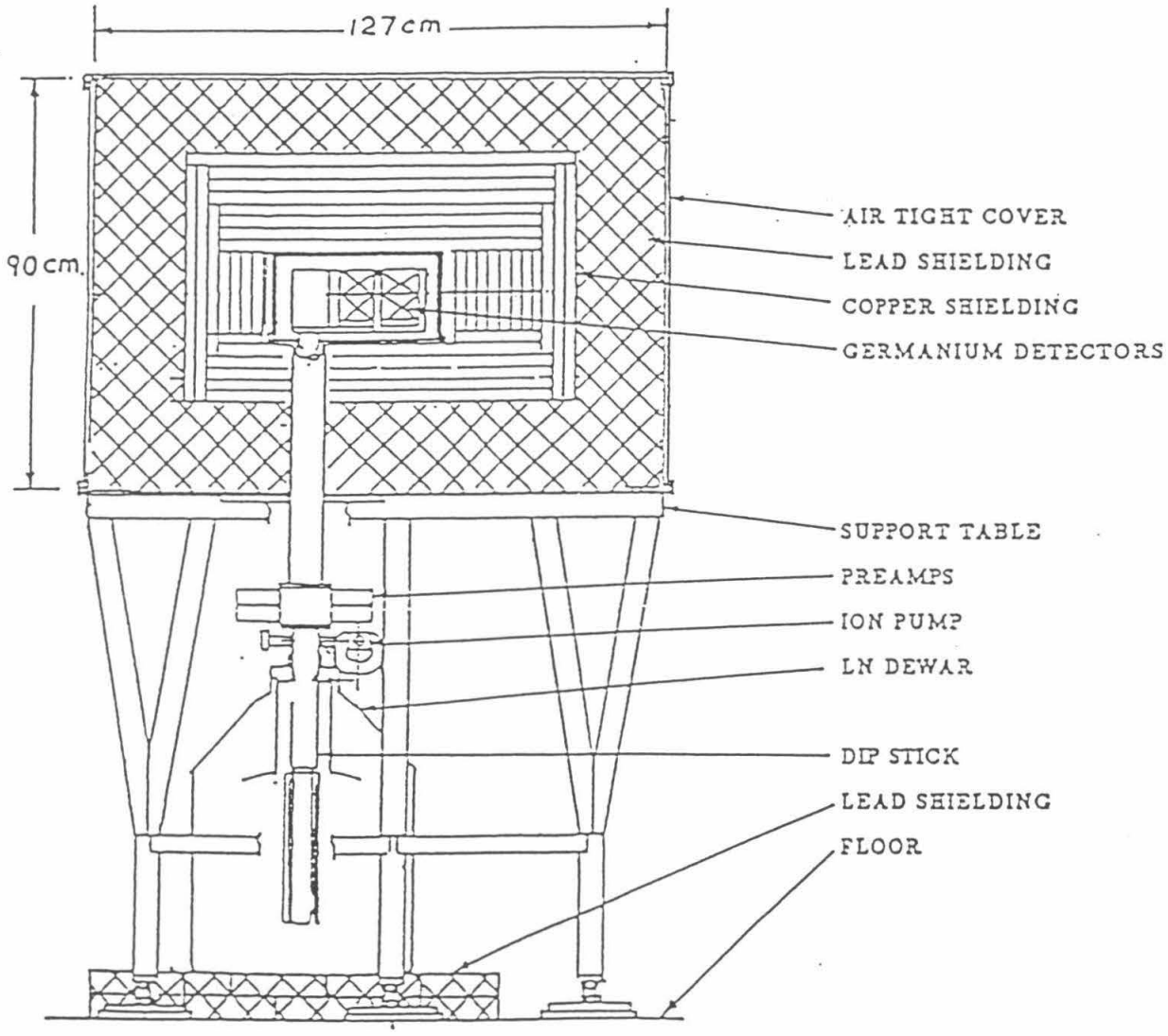

Figure 3.8 Eight crystal germanium system.

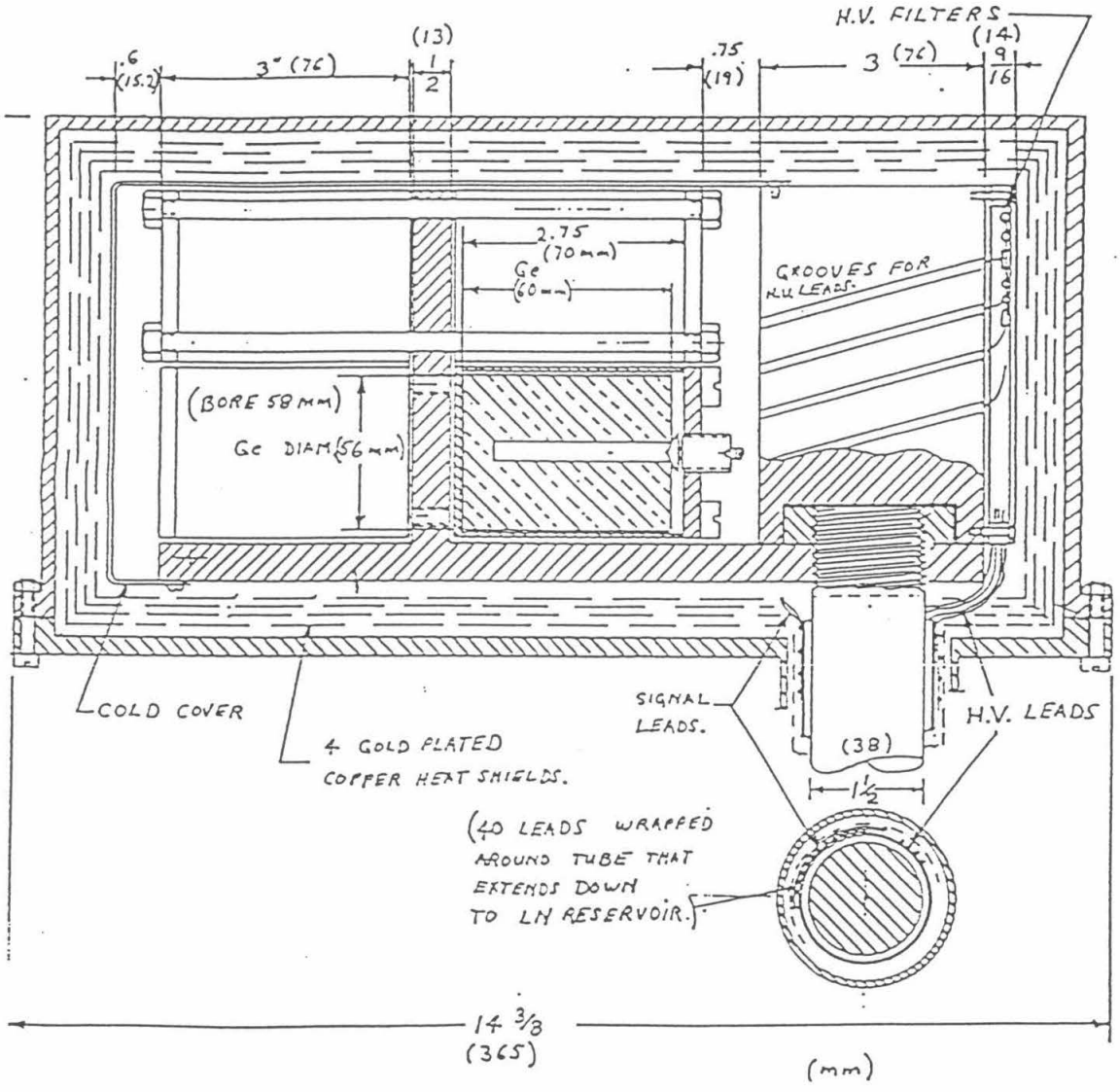

Figure 3.9 Cryostat containing eight 140 cm^3 germanium crystals

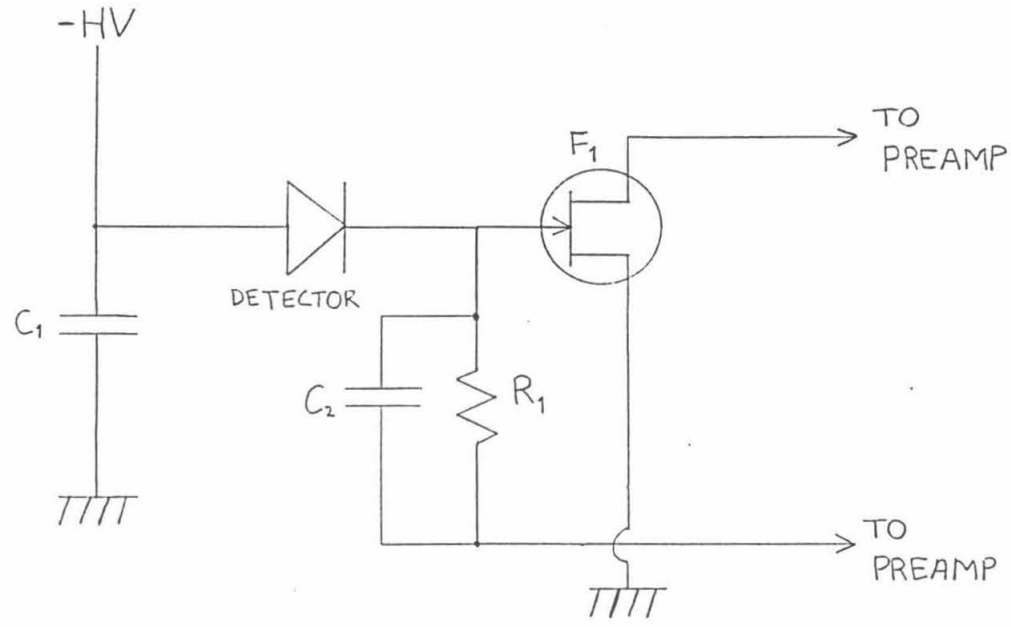

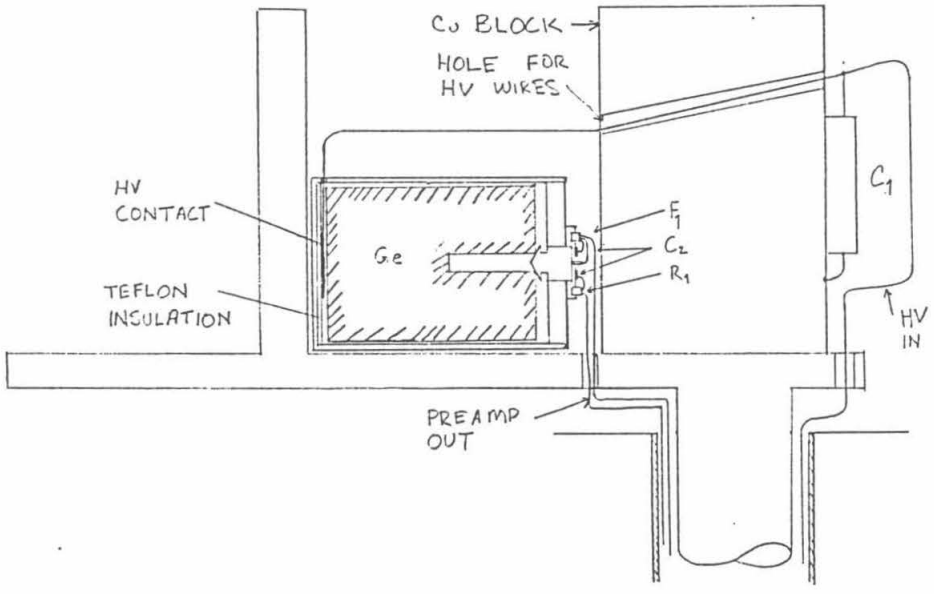

Figure 3.10 Electrical connections made inside cryostat.

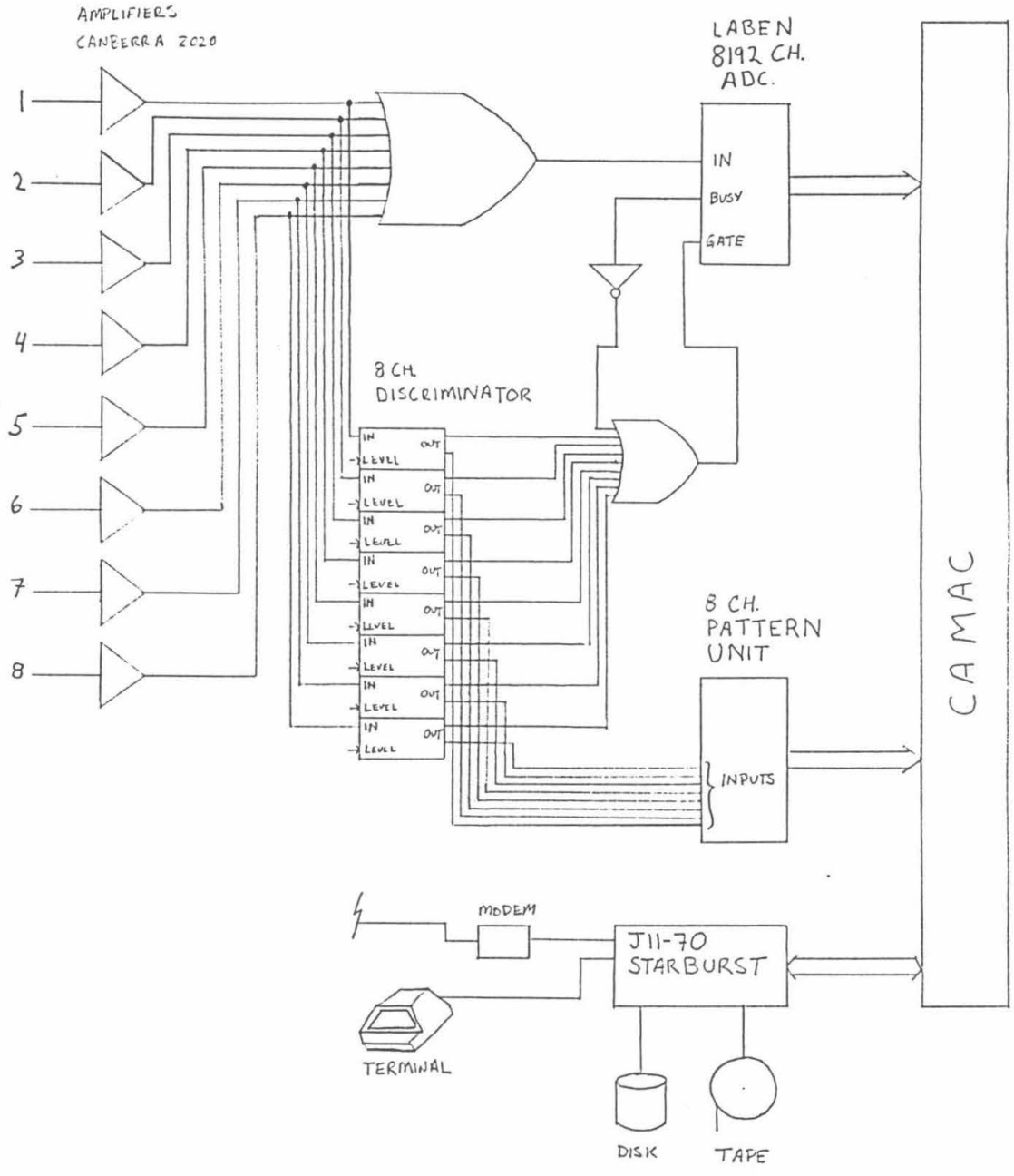

Figure 3.11 Data acquisition system.

Chapter 4

Measurement and Determination of $\beta\beta$ Decay Rates

4.1 Background Measurements

Aside from testing all materials used in the construction of the eight-crystal detector, several other measures were taken to reduce background. These were: placing the entire system deep underground to eliminate cosmic ray muons, surrounding the crystals with copper and lead shielding to absorb gamma rays and placing borated polyethylene shielding around the copper lead shielding to absorb thermal neutrons. This section describes the measurements and resulting backgrounds.

4.1.1 Measurements with the 90 cm^3 Detector

Cosmic ray muons passing through a germanium crystal will ionize atomic electrons close to its path, giving rise to a current pulse. There are two methods of reducing the cosmic ray muon background: an active veto or passive shielding. Passive shielding was chosen for this experiment as it is much more effective than an active veto. The passive shielding was Monte Prosa, a mountain near the St. Gotthard pass. The entire system was set up in bay B59 of the St. Gotthard road tunnel, 4 km. from the town of Airolo (Figure 1). Approximately 1000 meters of rock (equivalent to 3000 m of water) constitute the overburden. It serves to attenuate

the muon flux (Figure 2) by a factor of 2×10^5 to 4.4 h^{-1} striking the 1 square meter of the local shielding. Of these, 0.011 h $^{-1}$ or about 2 week $^{-1}$ strike the 25 square centimeter surface of the germanium crystal. The muons may also interact inside the shielding to produce photons, which may then interact inside the crystal. Assuming each muon generates one 3 MeV gamma ray and considering solid angle detector efficiency and attenuation through the local shielding, this flux of gamma rays from muonic interactions is less than 10^{-4} h $^{-1}$ or one per year.

Another important source of background is gamma rays from radioactive decays. The rock surrounding the tunnel is primarily red granite, which contains on the order of 10 ppm by weight [36] of ^{232}Th and ^{238}U, which are the precursors of the two principal natural decay chains (Figures 3 and 4.) Both emit gamma rays up to 2.6 MeV. The most direct way of reducing the background from these decay chains is to surround the crystal with high Z material in the form of local shielding. For the 90 cm^3 detector, an average of 11 cm of copper was placed around the crystal followed by 15 cm of lead. This has the effect of reducing the flux from the ^{208}Tl 2614 keV line by a factor of 3×10^4. The background with this shielding configuration (Shield I) was measured for 6728 h and is shown in Figure 1. The rate of the ^{208}Tl 2614 keV gamma ray photopeak was consistent with direct attenuation through the lead-copper shielding. To further reduce the gamma ray background, the local shielding was increased to 25 cm of copper and 25 cm of lead. The background spectrum from this second shielding configuration was measured in a second run of 2645 h (Shield II) and is shown in Figure 2. The photopeak rates from both runs are summarized in Tables 3 and 4.

The photopeak rates require some explanation. As described in Chapter 3, extensive materials tests were carried out during the Shield I and II runs. The criteria of these tests were that the material had no counts above background in the region above 1700 keV and in the photopeak for the 2614 keV line; the latter was usually

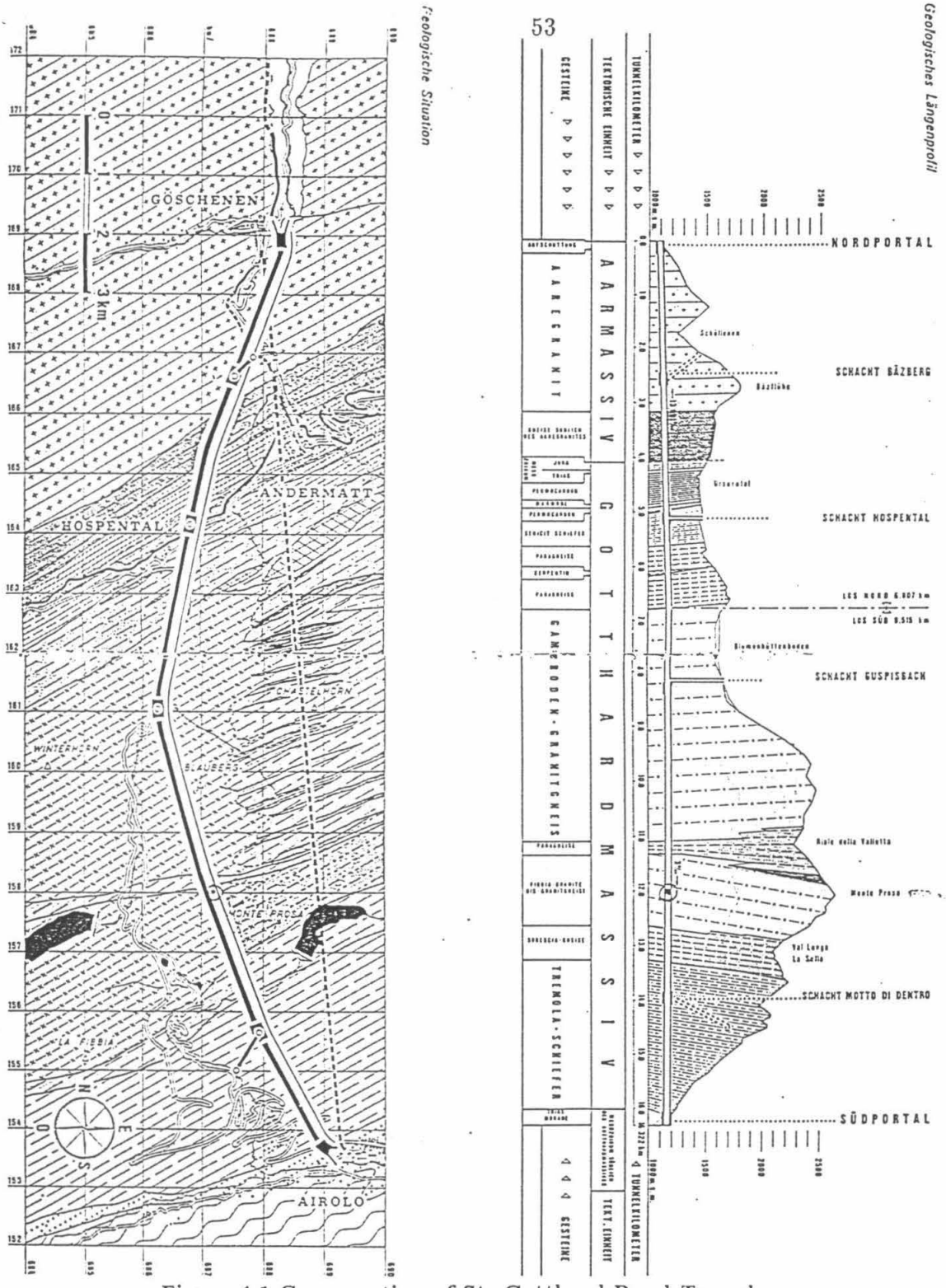

Figure 4.1 Cross section of St. Gotthard Road Tunnel.

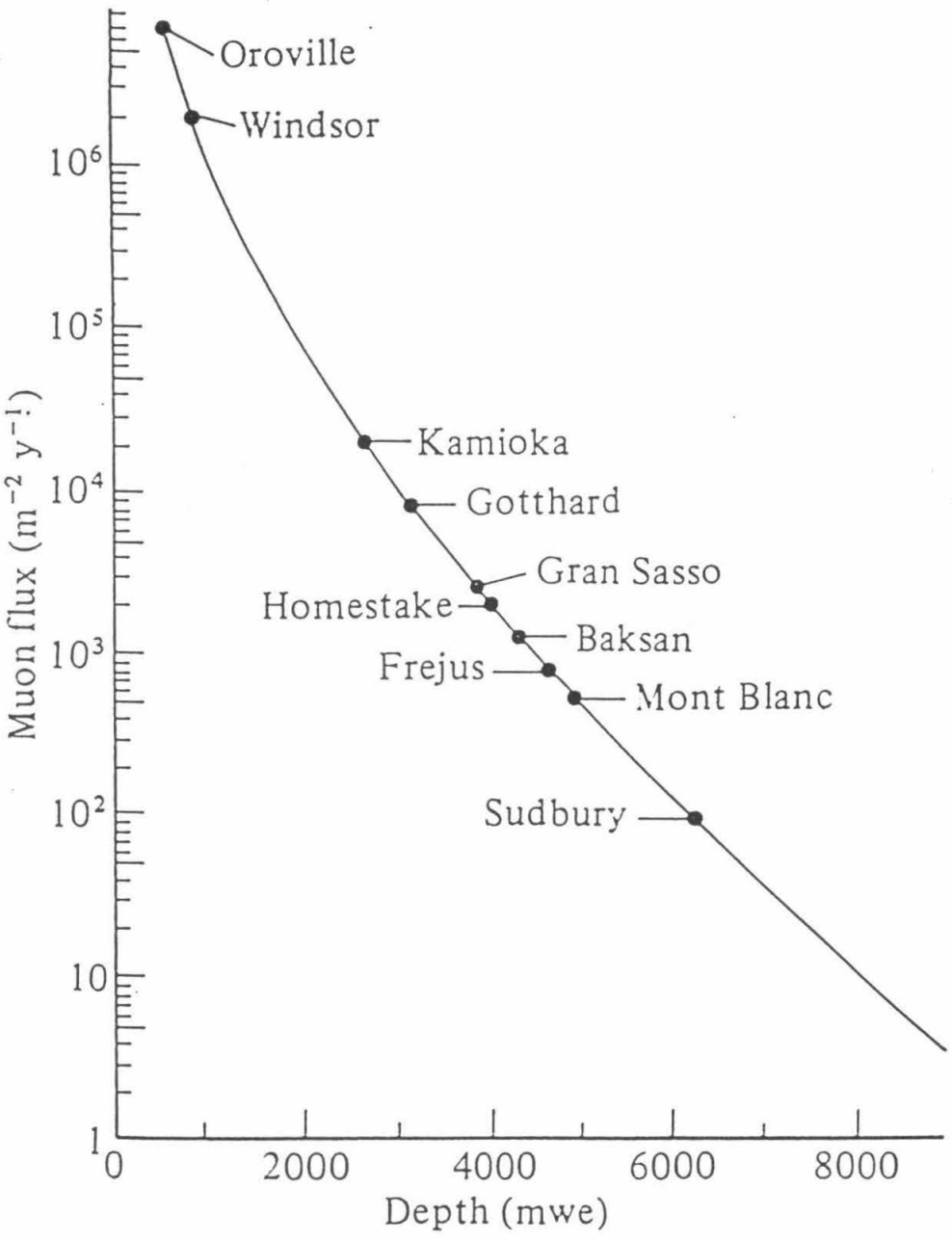

Figure 4.2 Muon flux in the St. Gotthard Road Tunnel. From [12].

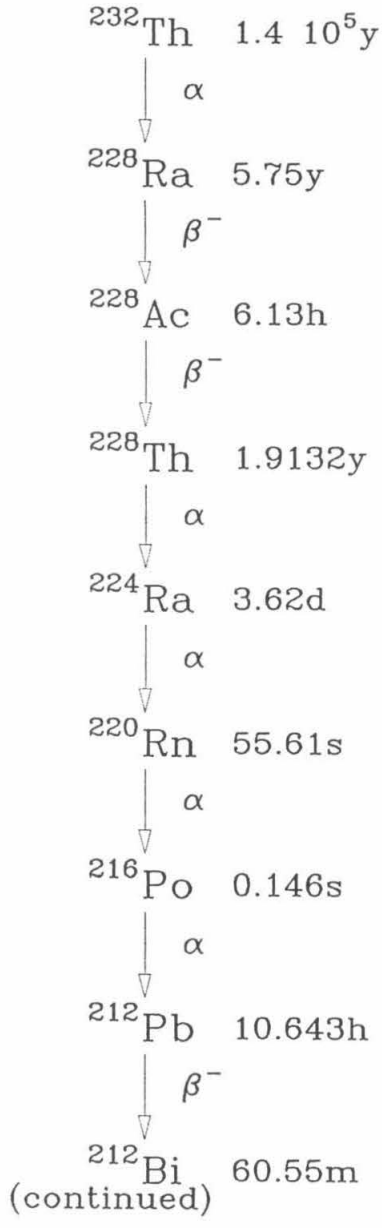

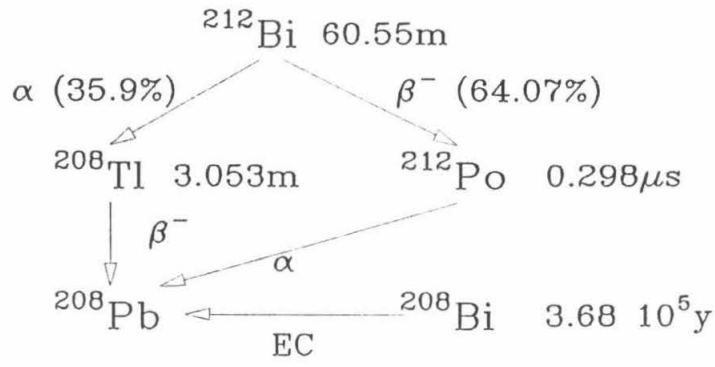

E_γ(keV)	Isotope	Intensity
209	^{228}Ac	0.05
270	^{228}Ac	0.04
328	^{228}Ac	0.03
463	^{228}Ac	0.12
911	^{228}Ac	0.29
968	^{228}Ac	0.17
844	^{224}Ra	0.28
239	^{212}Pb	0.44
300	^{212}Pb	0.03
727	^{212}Bi	0.07
277	^{208}Tl	0.03
511	^{208}Tl	0.08
583	^{208}Tl	0.32
860	^{208}Tl	0.05
2614	^{208}Tl	0.37

Figure 4.3 ^{232}Th decay chain.

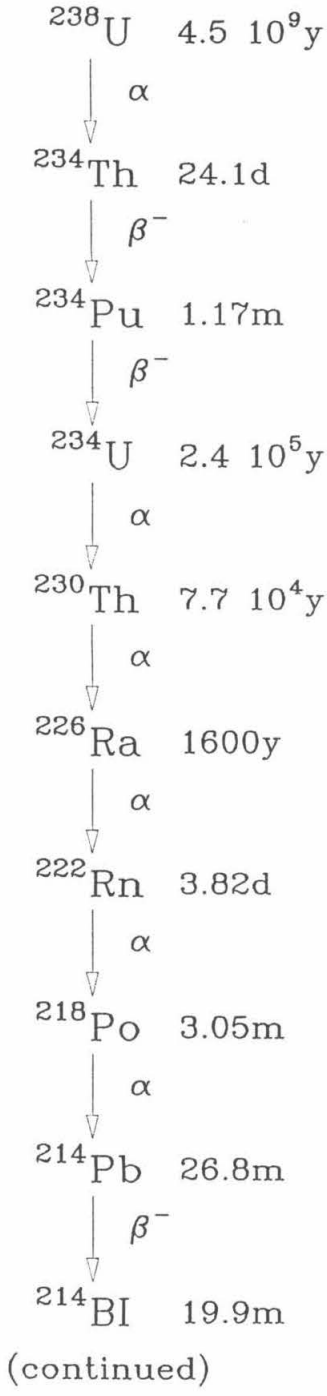

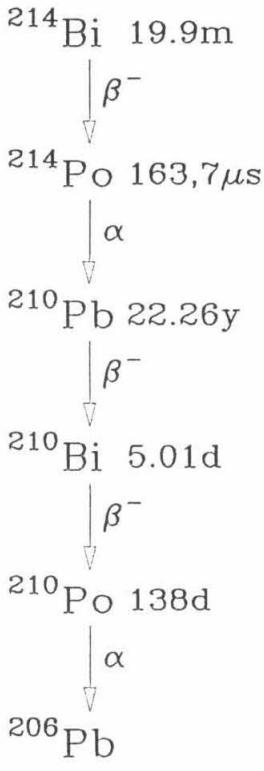

E_γ(keV)	Isotope	Intensity
48	^{234}Th	0.23
53	^{230}Th	0.28
68	^{226}Ra	0.24
185	^{222}Ra	0.05
53	^{214}Pb	0.12
242	^{214}Pb	0.075
295	^{214}Pb	0.21
352	^{214}Pb	0.38
609	^{214}Po	0.47
769	^{214}Po	0.05
1120	^{214}Po	0.16
1764	^{214}Po	0.17
304	^{214}Po	0.06

Figure 4.4 ^{238}U decay chain.

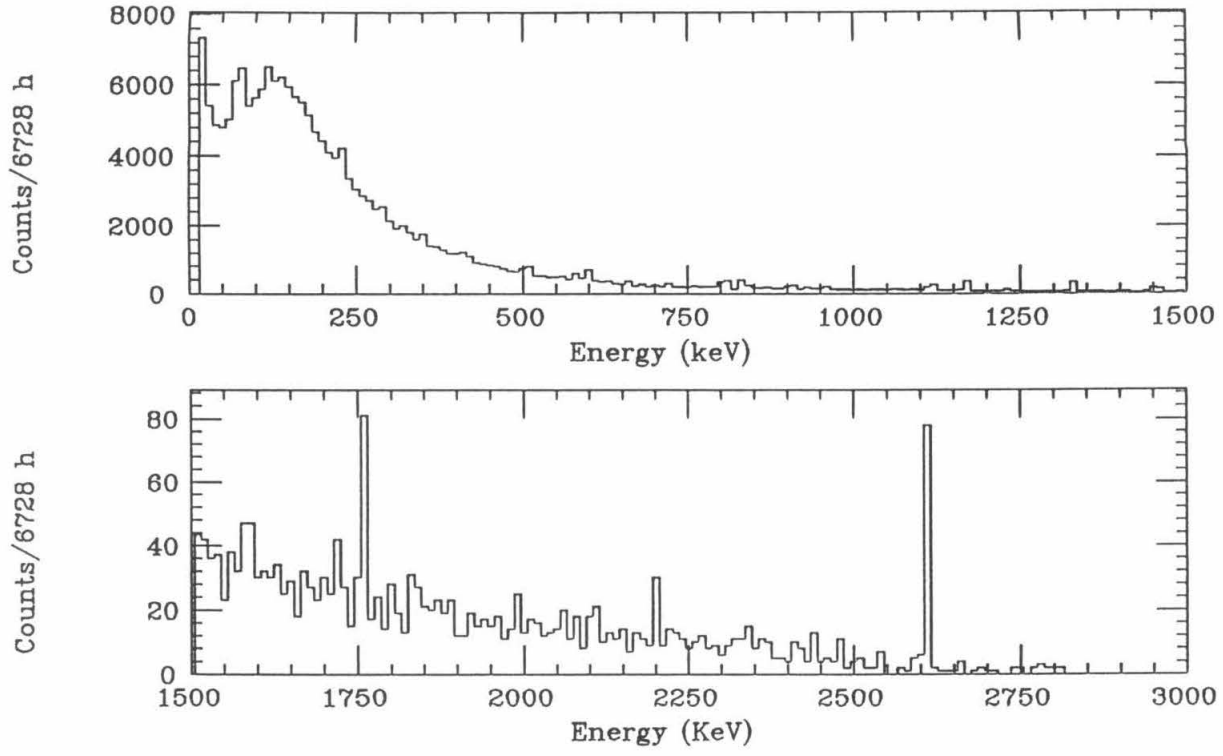

Figure 4.5 Pulseheight spectrum from 6728-hour run.

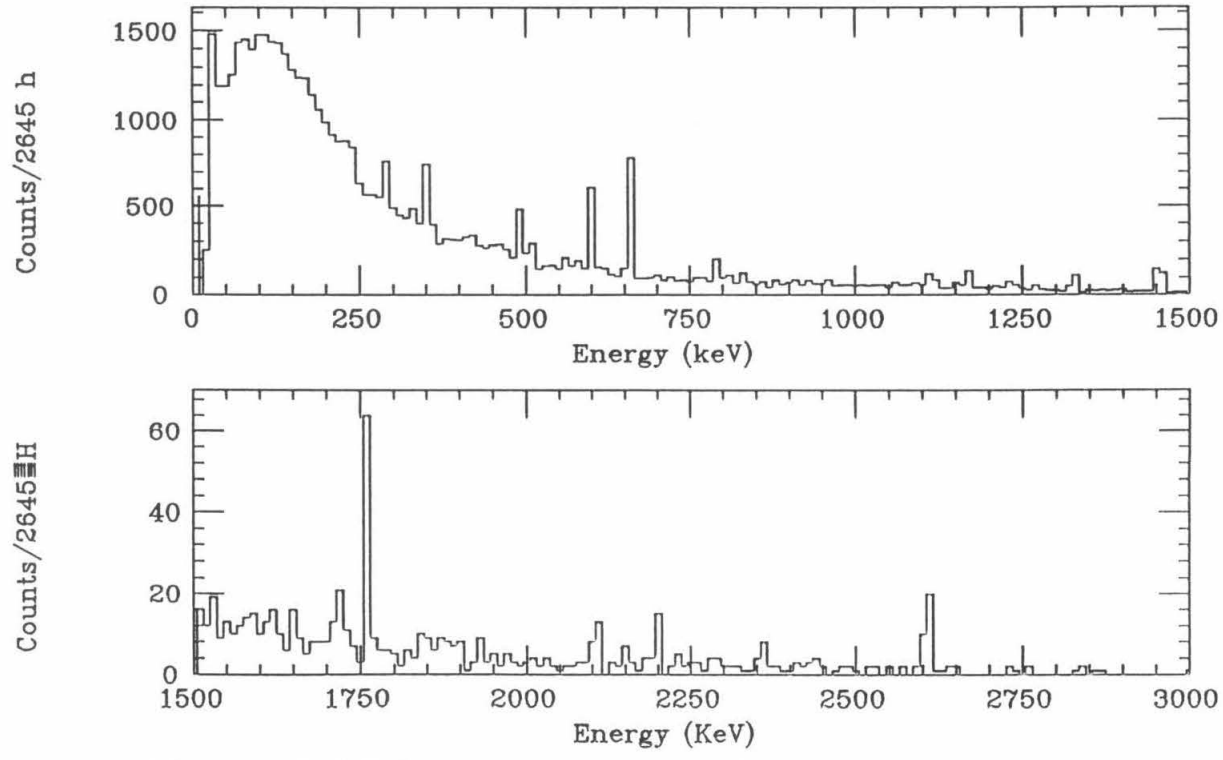

Figure 4.6 Pulseheight spectrum from 2645-hour run.

Energy (keV)	Intensity (Photons/100 decays)	Shield I (Counts/kg-y)	Shield II (Counts/kg-y)
2614.5	35.8	192 ± 23	181 ± 38
1587.9	3.7	14 ± 20	< 24
968.6	17.	113 ± 37	16 ± 9
964.6	5.5	34 ± 37	4 ± 9
911.1	29.	312 ± 41	184 ± 68
860.4	4.31	54 ± 34	50 ± 57
794.8	4.8	17 ± 34	853 ± 95
727.1	6.66	148 ± 38	44 ± 93
583.1	30.9	501 ± 62	476 ± 94
463.0	4.6	268 ± 70	150 ± 109
338.4	12.0	187 ± 84	279 ± 145
328.0	3.4	264 ± 110	< 99
300.1	3.4	278 ± 141	430 ± 164
241.0	3.95	561 ± 124	1173 ± 180
238.6	45.0	1490 ± 200	1141 ± 202
209.4	4.5	< 155	67 ± 197

Table 4.1 Observed photopeak rates for ^{232}Th lines from the Shield I and II runs with the 90 cm^3 detector.

Energy (keV)	Intensity (Photons/100 decays)	Shield I (Counts/kg-y)	Shield II (Counts/kg-y)
2447.7	1.55	11 ± 4	7 ± 17
2204.1	5.02	45 ± 8	105 ± 29
	16.0	128 ± 24	375 ± 54
1729.0	3.06	27 ± 18	< 25
1377.0	4.04	21 ± 23	84 ± 39
1238.1	5.95	123 ± 31	111 ± 69
1120.3	15.1	84 ± 36	557 ± 86
934.1	3.18	59 ± 28	205 ± 66
609.3	46.3	660 ± 62	2013 ± 139
351.9	37.3	492 ± 95	2637 ± 206
295.2	19.3	533 ± 107	1604 ± 220
186.0	3.28	5 ± 178	40 ± 213

Table 4.2 Observed photopeak rates for ^{238}U lines from the Shield I and II runs with the 90 cm^3 detector.

the more sensitive. However, the tested materials may have contained contaminants that emit gamma ray of energies below 2.0 MeV and still be considered "clean", so the photopeak rates in Shield I and II are greater than the actual background rates. Additionally, the shielding was opened, typically once a week, to insert materials for testing. This allowed ^{226}Ra gas to enter the detector and, since the nitrogen purge takes several days to push out all the gas in the shielding, the lines associated with ^{226}Ra are more intense than they would be if the system had been left sealed.

Other gamma ray lines that are not members of the natural decay chains were observed and are listed in Table 5. The photopeaks from ^{131}I, ^{134}Cs, ^{137}Cs and ^{103}Ru appeared after the shielding was opened in the time following the meltdown of the Chernobyl nuclear power plant near Kiev in the USSR. The isotopes ^{131}I and ^{103}Ru are short lived (8.0 days and 39.4 days, respectively) and disappeared gradually. The isotopes ^{134}Cs and ^{137}Cs have half-lives of 2.1 and 30.2 years, respectively, and continue to be a source of background.

Gamma rays may also be emitted by the materials inside the shielding. The ^{125}Sn and ^{40}K lines both come from internal contaminants. ^{40}K most probably came from glass in the FET. ^{125}Sn may be due to the solder connections made close to the crystal. The ^{40}K rate is much higher in Shield II because FETs were tested during the run.

Finally, gamma ray emitting isotopes may be produced by interactions between neutrons and the copper shielding and germanium crystals. There are two basic interactions: those with fast neutrons and those with thermal neutrons.

Fast neutrons at sea level are primarily cosmic in origin and, therefore, the products of fast neutron interactions are expected to decay with the appropriate half-life, once the detector is in the tunnel, (Table 6). The rate of the ^{58}Co photopeak several half-lives after the detector entered the tunnel indicates that the fast neutron flux in the tunnel is consistent with zero. Since the cross section for the ^{65}Cu(n,α2n)^{58}Co

Energy (keV)	Isotope	Intensity (Photons/100 decays)	Shield I (Counts/kg-y)	Shield II (Counts/kg-y)
1460.8	^{40}K	10.7	566 ± 43	$1689. \pm 110.$
1332.5	^{60} Co	100.	729 ± 49	741 ± 82
1173.2	^{60} Co	100.	689 ± 50	604 ± 85
1124.	^{65}Zn	50.6	350 ± 39	< 148
846.9	^{56}Co	99.9	134 ± 35	< 90
834.9	^{54}Mn	100.	511 ± 48	288 ± 72
810.8	^{58}Co	99.4	733 ± 55	382 ± 76
795.8	^{134}Cs	70	–	879 ± 100
661.6	^{137} Cs	85.1	181 ± 44	4771 ± 196
604.7	^{134}Cs	97.0	124 ± 71	1308 ± 136
569.6	^{207}Bi	97.8	97 ± 37	305 ± 103
511.	$e^+ - e^-$	–	837 ± 79	1020 ± 131
497.1	^{103}Ru	86.4	< 97	2000 ± 157
463.3	^{228}Ac		270 ± 65	< 238
427.9	^{125}Sn	29.4	$201 \pm 72.$	37 ± 171
409.8	^{228}Ac		$444. \pm 115.$	< 176
365	^{131}I	81.2	< 142	$128. \pm 168$
121.1	^{57}Co	85.6	1088 ± 171	637 ± 274
86.5	?	?	850 ± 158	< 518
77.1	^{214}Pb		1589 ± 159	< 474

Table 4.3 Observed photopeak rates for lines not associated with either of the natural decay chains from Shield I and II run with the 90 cm^3 detector.

Reaction	Gamma Energies (keV)	half-life (days)
$^{65}Cu(n,\alpha 2n)^{58}Co$	810.8	70.9
$^{63}Cu(n,2\alpha 2n)^{54}Mn$	834.8	312.5
$^{63}Cu(n,\alpha)^{60}Co$	1173.2 1332.5	1934.5
$^{63}Cu(n,\alpha 4n)^{56}Co$	1238.3 846.9	78.8
$^{63}Cu(n,\alpha p)^{59}Fe$	1099.3	44.5
$^{63}Cu(n,\alpha 3n)^{57}Co$	122.1	271.8
$^{70}Ge(n,\alpha 2n)^{65}Zn$	1124.1	244.1

Table 4.4 Fast Neutron Interactions.

Reaction	Gamma Energies (keV)	half-life c (days)
$^{70}Ge(n,\gamma)^{71}Ge \rightarrow {}^{71}Ga$	9.0	11.2
$^{74}Ge(n,\gamma)^{75}Gem \rightarrow {}^{75}Ge$	139.7	
$^{76}Ge(n,\gamma)^{77}Gem \rightarrow {}^{77}Ga$	159.7	

Table 4.5 Thermal Neutron Interactions.

reaction is not known, no limit can be placed on the neutron flux.

There are several thermal neutron capture reactions in germanium and copper that may take place (Table 7). 10 cm of borated polyethylene were used to eliminate the thermal neutron background. The products of one of the neutron capture reactions, ^{71}Ge, beta decays, the rest of the products emit no radiations above 200 keV. The 139.7 and 159.7 keV photopeaks from ^{77}Ge and ^{75}Ge are not observed and allow us to place an upper limit of 2.5×10^{-5} $cm^{-2}sec^{-1}$ on the flux of thermal neutrons in the tunnel.

As mentioned previously, ^{68}Ga is created in a fast neutron reaction $^{70}Ge(n,3n)^{68}Ge$. ^{68}Ge decays to ^{68}Ga with a 275 day half-life by electron capture. The ^{68}Ga then decays to ^{68}Zn with a 68.3 minute half-life (Figure 5). The decay of ^{68}Zn is 90 % β^+ and 10 % electron capture and has a endpoint of 1.920 MeV. The emitted positron

deposits all its kinetic energy in the crystal (up to 1.920 MeV) and then annihilates with an atomic electron into two 511 keV gamma rays, which may also interact with the crystal, extending the spectrum all the way to 2.9 MeV. The total number of ^{68}Ga atoms in the germanium crystal may be found by determining the rate of K X-rays from the decay of ^{68}Ga by electron capture after the ^{71}Ge has decayed. Since there are no fast neutrons present in the tunnel, the number of ^{68}Ge when the detector entered the tunnel may be determined from K x-ray rate, giving 3750 ± 407 ^{76}Ge atoms on April 4, 1984, when the detector first entered the tunnel. From the known sea-level fast neutron flux of 3×10^{-3}cm^{-2}s^{-1}, the cross section for the ^{70}Ge(n,3n)^{68}Ge reaction is found to be 30 mb. The cross section for ^{70}Ge(n,3n)^{68}Ge has not been measured, but the cross section for the ^{70}Ge(n,2n)^{68}Ge has and is found to be roughly 600 mb. Measurements of (n,2n) and (n,3n) on ^{203}Tl indicated the cross section for the (n,2n) reaction is about three times larger than for the (n,3n) reaction, which would give a cross section of 200 mb for ^{70}Ge(n,3n)^{68}Ge. This factor of three difference is only an order of magnitude guideline; ^{203}Tl is an odd-even nucleus , while ^{70}Ge is even-even, so the ratio of the (n,2n) and (n,3n) cross section could be quite different for ^{70}Ge. With this in mind, the 30 mb result for the (n,3n) reaction on ^{70}Ge seems reasonable.

The background rate in the tunnel outside the shielding was also measured. The tunnel background may be used to calculate the expected response of the detector for a given amount of local shielding to make certain the background from gamma rays in the tunnel is not significant. The detector was operated for 36-hours outside the local shielding. Figure 6 shows the accumulated spectrum and Tables 8 and 9 give the strength of the gamma ray peaks from the ^{232}Th and ^{226}Ra chains in the rock surrounding the tunnel. In order to determine the actual strength of each gamma line, the detector efficiency for gamma rays striking the surface of the detector cryostat was determined using the Monte Carlo program. Above 500 keV,

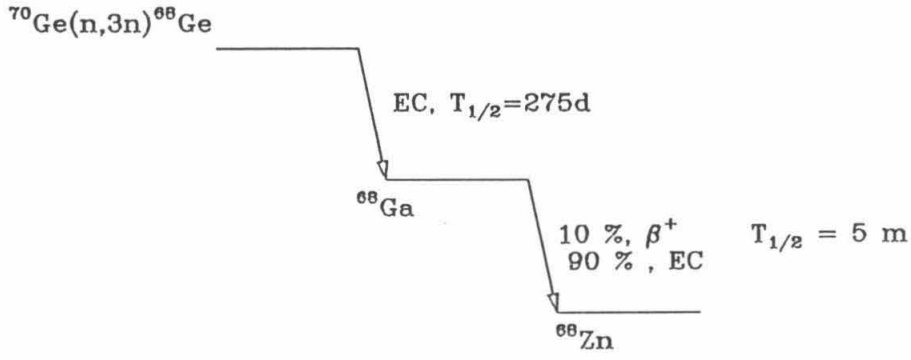

Figure 4.7 Decay process producing ^{68}Ga.

this efficiency was found to obey a power law,

$$\epsilon(E) = 0.0060E(MeV)^{-0.80}.$$

Below 500 keV, the efficiency falls off because the copper cryostat absorbs a significant fraction of the incident gamma rays, (Figure 7). The gamma flux, corrected for efficiency, is also given in Tables 4.1.1 and 4.1.1. After the strength of each gamma ray has been determined, the expected Compton continuum form a gamma ray source of that energy, and intensity is calculated by Monte Carlo and subtracted from the measured background spectrum. The remaining continuum spectrum will then be composed only of gamma rays that Compton scattered in the rock surrounding the laboratory before entering the germanium crystal. In order to determine the intensity of the continuum at each energy, the following stripping procedure is used: the continuum spectrum is first divided into 100 keV bins and, starting with the

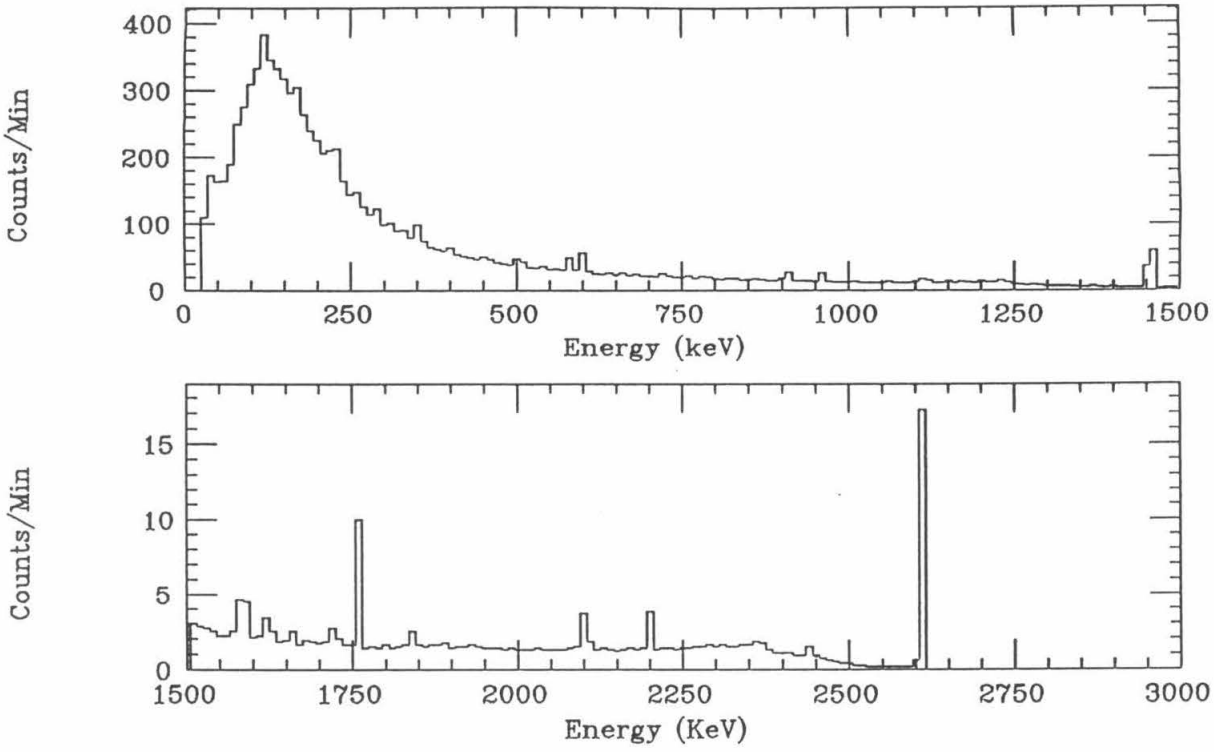

Figure 4.8 Tunnel Background spectrum for 36-hour run using the 90 cm^3 detector.

highest bin at 3 MeV, the Compton continuum is calculated for a photopeak of that energy. As before, this photopeak and Compton continuum is subtracted from the continuum spectrum. This process is repeated for the next bin and so on, from highest energy to lowest. This process is simply a deconvolution of the detector response and the measured raw data; a spectrum synthesized out of the photopeak rate corrected for photo-efficiency and the rate for each 100 keV continuum energy bin put through the detector Monte Carlo will then yield the corrected gamma ray fluxes (Figure 8).

4.1.2 Measurements with the Eight-crystal System

The overall count rate in the eight-crystal system was roughly the same per unit volume as in the 90 cm^3 detector. The background at 2 MeV was initially 1.0 counts keV^{-1} y^{-1} $(10^{23}$ ^{76}Ge nuclei$)^{-1}$ but dropped over the course of the first 2033 h to

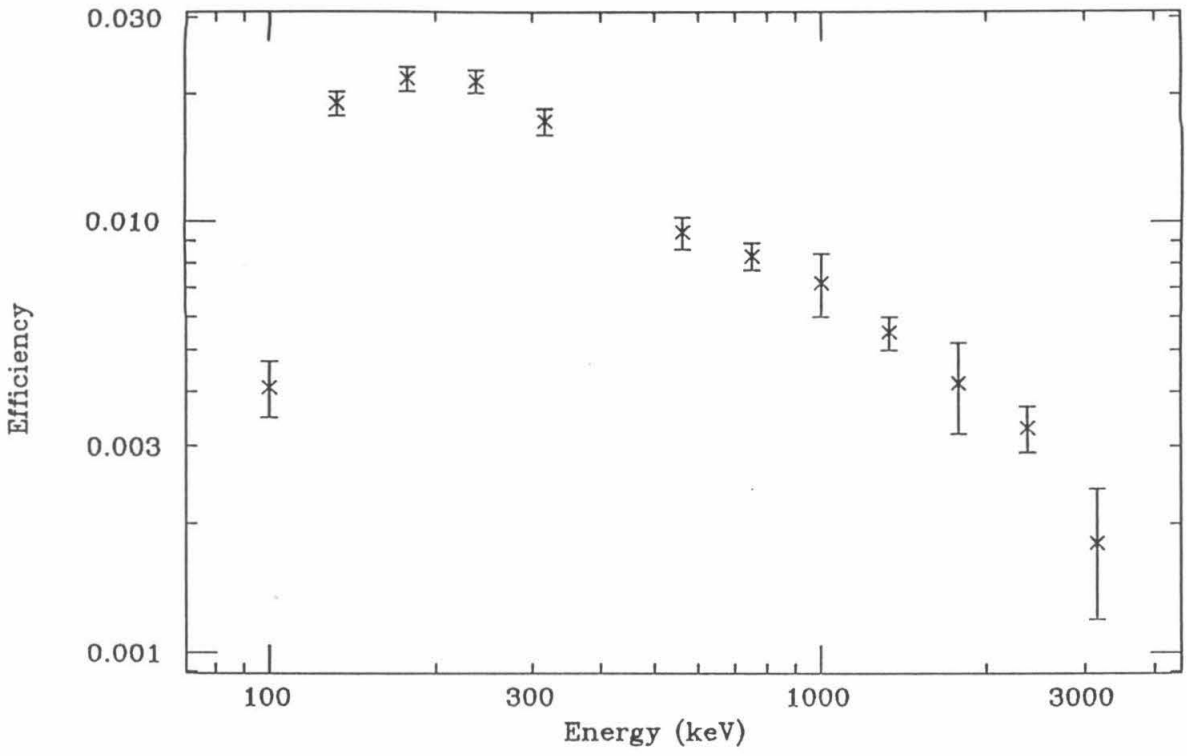

Figure 4.9 Calculated Isotropic efficiency for 90 cm^3 detector.

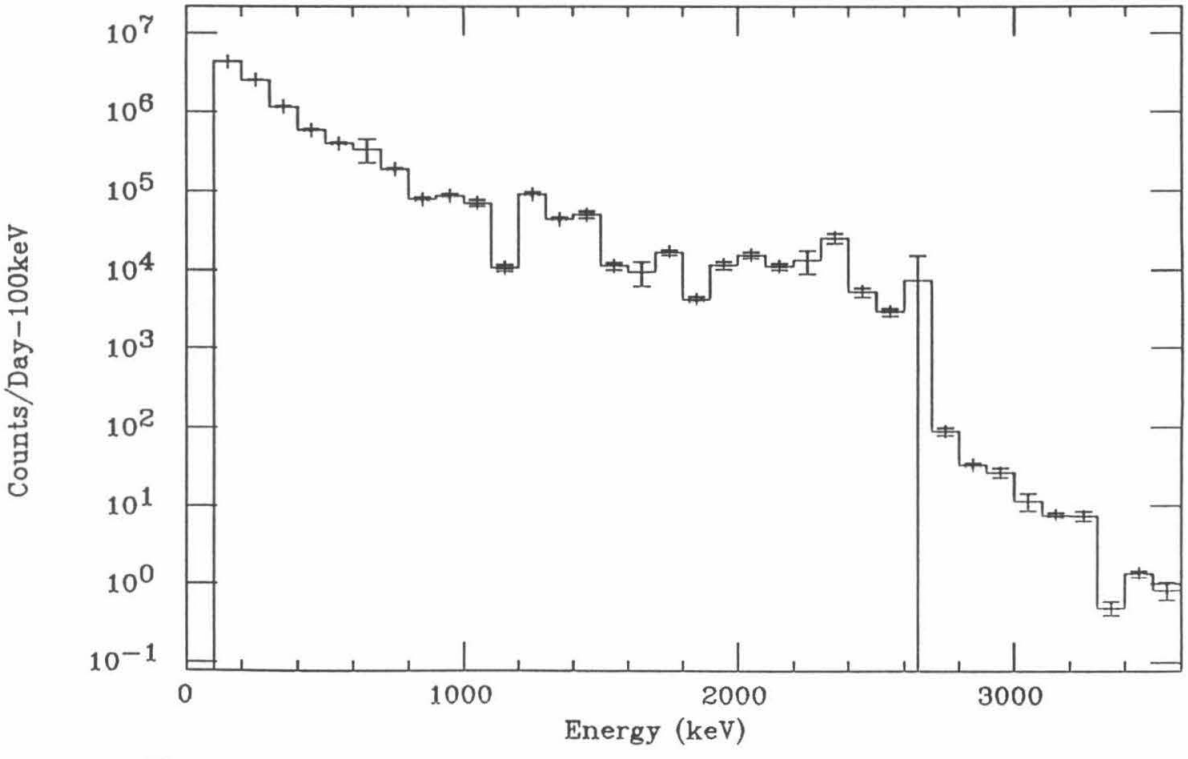

Figure 4.10 Background continuum, corrected for detector efficiency.

Energy (keV)	Branching Ratio(%)	Rate day $^{-1}$	Efficiency (%)	Corrected Rate (d^{-1} cm^{-2})
186.0	3.28	7929. ± 594.	0.02344	2198. ± 218.
295.2	19.30	16010. ± 428.	0.02039	5143. ± 366.
351.9	37.30	42625. ± 355.	0.01784	16709. ± 128.
609.3	46.30	45558. ± 244.	0.01735	30277. ± 2391.
665.6	1.57	2449. ± 166.	0.01595	1691. ± 167.
768.4	4.90	4138. ± 169.	0.01450	2992. ± 258.
785.9	1.10	1481. ± 146.	0.01403	1079. ± 137.
806.2	1.23	1004. ± 128.	0.01144	739. ± 114.
934.1	3.18	4864. ± 126.	0.01003	3846. ± 564.
1120.3	15.	12561. ± 170.	0.003	11396. ± 1841.
1155.2	1.70	1501. ± 121.	0.00815	1402. ± 240.
1238.1	5.95	5630. ± 155.	0.00784	5644. ± 693.
1281.0	1.48	728. ± 130.	0.00619	757. ± 156.
1377.7	4.04	2868. ± 107.	0.00580	3220. ± 304.
1385.3	0.78	675. ± 86.	0.00563	762. ± 117.
1401.5	1.39	1091. ± 82.	0.00533	1246. ± 144.
1408.0	2.49	1937. ± 84.	0.00530	2223. ± 220.
1509.2	2.20	2041. ± 83.	0.00517	2505. ± 307.
1538.5	0.41	336. ± 64.	0.00486	420. ± 96.
1661.3	1.15	790. ± 57.	0.00457	1058. ± 213.
1729.6	3.06	2255. ± 67.	0.00455	3124. ± 695.
1764.5	16.00	12060. ± 109.	0.00294	16986. ± 3975.
1838.4	0.38	287. ± 52.	0.00268	418. ± 129.
1847.4	2.13	1611. ± 59.	0.00262	2354. ± 598.
2118.5	1.22	826. ± 54.	0.00261	1342. ± 289.
2204.1	5.02	3625. ± 72.	0.00259	6089. ± 1070.
2293.4	0.32	164. ± 49.	0.00199	286. ± 95.
2447.7	1.55	1053. ± 52.	0.00157	1975. ± 234.

Table 4.6 Background Tunnel photopeak rates for ^{226}Ra lines. The measurement was made with the 90 cm^3 detector over a 36-hour run.

Energy (keV)	Branching Ratio (%)	Rate d^{-1}	Efficiency (%)	Corrected Rate (d^{-1} cm $^{-2}$)
209.4	4.50	3642. ± 540.	0.02344	1012. ± 163.
238.6	45.00	64875. ± 629.	0.02039	18156. ± 1121.
270.3	3.80	3288. ± 354.	0.01784	977. ± 122.
277.4	2.44	6800. ± 371.	0.01735	2062. ± 172.
300.1	3.42	5941. ± 312.	0.01595	1941. ± 165.
328.0	3.50	3284. ± 291.	0.01450	1186. ± 135.
338.4	12.00	11699. ± 292.	0.01403	4381. ± 342.
409.4	2.20	2001. ± 233.	0.01144	936. ± 135.
463.0	4.60	4211. ± 248.	0.01003	2254. ± 240.
510.8	7.75	19186. ± 275.	0.00903	11278. ± 1016.
562.3	1.00	581. ± 207.	0.00815	368. ± 135.
583.1	30.90	29414. ± 254.	0.00784	19073. ± 1582.
727.2	6.66	6028. ± 177.	0.00619	4282. ± 324.
772.1	1.60	1139. ± 133.	0.00580	825. ± 115.
794.8	4.80	5066. ± 161.	0.00563	3707. ± 331.
835.6	1.80	985. ± 151.	0.00533	736. ± 134.
840.2	1.00	958. ± 112.	0.00530	717. ± 111.
860.4	4.31	3760. ± 151.	0.00517	2864. ± 334.
911.1	29.00	22658. ± 193.	0.00486	17665. ± 2374.
964.6	5.50	4864. ± 126.	0.00457	3924. ± 623.
968.9	17.00	14555. ± 169.	0.00455	11776. ± 1866.
1587.9	3.70	782. ± 75.	0.00268	1005. ± 180.
1620.6	1.55	1370. ± 69.	0.00262	1795. ± 314.
1630.4	1.90	1213. ± 68.	0.00261	1597. ± 290.
1638.0	0.54	435. ± 54.	0.00259	575. ± 124.
2614.6	35.80	25158. ± 131.	0.00157	52001. ± 5481.

Table 4.7 Background tunnel photopeak rates for ^{232}Th lines. The measurement was made with the 90 cm^3 detector over a 36-hour run.

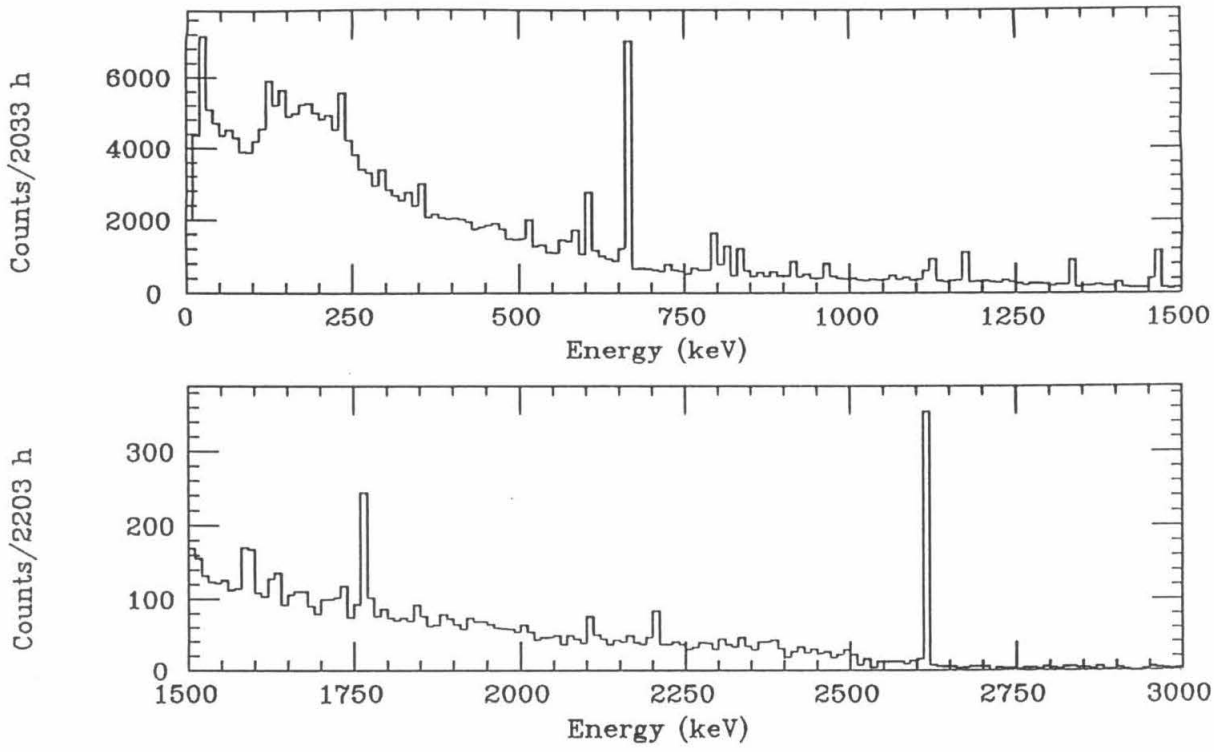

Figure 4.11 Pulseheight spectrum from the eight-crystal system for 2033 hours of operation.

an average of 0.53 in the same units. It is hoped that, as the ^{68}Ga decays, the background at 2 MeV continues to decrease. The pulseheight spectrum for the first 2033 hours is shown in Figure 9. The same ^{232}Th photopeaks appeared as in the 90 cm^3 detector (Table 10). The 2614 keV line was increased by roughly 30 %, most of which can be accounted for by the increased of efficiency for the the larger crystals. The other lines did not increase significantly, except for the 911.1 keV lines, which mysteriously increased by 300 %.

The ^{238}U photopeak rates (Table 11), with the exception of the 1120 keV line, in general decreased. This was expected since the local shielding was not opened and the nitrogen pressure kept the ^{226}Ra gas from entering the local shielding.

The lines associated with the Chernobyl meltdown (Table 12) were also present. As expected, the ^{131}I and ^{103}Ru have almost completely decayed away, while the ^{134}Cs and ^{137}Cs are still present in significant amounts. The lines from the germanium-

Energy (keV)	Intensity (Photons/100 decays)	Measured Rate (Counts/kg-y)	Percent change
2614.5	35.8	245 ± 29	32 ± 26
968.6	17.	164 ± 45	129 ± 79
964.6	5.5	112 ± 33	11 ± 49
911.1	29.	282 ± 46	500 ± 274
583.1	30.9	$413 \pm 64.$	2 ± 28
238.6	45.0	840 ± 106	41 ± 22

Table 4.8 Observed photopeak rates for ^{232}Th lines during 2033 h run of the eight-crystal system.

Energy (keV)	Intensity (Photons/100 decays)	Measured Rate (Counts/kg-y)	Percent Change
2447.7	1.55	15 ± 13	43 ± 134
2204.1	5.02	44 ± 17	5 ± 59
1764.5	16.0	$98. \pm 27.$	-28 ± 28
1238.1	5.95	34 ± 43	-75 ± 100
1120.3	15.1	239 ± 48	192 ± 77
934.1	3.18	24 ± 49	-56 ± 156
609.3	46.3	264 ± 57	-182 ± 95
351.9	37.3	535 ± 74	52 ± 36
295.2	19.3	142 ± 68	-55 ± 77

Table 4.9 Observed photopeak rates for ^{238}U lines during 2033 h run of the eight-crystal system. Changes are compared to Shield I.

Energy (keV)	Isotope	Intensity (Photons/100 decays)	Measured Rate (Counts/kg-y)	Percent Change
1460.8	^{40}K	10.7	674 ± 51	-10 ± 10
1332.5	^{60} Co	100.	471 ± 49	-49 ± 10
1173.2	^{60} Co	100.	522 ± 51	-40 ± 11
1124.	^{65}Zn	50.6	461 ± 48	13 ± 18
846.9	^{56}Co	99.9	116 ± 34	62 ± 61
834.9	^{54}Mn	100.	513 ± 52	-23 ± 13
810.8	^{58}Co	99.4	982 ± 68	12 ± 12
661.6	^{137} Cs	85.1	4203 ± 124	18 ± 84
600.8	^{125}Sb	97.0	858 ± 74	608 ± 103
569.6	^{207}Bi	97.8	214 ± 47	243 ± 154
511.	$e^+ - e^-$		708 ± 78	-45 ± 13
497.1	^{103}Ru	86.4	< 90	
463.3	^{228}Ac		< 100	< -63
427.9	^{125}Sn	29.4	75 ± 101	-66 ± 110
409.8	^{228}Ac		< 101	< -77
365	^{131}I	81.2	< 107	27 ± 45
121.1	^{57}Co	86.4	$675. \pm 105.$	
86.5			< 107	
77.1	^{214}Pb		136 ± 108	-91 ± 75

Table 4.10 Observed photopeak rates for lines not in either of the natural decay chains for 2033 h run of the eight-crystal system.

neutron and copper neutron reactions are also present with roughly the same intensity as in the 90 cm^3 setup. This is to be expected; they come from the germanium itself and the first few centimeters of copper surrounding the crystals, so they should have the same intensity per unit volume for all similar systems. The ^{40}K photopeak rate did not decrease, indicating that the contamination did most probably come from the FETs, all of which contain contamination of this type.

4.2 Determination of $\beta\beta$ decay rates

Once the experiment has been run for some time, the data collected during the experiment must be analyzed and the implications of the experiment extracted.

The data analysis consists of two steps for each decay mode: first, a determination must be made as to whether or not evidence for the decay mode is present. The next step depends on the outcome of the first. If evidence for the decay is present, the half-life for the mode must be determined and interpreted in terms of fundamental quantities. If no evidence for the decay is seen, an upper limit for the decay rate must be determined and interpreted in terms of upper limits of fundamental quantities.

The determination of whether a signal is present or not in any experiment must be made in an unbiased fashion. A test must be devised which not only indicates the presence or absence of a signal, but also gives some confidence for this conclusion. This chapter describes the statistical tests and results for the $2\nu, 0\nu$ and χ^0 decay modes. Since the methods for extracting limits for the 2ν and χ^0 modes are quite similar, they are described together.

4.2.1 $0\nu\beta\beta$ Mode

The signature for $0\nu\beta\beta$ decay is a peak in the pulseheight spectrum at 2040.71 keV. Since the nucleus is quite heavy compared to the two electrons, the width of the peak will be completely determined by the resolution of the germanium detector at this energy, which is 2.6 keV, FWHM or about 6 ADC channels. This portion of the spectrum is shown in Figure 10. Since the data in this region are fairly sparse (about a third of the ADC bins have no counts in them), using the Gaussian limit as an approximation for the Poisson distribution on the number of counts in each bin is not correct; the standard deviation on the number of counts on each bin is not $1/\sqrt{N}$. This is always the case when N $<$ 20. For this reason, the usual χ^2 statistic $1/\sigma^2(y_i - y(x_i))^2$ is not appropriate for determining the goodness-of-fit for the function $y(x)$ to data y_i at points x_i. Baker and Cousens [37] derive a more

appropriate statistical treatment with

$$\chi^2 = -2\sum_i(-y_i + y(x_i) + y_i ln\frac{y_i}{y(x_i)}),$$

the minimization of which will give the correct values for the fit parameters. Using this statistic for χ^2, the region around 2041 keV is searched for a peak; there are two methods of carrying out this search. First, the region around 2041 keV is fit with a succession of Gaussians each with the peak at succeeding energies. A plot of the peak energy versus χ^2 should show a minimum at the physical value of 2041 keV if a signal is present. If a statistically significant minimum is present, $0\nu\beta\beta$ decay is assumed to take place. A fit is then performed with the mean peak value fixed at the physical energy, giving the detected decay rate. On the other hand, if no minimum appears near the physical value of decay energy, $0\nu\beta\beta$ decay has not been detected. In this case, the mean value is fixed at 2041 keV and the normalization increased, until the value of chi-squared increases by one over the best-fit value. This gives the upper limit on the number of counts in the peak at the 68 % confidence level. The upper limit at 90 % confidence level is 1.4 times greater. A series of fits performed for the function

$$N(E) = N_0 e^{-\frac{(E-E_0)^2}{2\sigma^2}} + C$$

yields a plot of decay energy versus χ^2 shown in Figure 11. Clearly, no minimum of significance appears near the physical endpoint of 2041 keV and, therefore no signal is present.

A second method may be used. The peak region is fit with the function above with E_0=2040.71 keV and σ = 1.11 keV to give $\chi^2(\nu = 2)$. A second fit is done using the function $N(E) = C$ alone to give $\chi^2(\nu = 1)$. Then,

$$\lambda = \chi^2(\nu = 2) - \chi^2(\nu = 1)$$

will be a χ^2 distribution with one degree of freedom and the significance will give the significance of the added degree of freedom. Performing this fit for the spectrum

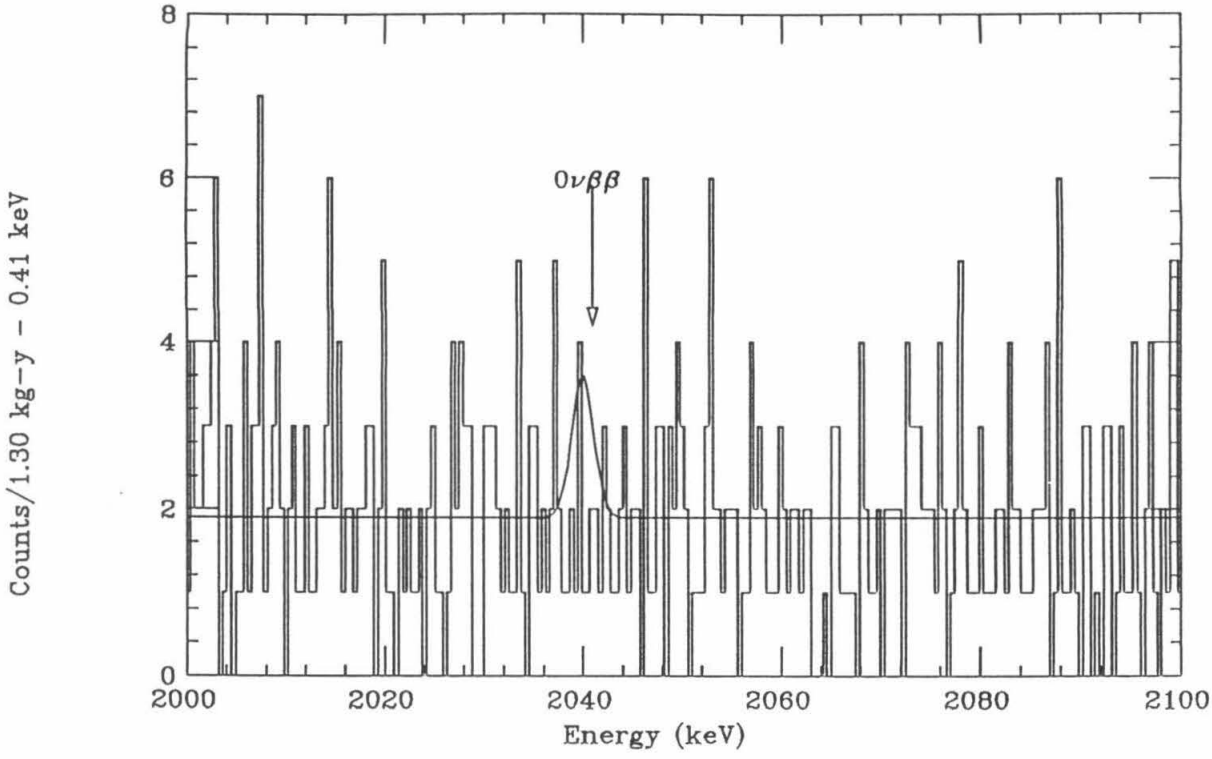

Figure 4.12 Pulseheight spectrum at 2.0 MeV for 1.30 kg-y.

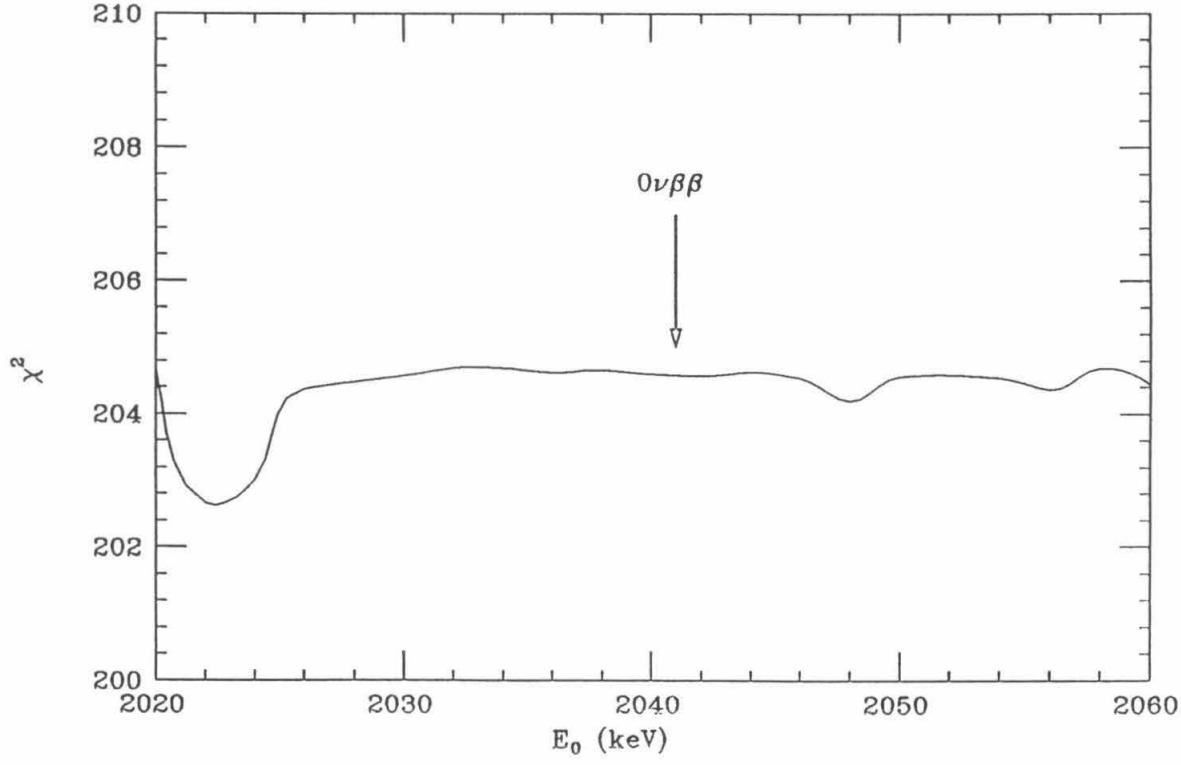

Figure 4.13 Endpoint versus χ^2 plot for spectrum in Fig. 1.

in Figure 12 gives

$$\lambda = 205.27 - 204.58 = 0.69,$$

which has a significance of 50 %, indicating that the added parameter does not significantly improve the fit. Again, no signal appears to be present.

To determine the upper limit of the number of counts in the $0\nu\beta\beta$ decay peak, a fit is performed with the peak energy set to 2040.71 keV, which yields $-0.56^{+1.8}_{-1.5}$ counts in the peak. Two problems are evident: first, the central value is in an unphysical region and second, the asymmetric errors indicate that Gaussain statisitcs are not a good approxiamtion to Poisson statistics. There are various methods of handling this sort of situation, the most straightforward being the Monte Carlo method. In the Monte Carlo method, many spectra with the same characteristics as the measured spectrum are generated and fit to give a distribution of central values for the number of counts in the peak. This distribution should then correspond to the true distribution for the number of counts in the peak. The 90% confidence level upper limit of the number of counts is then determined by taking the number of counts corresponding to the point at which 90% of the the area under the distribution in the physical region is encompassed. For the spectrum shown in Figure 12, this procedure gives an upper limit of 6.1 counts at 90% c.l. To convert this to a lower limit for the half-life, the formula

$$\Gamma < \frac{N_{upper}}{N_{nuclei}t}, \quad T^{0\nu}_{1/2} > \frac{ln2}{\Gamma}$$

is used to give

$$T^{0\nu}_{1/2} > 1.2 \times 10^{23} (\text{y } 90\% \text{ c.l.})$$

and

$$T^{0\nu}_{1/2} > 3.0 \times 10^{23} (\text{y } 68\% \text{ c.l.}).$$

To obtain a lower limit for the half-life of the $0^+ \rightarrow 2^+$ transition, a similar search is carried out at the region around 1480.5 keV (Figure 12.) In this case, a 559 keV

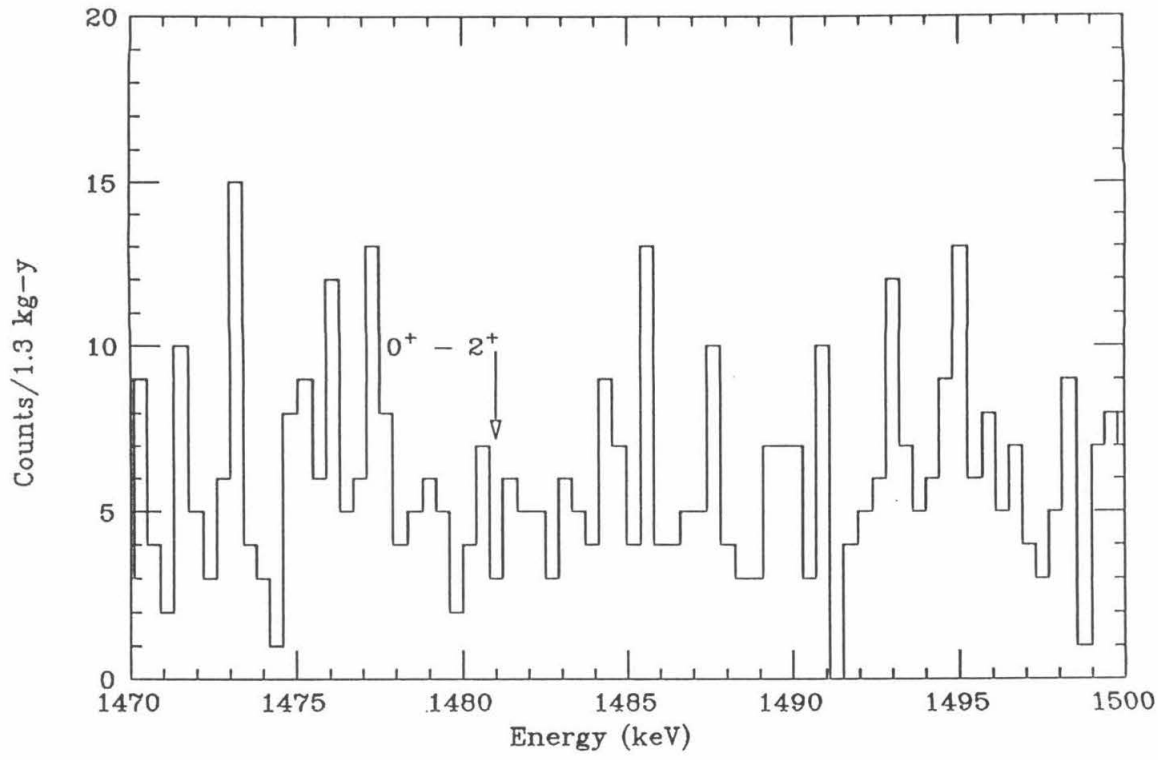

Figure 4.14 Histogram for 1.30 kg-y to the $0^+ \rightarrow 2^+$ transition energy 1480.5.

gamma ray is emitted from the daughter nucleus when it decays to its ground state. If this gamma ray deposits any energy in the crystal before escaping, the count will not be in the 1480.5 keV peak, so the limit on the number of counts must be corrected for the probability of this gamma ray's escape, which is determined by Monte Carlo to be 30 %. Carrying out the search as above, we find an upper limit of 30 counts (90 % c.l.), which gives a lower limit of

$$T^{0\nu}_{1/2}(0^+ \rightarrow 2^+) > 2.0 \times 10^{22}\text{y (90\% c.l.)}$$

and

$$T^{0\nu}_{1/2}(0^+ \rightarrow 2^+) > 6.8 \times 10^{22}\text{y (68\% c.l.)}.$$

4.2.2 2ν and $\chi^0\beta\beta$ Decay

Both two neutrino double beta decay and double beta decay with Majoron emission result in undetected particles in the final state. The energy of the emitted electrons is distributed over a large hump between zero and the double beta decay endpoint energy of 2041 keV. For ^{76}Ge, the peak of the 2ν total electron kinetic energy distribution is near 700 keV, while for $\chi^0\beta\beta$ decay, the peak of the distribution is near 1500 keV.

Typical calculations of the $2\nu\beta\beta$ decay half-lives in ^{76}Ge are of the order of 10^{22-21} years, which translates roughly to 150 to 1500 counts per year above 700 keV in the eight-crystal system. In this region, which is 53 % of the 2ν spectrum, we observe 21,045 counts in 1.30 kg-y. Taking the 90% confidence level upper limit on this number of counts gives a half-life limit of

$$T_{1/2}^{2\nu} > 6.4 \times 10^{18}\text{y (90\% c.l.)},$$

which is not sensitive to the predicted rates. In order to improve this limit, we must understand, calculate and subtract the various backgrounds.

Background counts, as discussed in Chapter 4, come from several sources: gamma rays from internal contaminants, gamma rays from the ^{238}U and ^{232}Th in the lead shield, gamma rays that penetrate the shield from outside and positrons (and the associated annihilation gamma rays) from the decay of ^{68}Ga. A Monte Carlo calculation using the measured gamma fluxes in the tunnel (Chapter 4) reveals that gamma rays penetrating the local shielding were significant only for Shield I; the additional shielding cut the gamma flux to an insignificant level for Shield II and the eight-crystal system.

The expected spectrum for the cosmogenic isotopes in the copper was determined in the same way: gamma rays for each isotope were generated in random positions in the cryostat and surrounding shielding and tracked through to the ger-

manium crystal. Each spectrum was normalized to the photopeak. In cases where several gamma rays were emitted in a cascade, all the gamma rays were tracked simultaneously to account for sum peaks.

Gamma rays from internal contaminants had to be calculated in the same way, except that this time some assumption had to be made about the position distribution of the source. Extensive calculations show that there is little dependence on the position of the source. The resulting detector response spectrum was, as before, normalized to the observed photopeak height.

The expected spectrum form ^{68}Ga β^+ decay was determined by simulating positron emission inside the crystal and tracking the β^+ and two 511 keV annihilation gamma rays. The normalization was determined by scaling the rate to the rate observed in the 90 cm^3 detector.

Finally, possible contamination of ^{238}U and ^{232}Th in outer lead shield had to be considered. Since both decay chains end with lead isotopes, it is not unreasonable to expect both chains to be present in lead. Monte Carlo simulation of the expected spectra from contamination of each chain indicated that ^{232}Th was not present in significant amounts while ^{238}U was present at the 1 ppm level when averaged over the inner 5 cm of the lead shield. This was to be expected; lead tested with the 90 cm ^{3} detector showed no evidence of ^{232}Th while gamma lines from the ^{238}U chain were present. The expected spectrum from ^{238}U was calculated and normalized to the rate of the 1764 keV gamma line measured after the shielding had been closed long enough for the ^{226}Ra to decay away.

Each of these spectra was subtracted in turn, resulting in the spectrum shown in Figure 15. The agreement between the data and calculated background is good above about 700 keV (see next section). Below 700 keV, many counts remain. They have three possible sources: incomplete charge collection, weak gamma lines and underestimation by the Monte Carlo program.

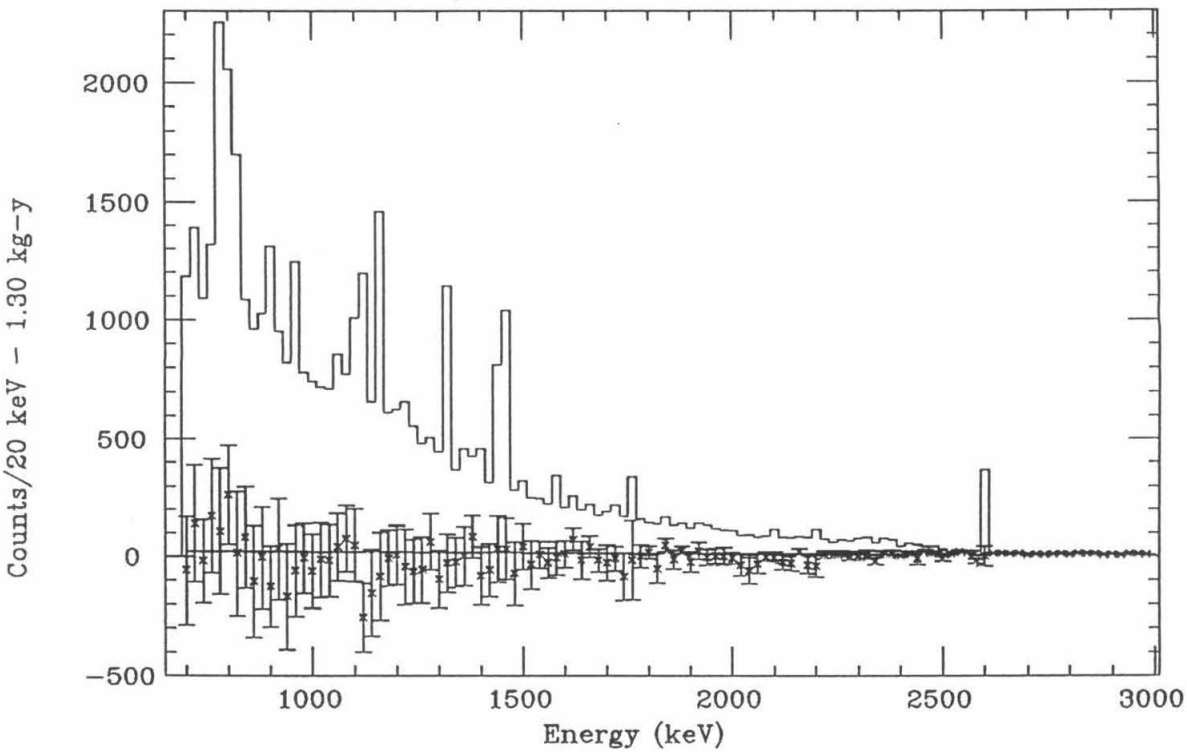

Figure 4.15 Spectrum above 700 keV after background subtraction. Histogram shows the raw data, the errors show the residual spectrum after background subtraction and the solid line is the best fit of the expected $2\nu\beta\beta$ decay energy spectrum and a linear background.

Incomplete charge collection means that all the ionization electron produced in a full energy gamma interaction may not be collected. This is caused by a non-neutral electric field at the closed end of the detector. Charge collected here does not contribute to the current pulse but instead slowly discharges. Thus, not all the gamma rays that deposit all their energy in the crystal will contribute to the full energy peak, leading to an underestimate of the Compton continuum.

Monte Carlo studies show that above 1 MeV, for every full energy count, there are about 5 counts in the Compton continuum. Thus, a gamma line may not be statistically significant above the background, but may contribute significantly to the rest of the spectrum.

Finally, tests with the Monte Carlo program (see Appendix) indicate that the program may underestimate the number of counts at low energies. This appears to be a fundamental problem with the manner in which the simulation is carried out.

There are also counts above the highest subtracted gamma line at 2614 keV. The ^{238}U chain has a several very weak gamma lines extending up to 3270 keV. The total intensity of these lines is about 10% of the strength of the ^{238}U line at 2447 keV (Figure 4), the photopeak of which is barely visible (Table 9). The measured rate between 2620 keV and 3270 keV is 0.230 keV^{-1}kg^{-1}y^{-1}. The rate above 3270 keV falls to 0.032 keV^{-1}kg^{-1}y^{-1}, indicating the counts in this region come from the ^{238}U chain. A crude Monte Carlo calculation indicates that ^{238}U contamination in the lead shield could account for about 10% of the observed rate. The remainder could come from a ^{214}Bi source inside the copper shielding.

Once this subtraction has been carried out, a limit on the number of $2\nu\beta\beta$ counts must be obtained. The most straightforward way of doing this is simply to integrate over the region from 700 to 2041 keV, which gives -522 ± 1136 counts, which translates to a half-life of

$$T_{1/2}^{2\nu} > 2.0 \times 10^{20}\text{y (90\% c.l.)},$$

or

$$T_{1/2}^{2\nu} > 5.0 \times 10^{20}\text{y (68\% c.l.)},$$

The residual spectrum may be taken into account crudely by assuming the density of weak photopeaks is constant. The Compton continua of these peaks along with the counts from incomplete charge collection will pile up to make a continuum that decreases linearly with energy. This is then folded with the power law efficiency for the detector. This gives a fit function which will be roughly linear

$$\frac{dN}{dE} = aS_{2\nu}(E) + b + cE,$$

where $S_{2\nu}$ is the total electron kinetic energy distribution function for $2\nu\beta\beta$ decay. The best fit when a is allowed to vary gives $a = -1882 \pm 2000$ which leads to an upper limit of

$$N_{2\nu} < 4547 \text{ counts or}$$

$$T_{1/2}^{2\nu} > 1.4 \times 10^{20}\text{y(90 \% c.l.)},$$

so fitting with a linear background function does not significantly improve the limit. This indicates the sensitivity is limited by the statistics of the data.

Recently, an observation of double beta decay with Majoron emission has been reported [38]. The signature for $\chi^0\beta\beta$ decay is similar to that of $2\nu\beta\beta$ decay. In the case of $\chi^0\beta\beta$ decay, however, the broad peak of the spectrum is shifted to about 1550 keV. Our search for $\chi^0\beta\beta$ decay, therefore, is carried out from 1500 to 2800 keV. Since most of the counts from $\chi^0\beta\beta$ decay will occur at a higher energy than those from $2\nu\beta\beta$ decay, the experiment will be more sensitive to $\chi^0\beta\beta$ decay since the backgrounds decrease at higher energies. As before, we begin by integrating the raw data spectrum from 1500 keV to 2041 keV (43 % of the $\chi^0\beta\beta$ decay spectrum), which gives 4984 counts, which translating to a limit of $T_{1/2}^{\chi^0} > 5.3 \times 10^{19}$ y, (90% c.l.).

Turning next to subtracted data spectrum and integrating over the same interval give a total of -64 ± 336 counts or

$$T^{\chi^0}_{1/2} > 8.0 \times 10^{20} y(90\%\ c.l.)$$

or

$$T^{\chi^0}_{1/2} > 1.0 \times 10^{21} y(68\%\ c.l.).$$

As with the $2\nu\beta\beta$ decay limit, for the final fit we use a linear background function along with the electron energy distribution function

$$\frac{dN}{dE} = aS_{\chi^0}(E) + b + cE$$

The best fit is $a = -333 \pm 682$ counts which gives a half-life limit

$$T^{\chi^0}_{1/2} > 8.0 \times 10^{20}\text{y (90\% c.l.)}$$

from our spectrum. As with the 2ν result, fitting with a linear background function does not improve the limit. This is in contradiction with the reported result $T^{\chi^0}_{1/2} = (6 \pm 1) \times 10^{20}$ y.

4.2.3 Comparison with Other Experiments

Results from the other measurements of ^{76}Ge are shown in Table 2. The best limit for $0\nu\beta\beta$ decay, obtained by the UCSB/LBL [29] experiment, is $T^{0\nu}_{1/2}[0^+ \rightarrow 0^+] > 5 - 8 \times 10^{23}$ y, (68 % c.l.). The limit 5×10^{23} y was obtained by simply considering the fluctuation of the observed flat backgrounds, while the limit 8×10^{23} y comes from a least squares fit with a Gaussian peak on a flat background. The method described in Chapter 4 was not applied to these data. Finally, For the $0^+ \rightarrow 2^+$ transition, the UCSB/LBL group reports a limit $T^{0\nu}_{1/2}0^+ \rightarrow 2^+ > 5 \times 10^{22}$ y, (68 % c.l.).

$2\nu\beta\beta$ decay has not yet been observed in ^{76}Ge. The best limits come from this experiment and the UCSB/LBL group and are $T^{2\nu}_{1/2} = 7 \times 10^{19}$ y and $T^{2\nu}_{1/2} = 8 \times 10^{19}$ y, respectively.

Group	Background $keV^{-1}y^{-1}(10^{23}\ ^{76}Ge)^{-1}$	Volume cm^3	$T^{0\nu}_{1/2}$ $\times 10^{23}$ y (68 %)
Zaragosa	6	400	0.2
Osaka	0.6	1100	0.7
Guelph/Queens	0.5	600	1.2
Milano I	4	115	3.2
Milano II	0.8	138	
PNL/USC	0.4	135	1.4
UCSB/LBL	0.3	1300	5-8
This exp.	0.53	1100	3.0
Erevan/ITEP	0.1 (?)	90(1100) [1]	1 (?)

Table 4.11 Summary of results from all ^{76}Ge measurements.

Finally, for $\chi^0\beta\beta$ decay, the UCSB/LBL group reports a limit of $T^{\chi^0}_{1/2} > 2 \times 10^{21}$ y, (90 % c.l.), also in contradiction with the PNL/USC result.

Chapter 5

Interpretation of Measurements

The implications of the limits of the half-lives are now analyzed in terms of fundamental physical quantities. For the neutrinoless mode of double beta decay, the half-life limits are used to give limits on the effective right-handed coupling constants $< \lambda >$ and $< \eta >$ and effective neutrino mass, $< m_\nu >$. Similarly, for the mode with Majoron emission, the half-life limit gives a limit on the $\chi^0 - \nu$ coupling constant, g_{ee}. The two neutrino half-life limit, however, serves only as a check on the matrix element calculations; it is an allowed process in the Standard Model and contains no "new" physics.

5.1 Neutrinoless Double Beta Decay

5.1.1 $0^+ \rightarrow 0^+$ Transition.

The neutrinoless double beta decay rate from Chapter 2 is

$$\begin{aligned}(T^{0\nu}_{1/2}(0^+ \rightarrow 0^+))^{-1} &= C_1 \frac{< m_\nu >^2}{m_e^2} + C_2 < \lambda > \frac{< m_\nu >}{m_e} + \\ & C_3 < \eta > \frac{< m_\nu >}{m_e} + C_4 < \lambda >^2 + \\ & C_5 < \eta >^2 + C_6 < \lambda >< \eta > .\end{aligned}$$

The coefficients C_i are given in Table 2.2.2 for the calculation by Do et. al. [13]. Limits on the quantities $< \lambda >, < \eta > and < m_\mu >$ are determined from the measured limit $T^{0\nu}_{1/2}$. Since only an upper limit is measured for $T^{0\nu}_{1/2}$, all points in

a region *outside* an ellipsoid in $(< \lambda >, < \eta >, < m_\nu >)$ space will be excluded by the measurement. The best way to see this is by projecting the surface of the ellipsoid onto the $(< \lambda >, < m_\nu >)$, $(< \eta >, < m_\nu >)$ and $(< \lambda >, < \eta >)$ planes, as shown in Figures 1, 2 and 3. The upper limits on the magnitude of $< \lambda >, < \eta >$ and $< m_\nu >$) are determined by how far the ellipse extends along the axis of each parameter. Since the coefficients C_i depend on the calculation of the nuclear matrix elements, the excluded region varies depending on which nuclear matrix elements are used. Only Haxton & Stephenson [12] have carried out the calculation of the matrix elements necessary to include right-handed currents and the exclusion plots shown in Figures 1, 2 and 3 are from this calculation. The calculations of Vogel at. al [22] and Klapdor & Grotz [23] do not include right-handed currents, so they only give limits for $< m_\nu >$ in the absense of right-handed currents. The results for each calculation are shown in Table 1. As is clear from Table 1, the limits on the neutrino mass vary by a factor of almost ten for differing calculations of the nuclear matrix elements.

Limits from other attempts to detect $0\nu\beta\beta$ decay in ^{76}Ge are shown in Table 4.2.3. These limits imply an upper limit of the Majorana mass in the range 5.8 - 0.2 eV. Clearly, a resolution of the nuclear matrix element question is necessary to clarify these results.

Author	$< m_\nu >$ (eV) <	$< \lambda > \times 10^{-5}$ <	$< \eta > \times 10^{-5}$ <
Vogel [22]	16	(1.3)	(1.2)
Haxton [12]	5.8	0.14	0.13
Klapdor [23]	1.6	(0.040)	(0.0037)
Faessler [24]	1.9	(0.047)	(0.0043)

Table 5.1 Upper limits for $< m_\nu >$, $< \eta >$ and $< \lambda >$ for measured half-life limit of $T^{0\nu}_{1/2} > 1.0 \times 10^{23}$ years at 90% c.l. Limits for the right-handed couplings $< \lambda >$ and $< \eta >$ shown in parenthesis are found by using the coefficients obtained by muuliplying the calculation of C_1 by the value of C_i/C_n calculated by Haxton & Stephenson [12] and compiled in Doi et. al. [13].

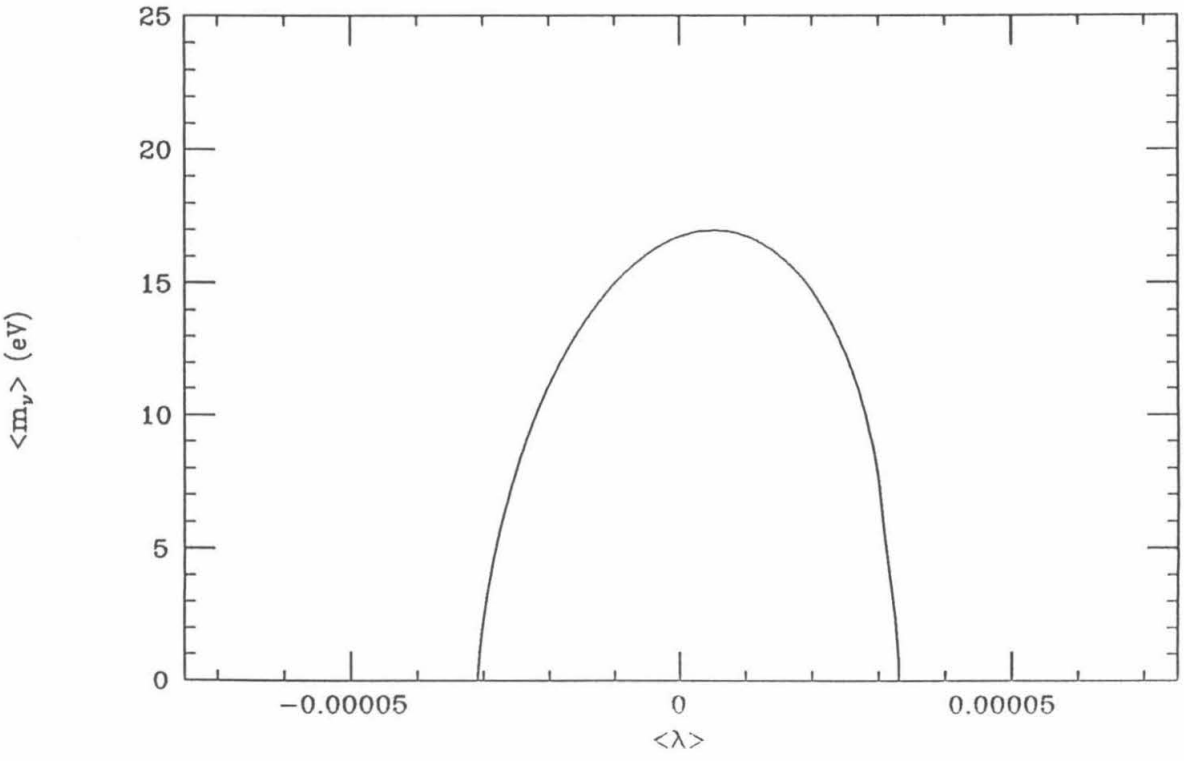

Figure 5.1 90 % confidence level excluded region along $< m_\nu > - < \lambda >$ plane for $T^{0\nu}_{1/2} > 1 \times 10^{23}$ y The values for C_i are calculated by Haxton & Stephenson and are compiled by Doi et. al.

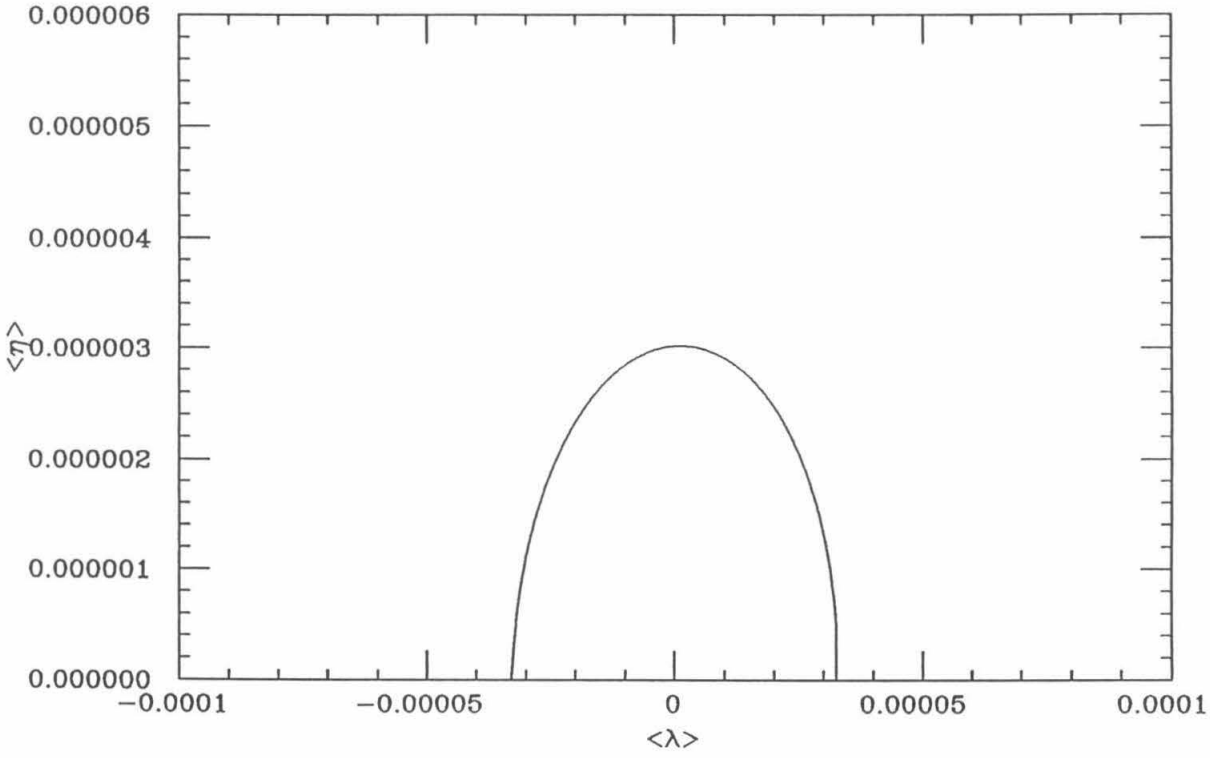

Figure 5.2 90 % confidence level excluded region along $< \lambda > - < \eta >$ plane for $T^{0\nu}_{1/2} > 1 \times 10^{23}$ y. The values for C_i are calculated by Haxton & Stephenson and are compiled by Doi et. al.

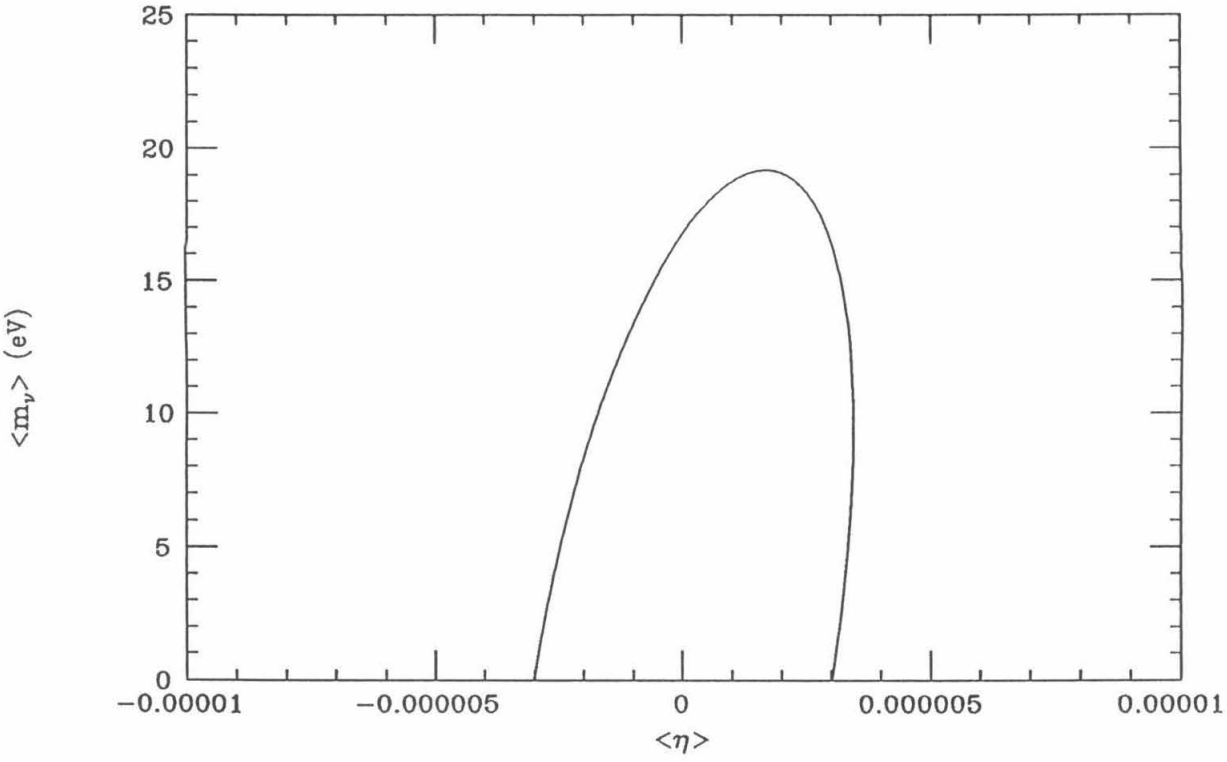

Figure 5.3 90 % confidence level excluded region along $< \eta > - < m_\nu >$ plane for $T^{0\nu}_{1/2} > 1 \times 10^{23}$ y. The values for C_i are calculated by Haxton & Stephenson and are compiled by Doi et. al.

5.1.2 $0^+ \rightarrow 2^+$ Transition

The rate of the $0^+ \rightarrow 2^+$ transition does not depend explicitly on the Majorana mass of the neutrino (although some Majorana mass is necessary), and the decay rate depends only on the values of λ and η :

$$(T^{0\nu}_{1/2}(0^+ \rightarrow 2^+))^{-1} = D_1\lambda^2 + D_2\lambda\eta + D_3\eta^2,$$

where the values for D_i are given in Chapter 2. Since the $0^+ \rightarrow 2^+$ transition energy of 1480.5 keV lies at a lower energy than the $0^+ \rightarrow 0^+$ transition energy, the half-life limit is poorer since the backgrounds tend to decrease with increasing energy. Thus, the limits on the right-handed mixing parameters are much worse than those derived from the $0^+ \rightarrow 0^+$ transition. Like the $0^+ \rightarrow 0^+$ case, a limit on the $0^+ \rightarrow 2^+$ transition defines an ellipse in $< \eta > - < \lambda >$ space that encloses the allowed values of the right handed coupling parameters. The exclusion plot for our limit is shown in Figure 4 and gives the limits

$$|< \eta >| < 0.0025$$

$$|< \lambda >| < 0.004$$

both at 90 % confidence level.

5.2 Neutrinoless Double Beta Decay with Majoron Emission

The measurement of the decay rate into two electrons and a Majoron χ^0 provides a measurement of the $\nu - \chi^0$ coupling constant g_{ee} as described in Chapter 2. Since the $\chi^0\beta\beta$ decay rate depends on the 0ν nuclear matrix element, the limit on g_{ee} is uncertain by the same factor of 30 as the neutrino's Majorana mass, Table 2. The dependence of the $\chi^0\beta\beta$ decay rate is hidden in the relation

$$g_{ee}v = m_{\nu,Majorana},$$

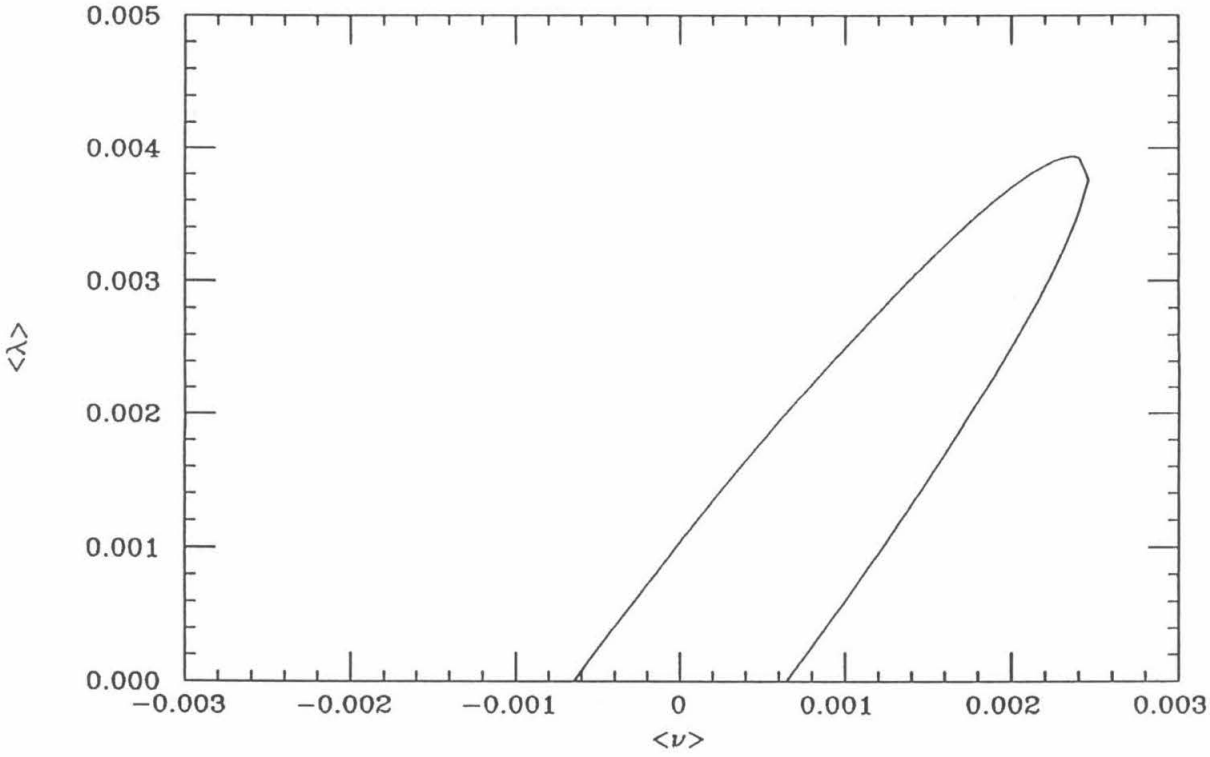

Figure 5.4 Exclusion plot for $T^{0\nu}_{1/2} > 2 \times 10^{22}$ y (90 % c.l.) The matrix elements are from Haxton & Stephenson and are compiled in Doi et. al. [13]

Calculation	g_{ee}
Vogel et. al. [22]	8×10^{-3}
Klapdor & Grotz [23]	8×10^{-4}
Haxton & Stephenson [12]	3×10^{-4}

Table 5.2 Majoron coupling constant and Majorna neutrino mass limits from different calculations of the nuclear matrix element for ^{76}Ge and for the half-life limit of $T^{\chi^0}_{1/2} > 1.2 \times 10^{21}$y, 90 % c.l.

where v is the vacuum expectation value of the Majoron. Astrophysical arguments give $v < 10^5$ eV, so a measurement (or limit) of g_{ee} in the range of 10^{-5} could be used to determine the Majorana mass (or mass limit) of the neutrino.

As discussed in Chapter 4, our limit of $T^{\chi^0}_{1/2} > 1 \times 10^{21}$ y (90 % c.l.) is in sharp contradiction with the reported PNL/USC measurement of $T^{\chi^0}_{1/2} = (6 \pm 1) \times 10^{20}$ y. Other measurements of the limit of $\chi^0\beta\beta$ decay in ^{82}Se and ^{136}Xe [39] also exclude the PNL/USC result for all calculations of the 0ν nuclear matrix elements. However, all of these results depend on rather complex background calculations and more work needs to be done in this area.

5.3 Two Neutrino Double Beta Decay

Our limit of $T^{2\nu}_{1/2} > 3.0 \times 10^{20}$ y lies just above the fastest calculated rate of $T^{2\nu}_{1/2} = 1.5 \times 10^{20}$ of Klapdor et. al. [23]. This calculation does not include the particle - particle interaction which tends to suppress $2\nu\beta\beta$ decay. Although $2\nu\beta\beta$ decay is allowed by the Standard Model, its observation is of crucial importance for solving the nuclear matrix element problem and work is continuing to further understand, calculate and subtract the background from gamma ray sources.

Recently, $2\nu\beta\beta$ decay has been observed in the decay of ^{82}Se with the U.C. Irvine Time Projection Chamber (TPC) [40] with a half-life of $1 \pm 0.5 \times 10^{20}$ y. This half-life agrees very roughly with half-life calculation of 1×10^{20} y from Vogel et al.

[22]. All the other calculations predict faster rates, indicating the suppression from the particle-particle interaction may be present. Additional measurements of the $2\nu\beta\beta$ decay half-life are still needed, and the hope is the new generation of xenon experiments (see Chapter 6) will provide more positive measurements.

Chapter 6

Outlook for $\beta\beta$ Decay Counting Experiments

Laboratory searches for $\beta\beta$ decay continue to expand by being sensitive to longer half-lives and using a wider range of candidate isotopes. The fundamental importance of neutrino mass and lepton number conservation means that these experiments will continue long into the future.

Currently, the longest half-lives and lowest mass limits come from ^{76}Ge experiments such as the one described in this thesis. It seems clear, however, that this position will be relinquished before long; the size of the current systems is at technological and, more importantly, financial limits. Several groups, the ITEP/Erevan group [41] in particular, are working with germanium detector crystals grown from enriched ^{76}Ge. The ITEP/Erevan currently has one such 90 cm^3 89% enriched crystal with a second planned. Such a system will have roughly 12 moles of ^{76}Ge nuclei, about twice the present experiment with much lower background per mole of ^{76}Ge nuclei. The resolution of such detectors is quite poor (6 - 20 keV at 2 MeV), giving roughly the same sensitivity as present germanium experiments.

From the point of view of the present (poorly understood) nuclear structure of $\beta\beta$ decay, a large nuclear matrix element makes ^{136}Xe an attractive candidate. Its high Q value of 2.480 MeV provides some phase space enhancement over ^{76}Ge

and lies above the Compton edge of the ^{208}Tl 2.614 MeV line. Several groups are currently beginning experiments in which ^{136}Xe is used as a fill gas in various types of detectors. Two of the most promising of these experiments are the Caltech-SIN-Neuchatel Time Projection Chamber (TPC) [42]and the Milano proportional counter experiment [43].

The TPC has the distinct advantage that the trajectory of each electron is recorded. When a ^{136}Xe nucleus $\beta\beta$ decays, the two emitted electrons pass through the xenon gas filling the chamber, losing energy as they ionize atoms along the way. An electric field drifts the electrons liberated in the ionization down to an x-y pad on the bottom of the chamber where the z position of the ionization event is recovered by recording the arrival time of the ionization electrons, allowing full reconstruction of the electron track. As they lose energy, the $\beta\beta$ decay electrons will become more strongly ionizing, resulting in characteristic "blobs" at the end of each electron track where the electron finally stops. Thus, a $\beta\beta$ decay event will have a very distinct signature; a contained track with a blob on each end. The Caltech-SIN-Neuchatel TPC will contain 40 moles of ^{136}Xe (when filled with enriched xenon) and will have a 20 % efficiency for containing a $\beta\beta$ decay event and so will be sensitive to half-lives of the order of 10^{24}y or masses in the range of 2.0 -0.2 eV, depending on the nuclear matrix element. For the $2\nu\beta\beta$ decay mode, the TPC's ability to fully reconstruct tracks should make it sensitive to half-lives on the order of 10^{22} y. The TPC is currently operating at Caltech and will be installed in the St. Gotthard tunnel in Spring 1988.

The Milano group took a different approach to the same problem by constructing a large segmented proportional counter using ^{136}Xe as a fill gas. In this case, the inner volume is segmented into 61 cells, each cell consisting of a wire held at high voltage surrounded by guard wires. Electrons emitted in a $\beta\beta$ decay will ionize atomic electrons, which will be drifted toward the high voltage sense wire and

detected. By requiring that all firing cells be connected and restricting the number of firing cells to between 3 and 8, large background reduction is possible. The Milano system contains about 40 moles of ^{136}Xe (when filled with enriched xenon) and so will be sensitive to roughly the half-life and mass range as the TPC. The Milano experiment has been operating in the Gran Sasso underground laboratory since Spring 1987 with natural xenon and has already reported a half-life limit of $T^{0\nu}_{1/2} > 4 \times 10^{21}$ y, (68 %c.l.).

Several other groups [44] are also experimenting with low resolution high pressure (30 - 100 atm) xenon ionization chambers. The projected chambers will contain fewer ^{136}Xe atoms, but will have nearly 100 % efficiency and, with 1 - 2 % resolution, will have roughly the same sensitivity as the larger xenon experiments. Several problems relating to gas purity need to be solved and so far no group has achieved better than 2.7 % at 30 atm.

In the spirit of the early geochemical experiments, several groups [45] are attempting to count the daughter products of $\beta\beta$ decay. In the case of ^{136}Xe, the daughter product, ^{136}Ba, is drifted onto some substrate, which is then sputtered off and run through a high precision mass spectrometer which will, it is hoped be sensitive to tens of atoms. Several problems concerning the ion drifting and sputtering process remain to be solved.

Finally, one very intriguing prospect is the use of cadmium-telleride (CdTe) detectors. CdTe is a room-temperature semiconductor that has been used for charged particle and gamma ray spectroscopy in recent years. Small (< 1 cm ^{3}) CdTe detectors may have resolutions as low as 1 %. CdTe contains no less than five double beta decay candidates (^{106}Cd, ^{114}Cd, ^{116}Cd, ^{128}Te and ^{130}Te). In particular, ^{116}Cd and ^{130}Te have endpoints above 2.5 MeV (2.580 and 2.840 MeV respectively) making them excellent candidates for $\beta\beta$ decay search. A 0.3 cm^3 system has been constructed and operated for 450 h [46], giving limits of $T^{0\nu}_{1/2} > 3 \times 10^{18}$y for ^{130}Te

and $T^{0\nu}_{1/2} > 3 \times 10^{18}$y for ^{116}Cd, both at 90 % c.l. A much larger system (100 cm^3) is required to be sensitive to neutrino masses below 10 eV. Large CdTe crystals have problems with charge build-up and, to address this problem, an intermediate system of 3 cm^3 is planned.

Appendix A

A Monte Carlo for Background Calculation

The subtraction of gamma ray background described in Chapter 4 requires that the Compton continuum from a known gamma ray source be calculated based on the source position, the geometry of the detector and the geometry and materials surrounding the detector. To this end, a Monte Carlo program, Geant v3.10 was used. This appendix describes the theory and operation of the Monte Carlo used.

Suppose a gamma ray source may be characterised by a function $S(\vec{x}, \vec{p}, E)$ which gives the source intensity for each momentum interval and point in space, then the detector's response as a function of energy (or pulseheight) will be given by

$$I(E') = \int d\vec{x} d\vec{p} D(\vec{x}, \vec{p}, E; E') S(\vec{x}, \vec{p}, \vec{E}).$$

The function $D(\vec{x}, \vec{p}E; E')$ simulates the detector's response; for a monoenergetic, well collimated, point source of unit intensity , $S(\vec{x}, \vec{p}, E) = \delta(\vec{x} - \vec{x_0})\ \delta(\mid \vec{p} \mid - \mid \vec{p_0} \mid)$, $D(\vec{x_0}, \vec{p_0}, E_0; E')$ will give the detector's response as a function of E'. In practice, it is nearly impossible to compute D analytically; the physical processes which take place in the detector are manifold and strongly energy dependent. The Monte Carlo method provides a straight forward way of computing D for a given S.

The Monte Carlo method acts like a polling agency before an election. Since all the voters cannot (economically) be questioned, a representative subset is questioned

to give some indication of the opinion of the population at large. In the same way, the Monte Carlo method samples a number of different possible tracks the gamma ray may take through the detector and obtains a sample response function $I(E')$ for a given source S. If the number of sampled pathes is large enough, the sample response function should be a close approximation to the actual response function.

This calculation is best carried out on a computer which allows the number of sampled paths to be very large. The details of the Monte Carlo program used need some explanation. Geant is a detector simulation package (written at CERN) which provides the user with a set of routines which handles the bookkeeping of the simulation. The user provides the program with a description of the geometry and material of the detector and surrounding materials and a routine describing the source distribution function. The program samples the source distribution to obtain a starting position and momentum and computes the probability per unit path length for all the relevant physics processes (Compton scattering, photo absorption, pair production). The gamma ray is "moved" in unit steps along its momentum vector and, at each step, the probability for each process is sampled. If one of the above processes takes place, the appropriate distributes are sampled and the energy, position, momentum and type of each secondary particle is stored. This is continued until the primary photon leaves the apparatus or is absorbed. Next, all the secondary particles are tracked in the same way and *their* secondaries are tracked and so on until there are no particles left to be tracked. This constitutes an event.

For each of the photon related processes, an energetic electron is produced. The tracking of the electrons is handled in a somewhat different way than the photons since the electrons lose energy in small steps as they ionize bound atomic electrons close to their trajectories. To save computer time, the ionization electrons are not tracked if they are below some energy threshold, typically 100 keV. Ionization

electrons which are created inside the active region of the germanium detector are assumed to contribute to the pulseheight; their kinetic energy is added to the total pulseheight of the event. Electrons may also bremsstrahlung, emitting a photon, which is also tracked.

The Geant package has been extensively tested at CERN to insure the tracking and physics routines are corrected. Geant was also tested by setting up a germanium detector in a known geometry with a known source. and comparing the measured spectrum with a simulation for an identical detector and source using Geant. The results of one such test is shown in Figure 1. In this test, a ^{60}Co source was placed on axis 20 cm in front of an 80 cm^3 germanium detector. The Monte Carlo was then set up to simulate this geometry. In general, the agreement between the measurement and calculation is good above 200 keV, with the Monte Carlo calculation tending to underestimate the number of counts slightly. Below 250 keV, the Monte Carlo underestimates the number of counts by roughly 10 %. The reasons for this is clear: to make the calculation run in a reasonable amount of time, the Monte Carlo only generates primary gamma rays in a limited solid angle directed at the detector face. In reality, gamma rays generated outside of this solid angle may scatter off the table on which the source is placed, the source holder or other materials close to the setup and then enter the detector. Since most such events would involve one or more large angle scatterings, the gamma rays which make it into to detector will be generally low energy, below 250 keV. Additionally, the exact construction of the detector and source is not known and this may lead to an underestimation of the number of low energy counts. This is especially clear in Figure 1; the backscatter peak around 230 keV does not appear beacuse the exact composition of the detector holder behind the crystal is not known. A second test was carried out with the same apparatus with a 2.5 cm copper plate inserted between the source and detector (Figure 2). The spectrum softens because gamma ray may now Compton scatter in the copper before

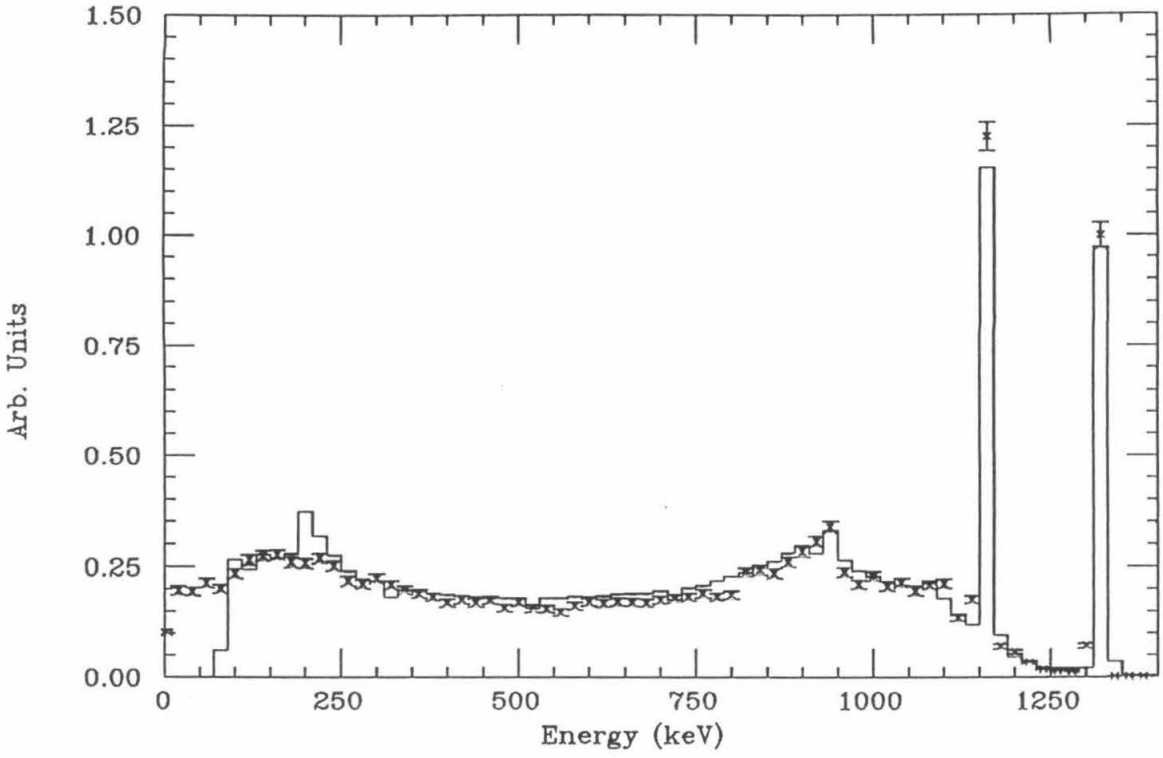

Figure A.1 A comparison of measured (histogram) and calculated (points) pulseheight spectrum for an 80 cm^3 detector of known geometry with a ^{60}Co source. The errors for the measured points are about 10 %.

entering the detector crystal. Here again, the agreement between calculation and measurement is good down to about 250 keV, where the calculation underestimates the number of counts. Tests have been carried out with other sources (^{137}Cs and ^{128}Na) which emit two gamma rays in cascade and here too, agreement between calculation and experiment is quite good above about 300 keV.

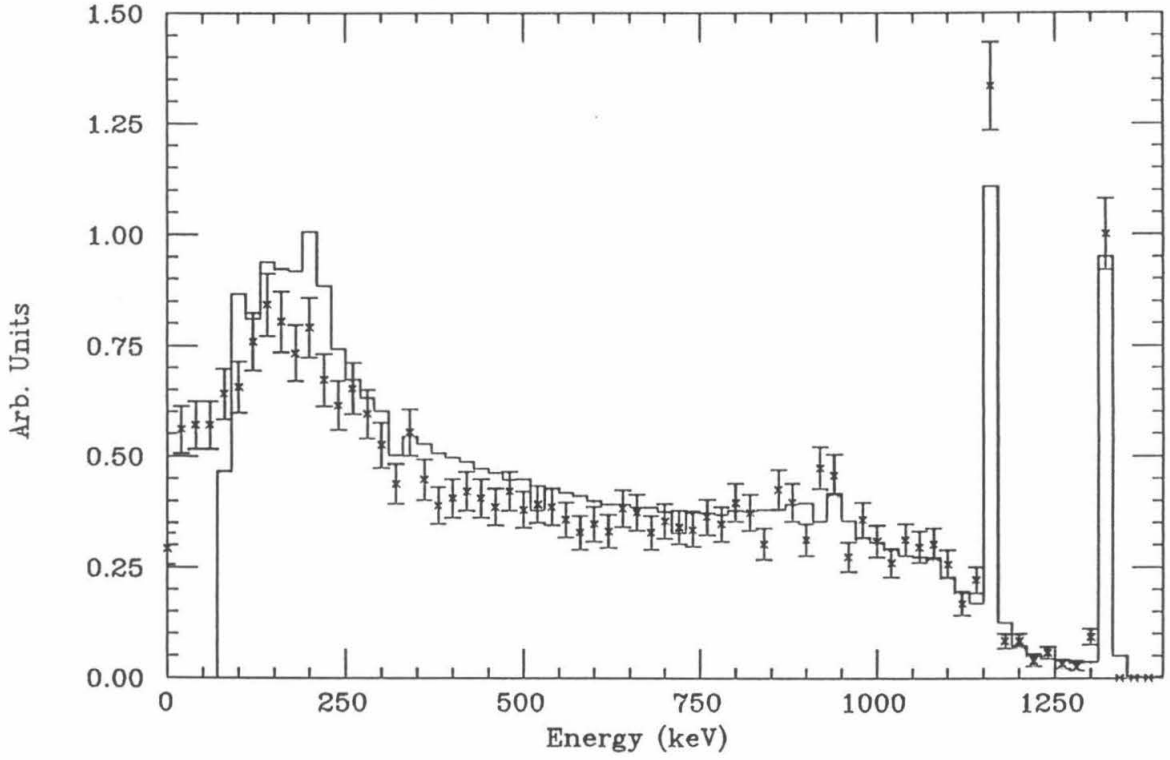

Figure A.2 A comparison of measured (histogram) and calculated (points) pulseheight spectrum for an 80 cm^3 detector of known geometry with a ^{60}Cs source. A 2.5 cm thick copper plate was placed between the source and the detector causing the spectrum to soften.

References

[1] W. Pauli *Letter to the Physical Society of Tubingen, unpublished; reproduced in* L.M.Brown, *Physics Today*, **31**, No. 9, 23, (1978).

[2] F. Reines and C. Cowan, *Phys. Rev.*, **90**, 492 (1953).

[3] T.D.Lee and C.N. Yang, *Phys. Rev.*, **104**, 254 (1956).

[4] S.L.Glashow, *Nucl. Phys.*, **22**, 579 (1961).
A.Salam and J.C.Ward,*Phys. Rev. Lett.*, **13**, 168 (1964).
S.Weinberg, *Phys. Rev. Lett.*, **19**, 1264 (1967).

[5] G.Barbiellini and C.Santoni, CERN-EP/85-117 (1985).

[6] J.Bernstein, CERN 84-06 (1984). Ya.Zeldovich, *Rev. Mod. Phys.*, **53**, 1 (1981).

[7] J.Primack, SLAC-PUB-3387, (1984).

[8] B.Kayser, *Comments on Nuclear and Particle Physics*, **14**, 69 (1985).

[9] E.Commins amd P.H.Bucksbaum, Weak Interactions of Leptons and Quarks, Cambridge University Press/London (1983).

[10] F.H.Boehm and P.Vogel, Physics of Massive Neutrinos, Cambridge University Press/London (1987).

[11] J.-L. Vuilleumier, *Rpe. Prog. Phys.*,**49**, 1293 (1986).

[12] W.C.Haxton and G.J.Stephenson, *Prog. Part. Nucl. Phys.*, **12**, 409 (1984).

[13] M.Doi et al., *Prog. Theo. Phys. Supp.*, **83**, 1, (1985).

[14] H.M.Georgi,etal. *Nucl. Phys.*, **B193**,297 (1981).

[15] P.Vogel and P.Fisher, *Phys. Rev.*, **C32**, 1362 (1985).

[16] T.Kirsten et al., *Phys. Rev. Lett.*, **50**, 474 (1983).

[17] H.V. Klapdor and K. Grotz, *Nucl. Phys.*, **A460**, 395 (1986).

[18] T.Tomoda et al. *Nucl. Phys.*, **A452**, 591 (1986).

[19] A.J. Rassey *Phys. Rev.*, **109**, 949 (1958).

[20] G.E. Brown Many Body Problems, North-Holland/Elsevier (1972).

[21] C.Gaarde, *Nucl. Phys.* **A396**, 127 (1983).

[22] P.Vogel et al., MAP-95, *Submitted to Phys. Rev. C* (1987).

[23] H.V.Klapdor and K.Grotz, *Phys. Lett.*, **142B**, 323 (1984).
K.Grotz and H.V.Klapdor, *Nucl. Phys.*, **A460**, 395 (1986).

[24] T.Tomoda and A. Faessler, *Preprint, University of Tubingen*, (1987).

[25] V.Lubimov, *Massive Neutrinos in Astrophysics and Particle Physics, Proceedings of the 7th Moriond Workshop*, eds. O. Fackler and J.Tran Thanh Van, Editions Frontieres, Paris (1987).

[26] W.Kundig et al., *Proc. Harrogate Conference*, in press.

[27] B. Jeckelmann et al., *Phys. Rev. Lett.*, 56, 1444, (1986).

[28] Kolanski et al., *Proceedings of the EPS High Energy Physics Conference, Uppsala, Sweden, 24 June - 1 July 1987*, in press.

[29] D.O.Caldwell et al., UCSB Preprint, January 1987.

[30] G.F.Knoll,Radiation Detection and Measurement, John Wiley and Sons/New York (1979).

[31] P.Fisher et al.,*Phys. Lett.***B192**, 12 (1987).

[32] L.L.Carter & E.D.Cashwell, Particle-Transport Simulation with the Monte Carlo Method, ERDA Critical Review Series (1975).

[33] M.Aguilar-Bemitz et al.,*Particle Propeties Data Booklet*, Particle Data Group, North Holland (1986).

[34] A.Forster, et al., *Phys. Lett.* **138B**, 301 (1984).

[35] P.Fisher, *Massive Neutrinos in Astrophysics and Particle Physics, Proceedings of the 7th Moriond Workshop*, eds. O. Fackler and J.Tran Thanh Van, Editions Frontieres, Paris (1986).

[36] *Proposal for the Sudbury Heavy Water Neutrino Observatory*, 1985.

[37] A.Baker & B.Couzens, *NIM*,**221**, 442 (1984).

[38] F.T.Avignone et al., Talk presented to the American Physical Society, Salt Lake City, Jan. 14-17, 1987; Univ. of South Carolina preprint, Jan. 1987.

[39] P. Fisher et al., *Proceedings of the EPS High Energy Physics Conference, Uppsala, Sweden, 24 June - 1 July 1987*, in press.

[40] S.R. Elliot, et al., *Phys. Rev. Lett.*, **59**, 2020 (1987).

[41] Hamburg Conference, June 1987.

[42] J. Thomas, *New and Exotic Phenomena in Physics and Astrophysics, Proceedings of the 8th Moriond Workshop*, eds. O. Fackler and J. Tran Thanh Van, Editions Frontieres (1987).œ[B

[43] O. Cremonesi, *Proceedings of the EPS High Energy Physics Conference, Uppsala, Sweden, 24 June - 1 July 1987*, in press.

[44] J. Thomas, *Private Communication*, 1987.
A.S. Barabash, *NIM*, **B17**, 450 (1986).
Apirle, 1987.

[45] L. Mitchell, *Private Communication*, 1987.

[46] L. Mitchell & P. Fisher, Caltech Preprint, *Submitted to Phys. Rev. C*, 1987.

[47] T.F.Cavaignac et al., *Phys. Lett.*, **B148**, 387 (1984).

[48] G.Zacek et al., *Phys. Rev.*, **D34**, 2621 (1986).

[49] D.Kocher, *Radioactive Decay Tables*, Washington (1979).

[50] U.Reus et al., *Gamma Ray Catalog*, G.S.I. Report 79-2, Darmstadt, West Germany (1979).

[51] J.P.Egger, *Private communication.*